

1-1-1983

MM-wavelength measurements of CO in the atmosphere of Mars and SO₂ in the atmosphere of Venus.

John Conrad Good

University of Massachusetts Amherst

Follow this and additional works at: https://scholarworks.umass.edu/dissertations_1

Recommended Citation

Good, John Conrad, "MM-wavelength measurements of CO in the atmosphere of Mars and SO₂ in the atmosphere of Venus." (1983).
Doctoral Dissertations 1896 - February 2014. 1750.
https://scholarworks.umass.edu/dissertations_1/1750

This Open Access Dissertation is brought to you for free and open access by ScholarWorks@UMass Amherst. It has been accepted for inclusion in Doctoral Dissertations 1896 - February 2014 by an authorized administrator of ScholarWorks@UMass Amherst. For more information, please contact scholarworks@library.umass.edu.

**FIVE COLLEGE
DEPOSITORY**

MM-WAVELENGTH MEASUREMENTS
OF CO IN THE ATMOSPHERE OF MARS
AND SO₂ IN THE ATMOSPHERE OF VENUS

A Dissertation Presented

By

John Conrad Good

Submitted to the Graduate School of the
University of Massachusetts in partial fulfillment
of the requirements for the degree of

DOCTOR OF PHILOSOPHY

September 1983

Physics and Astronomy

MM-WAVELENGTH MEASUREMENTS
OF CO IN THE ATMOSPHERE OF MARS
AND SO₂ IN THE ATMOSPHERE OF VENUS

A Dissertation Presented

By

John Conrad Good

Approved as to style and content by:



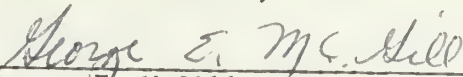
F. Peter Schloerb, Chairman of Committee



William M. Irvine, Member



David Van Blerkom, Member



George E. McGill, Member



LeRoy F. Cook, Department Head
Physics and Astronomy

ACKNOWLEDGEMENTS

It is a pleasure to have this opportunity to acknowledge the efforts of all those without whose help this thesis would have been impossible. Certainly first on the list is my advisor Peter Schloerb, who had most of the ideas and who edited some portions of the thesis so thoroughly that I sometimes wondered whether I could legitimately claim to have written it at all. Also high on the list is William Irvine who, besides supporting the work, was always ready with useful comments and questions. I would also like to thank the other members of my committee, David Van Blerkom and George McGill, for sifting through the document and for their many helpful comments. Thanks also to Donald Hunten for providing insight during the early Mars CO work.

I am grateful to the staff of the Five College Radio Astronomy Observatory for making it such a great place to work. My thanks also goes to the staff of the Hat Creek Radio Astronomy Observatory and especially to Jack Welch for his assistance and encouragement. This research was supported by NASA Grant NGL 22-010-023. The FCRAO is operated under NSF Grant AST 80-26702 and the HCRAO under NSF Grant AST 78-21307.

My special thanks goes to my wife, Mih-seh, whose support through all my graduate studies has, more than anything else, kept me going.

ABSTRACT

MM-Wavelength Measurements
of CO in the Atmosphere of Mars
and SO₂ in the Atmosphere of Venus

(September 1983)

John C. Good, B.A., Western Michigan University

M.A., University of Hawaii

Ph.D., University of Massachusetts

Directed by: Professor F. Peter Schloerb

Chemical modeling of the atmospheres of Mars and Venus has long suffered from poor knowledge of the abundances of some of the more important chemical species. On Mars, questions concerning the stability of the CO₂ atmosphere to photodissociation rely on uncertain abundance measurements of CO and O₂, its daughter products. In this work, millimeter-wavelength spectra of CO on Mars are used to determine both its abundance and the temperature profile in the atmosphere. Two different lines (CO(J=1-0) and CO(J=2-1)) are required to do this unambiguously since it is found that the abundance derived is extremely dependent on the form of the atmospheric temperature profile chosen. The CO mixing ratio determined, $(8 \pm 3) \times 10^{-4}$, is very close to that measured from infrared lines (Kaplan et al., 1969, Young, 1971) and is therefore consistent with models in which this abundance does not vary with time. On Venus, the study of the chemistry of the omnipresent sulfuric acid clouds would likewise benefit from an accurate measure-

ment of the abundances of sulfur compounds and particularly of SO_2 , the major sulfur bearing compound in the region below the clouds. Constraints on the abundance profile of SO_2 on Venus are made via an interferometric measurement of the amount of limb darkening at 3.4 μm . The limb darkening indicates that the absorption coefficient profile in the atmosphere is essentially consistent with a pure CO_2 atmosphere with no additional absorbers. Hypothetical SO_2 profiles were modeled and it was found that the large SO_2 abundance measured by the Pioneer Venus entry probes in the lower atmosphere must begin to decrease well below the bottom of the lower cloud, indicating that a destruction mechanism for SO_2 exists in this region.

TABLE OF CONTENTS

INTRODUCTION 1

PART I. MARS CO ABUNDANCE

Chapter

I. INTRODUCTION 4

II. OBSERVATIONS 9

 1980 CO(J=1-0) Measurements

 1982 CO(J=1-0) and CO(J=2-1) Measurements

III. ATMOSPHERIC MODEL 16

 Radiative Transfer

 Absorption Coefficient of CO

 Viking Measurements - Constraints on the Model

IV. MODEL FITTING TO THE CO(J=1-0) LINE 25

V. SIMULTANEOUS FITTING OF TWO CO LINES 36

VI. SUMMARY AND CONCLUSIONS 61

.

BIBLIOGRAPHY 64

PART II. VENUS SO₂ ABUNDANCE

Chapter

I. INTRODUCTION 68

II. MEASUREMENT OF THE ZERO CROSSING 74

Observations	
Baseline Determination	
Phase Calibration	
Amplitude Calibration	
Fit to Zero Crossing	
III. INTERPRETATION OF THE ZERO CROSSING	88
Introduction	
Model Limb Darkening Curves	
Calculation of the Visibility Function	
Model Fitting to Zero Crossing Measurement	
Conclusions on SO ₂ Abundance Profile	
IV. DISCUSSION	112
Sulfur Chemistry in the Clouds of Venus	
Other Possible Sources of Opacity	
Brightness Temperature of Venus at Millimeter Wavelengths	
Use of Venus as an Absolute Calibration Source	
.	
BIBLIOGRAPHY	119
APPENDIX A - Visibility Function from Brightness Temperatures . .	123
APPENDIX B - Error Analysis	129
APPENDIX C - Theoretical Limb Darkening Curve	141

LIST OF TABLES

PART I. MARS CO ABUNDANCE

1. Results of Fitting Model to 1982 Mars CO(J=1-0) Line.	32
2. Results of Simultaneously Fitting Model to 1982 Mars CO(J=1-0) and CO(J=2-1) Lines	37
3. Results of Simultaneously Fitting Model to Simulated Mars CO(J=1-0) and CO(J=2-1) Lines.	55

PART II. VENUS SO₂ ABUNDANCE

1. Baseline Sources	76
-------------------------------	----

LIST OF ILLUSTRATIONS

PART I. MARS CO ABUNDANCE

1.	1980 CO(J=1-0) Data and Fit Jupiter Spectrum as a Baseline Check	11
2.	a) 1982 CO(J=1-0) Line b) 1982 CO(J=2-1) Line.	14
3.	Constant Lapse Rate Model Fit to 1982 CO(J=1-0) Line	27
4.	a) Best Fit CO Mixing Ratio <u>vs</u> Assumed Surface Pressure for the 1982 CO(J=1-0) Line b) Best Fit CO Mixing Ratio <u>vs</u> Assumed Lapse Rate for the 1982 CO(J=1-0) Line	29
5.	Two Lapse Rate Temperature Profiles from Fits to the 1982 CO(J=1-0) Line with the CO Mixing Ratio Fixed	34
6.	a) Constant Lapse Rate Model Fits to the 1982 Data b) Corresponding Temperature Profiles.	38
7.	a) Double Lapse Rate Model Fits to the 1982 Data b) Corresponding Temperature Profiles.	42
8.	a) Multiple Lapse Rate Model Fits to the 1982 Data b) Corresponding Temperature Profiles.	46
9.	a) Surface Temperature Offset Model Fit to the 1982 Data b) Corresponding Temperature Profiles.	51
10.	a) Fits to the Simulated Data b) Corresponding Temperature Profile and True Structure.	56

PART II. VENUS SO₂ ABUNDANCE

1.	Phase Variations of Reference Calibrators.	77
2.	Sample Venus Phase Data with Fitted Polynomial	81
3.	Venus Amplitude Data with Polynomial Fit to Zero Crossing.	85
4.	Absorption Coefficients for CO ₂ and SO ₂	97
5.	Zero Crossings and Brightness Temperatures for Cutoff Model.	105
6.	Upper Limits to the SO ₂ Abundance Profile.	109

I N T R O D U C T I O N

Chemical processes in the atmospheres of Mars and Venus are similar enough to those on the Earth to make their study valuable for the insight it gives into the problems of our own atmosphere. Indeed, work on the effects of trace constituents in the atmosphere of Venus has already sensitized us to the problem of ozone depletion in our own stratosphere.

Unfortunately, this research is severely limited by the quality and quantity of abundance measurements for some of the more chemically important species. On Mars, the photodissociation of CO_2 , by far the main constituent of the atmosphere, is extremely efficient and if the recombination of its daughter products, CO and O_2 , were not catalytically aided, this process would essentially go to completion. While measurement of those species (OH , HO_2 , H_2O_2) which supposedly act as intermediaries in this process can help us predict how far and how fast this recombination should proceed, direct determinations of the CO and O_2 abundances specify exactly how efficient that process is.

The most obvious and important factor in the atmosphere of Venus is the perpetual presence of thick sulfuric-acid cloud banks. The main sulfur-bearing compound in the lower atmosphere is SO_2 . The process through which this species is brought up through the cloud layers, converted to sulfuric acid, and returned to the lower atmosphere in this form is almost completely unknown. Sulfur compounds are relatively

minor constituents in the atmosphere and can react with a host of other chemical species. Thus, determination of the SO_2 abundance profile in and just below the cloud layers should help to elucidate the details of the cloud sulfur chemistry.

Planetary research using mm-wavelength lines holds the promise of solving these and other problems related to the chemistry of planetary atmospheres. Spectral measurements at these wavelengths can be made at resolutions impossible in the visible and infrared, thereby allowing a fit to the lineshape itself, essentially uncomplicated by the instrumental profile. In many cases, this wavelength region probes a part of the atmosphere unreachable by any other means. For Mars, measurement of the $\text{CO}(J=1-0)$ and $\text{CO}(J=2-1)$ lines shows enough structure in their shape to allow a fit to several atmospheric parameters simultaneously and with strong constraints. In the case of Venus, interferometric measurements of the SO_2 abundance profile via the limb darkening curve at 3.4 mm probe the region of the cloud base, far below the cloud-top measurements made in the visible and infrared.

In this thesis, we will attempt to use these techniques to constrain the CO on Mars and SO_2 on Venus. In each case, we are looking not at a catalyst or by-product of the interesting chemical cycle but at one the main participants. Thus the results, whatever they may be, place direct constraints on that cycle.

P A R T I

MARS CO ABUNDANCE

C H A P T E R I

INTRODUCTION

The abundance of CO in the atmosphere of Mars has long been used as an indicator of the aeronomical processes that are occurring there. The original determinations of a very low CO abundance (Kaplan et al., 1969) triggered much work to explain the stability of the CO₂ atmosphere to photodissociation into CO and O₂. The main explanation of this stability (McElroy and Donahue, 1972, Parkinson and Huntten, 1972), that small amounts of odd H (H, OH, HO₂ etc.) species catalyze the recombination of CO and O₂ into CO₂, has had an impact on studies of the photochemistry of all planets and made us much more conscious of the effect of trace amounts of pollutants on the photochemistry in our own stratosphere.

The CO millimeter-wavelength lines (primarily CO(J=1-0) and CO(J=2-1) at 115.271 and 230.538 GHz, respectively) are potentially excellent tracers of the atmospheric temperature and CO abundance structure since millimeter technology is capable of resolving them (Schloerb et al., 1980). This allows fitting to the pressure broadened line structure itself, each frequency measured supplying additional information. Therefore, depending on the signal-to-noise ratio, there

can be enough information in a single line to constrain a very complex atmospheric model.

The first detection of the CO(J=1-0) line by Kakar et al.(1977) showed a strong absorption, though unfortunately their spectrum did not extend far enough out into the wings of the line to allow accurate modeling. Therefore, their observations provided a poor constraint on the CO abundance. Encouraged by the strength of the line, Good and Schloerb (1981) measured it with a bandpass wide enough to reach the continuum level. Their analysis found that this line could be fit with an extremely simple atmospheric temperature structure model (a single constant lapse rate) and that within the context of this model the CO abundance was well constrained. The uncertainty in this abundance was estimated from the range of values that resulted from fits to hypothetical extreme temperature profiles. All of these results were internally consistent and seemed to indicate a CO abundance of $(3.2 \pm 1.1) \times 10^{-3}$, which was about three times greater than had been previously measured from infrared lines (Kaplan et al., 1969, Young, 1971). Thus, comparison of millimeter and infrared observations suggested that the Mars CO abundance had varied over the ten years between the observations.

Interestingly enough, such a variation had been anticipated theoretically by Hunten (1974) who discussed the stability of odd H species in the atmosphere of Mars. These are all derived principally

from H_2O , a condensible species, and are, in some cases, themselves condensible (H_2O_2 and HO_2). For this reason, Hunten argued that the process of CO and O_2 recombination might itself be unstable in time and that variations in the abundances of CO and O_2 might exist. Because the doubling time for the CO concentration in the Mars atmosphere is only about two years (Hunten, 1974), detectable changes in the CO abundance might be expected on this scale. Thus, the abundance variation found by Good and Schloerb (1981) appeared to be quite plausible in view of the current understanding of the atmosphere of Mars.

A reassessment of the data of Good and Schloerb (1981), along with an analysis of a new CO(J=2-1) spectrum, by Clancy et al. (1983) found a quite different result. To better perform the disk averaging, they created a grid of locations across the face of the planet, modeled the surface temperature and the emission properties at each point, postulated a latitude- and time-of-day-dependant atmospheric temperature structure (as offsets from a nominal model based on Viking data) at each location, and integrated the radiative transfer equation to give the intensities on their grid. While this very detailed approach is more accurate, one interesting result of this model was that treating the properties of Mars as uniform across the disk yields surprisingly good results, a factor utilized in the current analysis. A second surprising result was that with this model, Clancy et al. found that their fit to the CO(J=1-0) spectrum of Good and Schloerb gave a mixing ratio much closer to that found from the infrared lines in the Connes

spectral atlas (Kaplan et al., 1969, Young, 1971), suggesting that CO may not in fact be variable after all. Their CO(J=2-1) data, on the other hand, gave evidence for a high CO abundance, like that found by Good and Schloerb. Thus, there remained a discrepancy both between the mixing ratios from the two fits to the CO(J=1-0) data of Good and Schloerb and between the values found for that line and the CO(J=2-1) line, and the interesting question of CO variability on Mars remained open.

In view of the contradictory evidence and conflicting results obtained by previous workers, this work will attempt to study the use of millimeter lines in the determination of the CO abundance. In the previous work, the researchers have made seemingly valid assumptions regarding the independent model parameters (defined to be everything but the CO abundance) and have been able to fit the CO(J=1-0) line or, alternatively, the CO(J=2-1) line. However, since none of the abundances derived agree, it is apparent that these assumptions must be reexamined.

The main difficulty with all previous work is that although there is potentially enough information in a single line to constrain a complex model, this potential is difficult to realize due to the possible complexity in the details of the atmospheric structure. Not only must the atmospheric temperature profile be accurately defined to calculate a model line profile, but an accurate surface temperature and

CO mixing ratio structure are also needed. Obviously, even with such simplifying assumptions as a constant CO mixing ratio and disk averaged quantities, the accuracy of a deduced CO abundance is only as good as the temperature structure assumed. What is more unclear is the degree to which this relationship affects the CO abundance derived. In this section, it will be shown that the CO abundance derived is, in fact, much more sensitive to the details of the temperature structure than has been supposed or would appear in a simple perturbation analysis.

It is only by identifying the important parameters in the atmospheric model used and understanding the details of their inter-relationships that we can hope to accurately constrain that model and determine the CO abundance. It will be shown in this section that a single CO line can be used to constrain the CO abundance only if the temperature structure used is extremely accurate. It shall further be found that by including more information, in the form of a second CO line, we are able to derive not only the CO abundance but the pertinent details of the temperature profile as well.

C H A P T E R I I

OBSERVATIONS

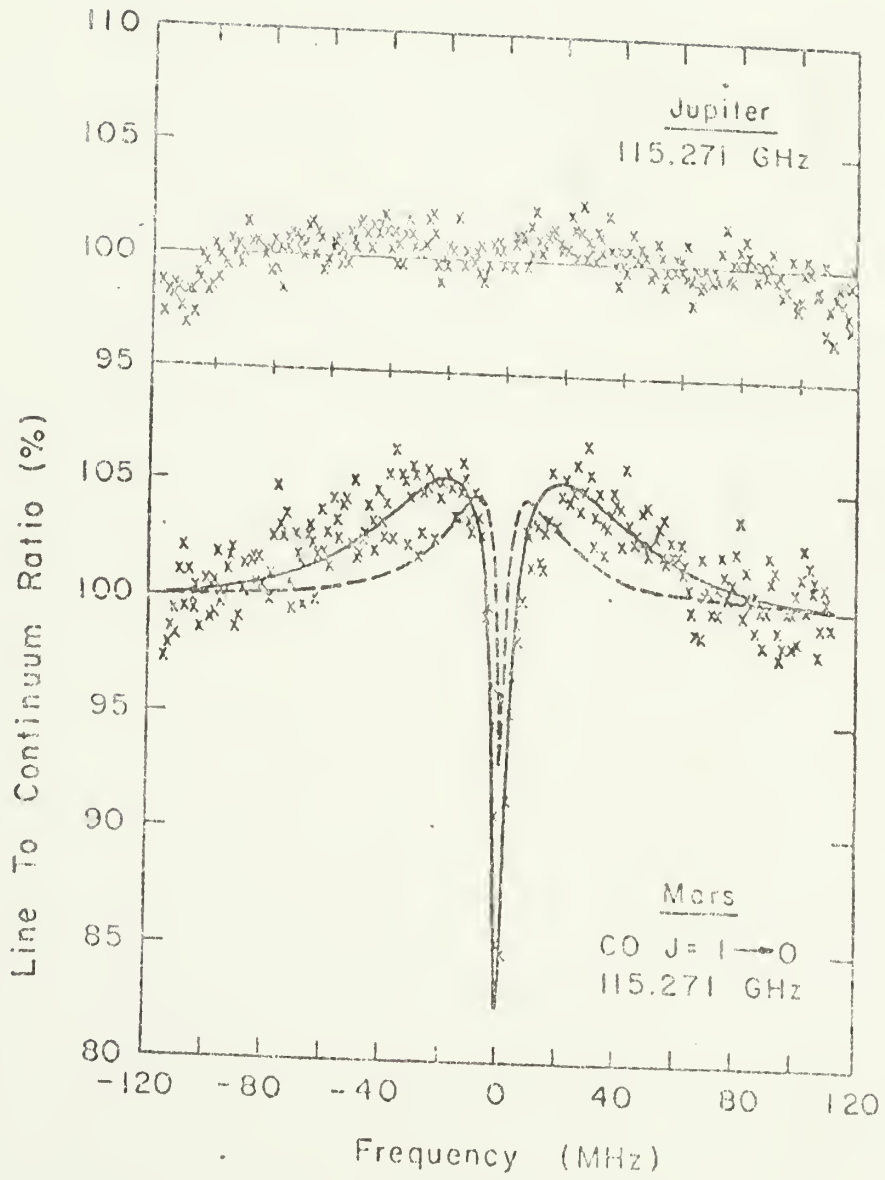
1980 CO(J=1-0) Measurements

Measurements of the line shape of the CO(J=1-0) transition were made with the Five College Radio Astronomy Observatory 14m telescope (HPBW=50 arc sec) at New Salem, Massachusetts on 29 March, 30 March and 1 April, 1980. The receiver was a cooled mixer with a single sideband receiver temperature of 550K and the spectrometer was a 256-channel x 1-MHz filterbank. Data were also obtained with a 256-channel x 0.25-MHz filterbank, though this proved to be of considerably less importance in the analysis because the line is wide enough to be resolved adequately by the 1 MHz filterbank. The observations were made by alternately observing the planet and a position separated by 3 arcmin in azimuth for comparison. In order to reduce the possible effects of standing waves in the spectrum, a quasi-optical phase modulator was used (Goldsmith and Scoville, 1980) and the position of the line in the filterbank was varied by $\pm 1/2$ of the frequency of the standing waves between the subreflector and the feed horn (± 16 MHz). No such effects were detected, and the final average spectrum includes all data, shifted so that the sky frequencies of the individual channels agree. An interferometric SSB filter was used to isolate the signal sideband since failure to reject the image sideband properly

would cause a systematic error in the line-to-continuum ratio. The effect of this on the modeled parameters is negligible since the maximum level of the contamination by the image is about 15 db below the signal. These data were previously analyzed by Good and Schloerb (1981).

The Mars CO line observed in 1980 is shown in Figure 1 with two models from Good and Schloerb (1981) which will be discussed later in the text. The size of the planet (~ 12 arcsec diameter) is much less than that of the beam, and therefore, the spectrum shown is an average over the visible disk. There is no information about the absolute calibration, and we have therefore normalized the data to the continuum level in the far wings of the line. As can be seen from the figure, the line appears in emission in the wings but in absorption near the center of the line. Because such a complicated lineshape, though interesting, could be explained as an effect of the baselines, the systematic baselines have been tested by observing the planet Jupiter during the same time period that the Mars observations were made. This spectrum of Jupiter is also shown in Figure 1. Although it is apparent that there are some residual baseline variations at about the $\pm 1\%$ level, the large emission wings observed in the Mars CO line ($\sim 5\%$) cannot be due to bad baselines. Thus, it is concluded that the observed lineshape of the Mars CO line is mostly real with only small systematic errors at perhaps the 1% level.

Figure 1. 1980 CO(J=1-0) data and curves from the analysis of Good and Schloerb (1981). The Jupiter spectrum is shown as a baseline check. If non-linearities in the detection system were responsible for part of the CO(J=1-0) lineshape, their effects would be observed in this spectrum as well.



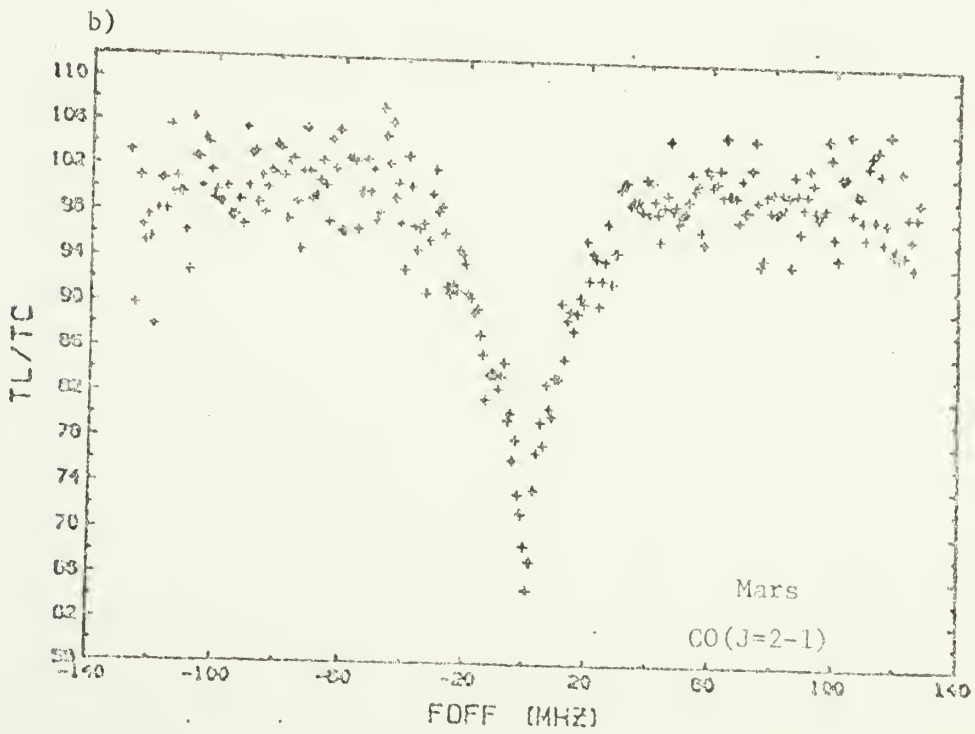
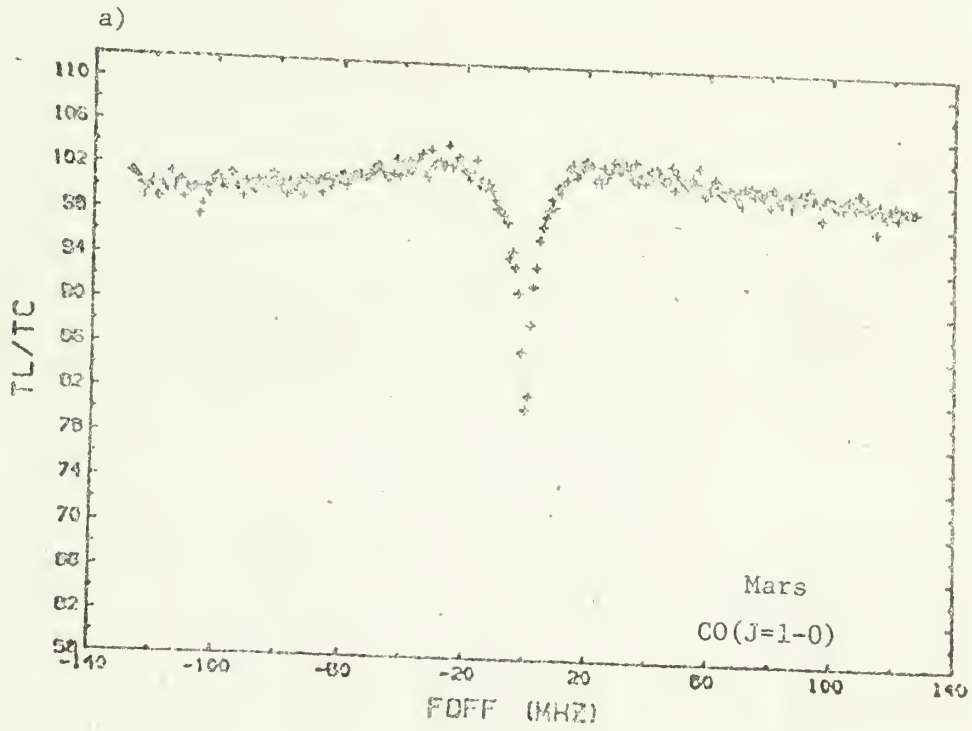
1982 CO(J=1-0) and CO(J=2-1) Measurements

On six dates between December 17, 1981 and March 29, 1982 the martian CO(J=1-0) line was reobserved using the same system and techniques at the Five College Radio Astronomy Observatory as were used for the 1980 CO(J=1-0) observations, though the system temperature had been considerably improved (K). The combined spectrum from these dates is shown in Figure 2a.

The martian CO(J=2-1) line was observed over a shorter time period during this longer span with the Millimeter Wave Observatory (University of Texas) 5m antenna and a cooled receiver developed at the FCRAO. The observations were carried out in February 1982 under good weather conditions using a 256 channel x 1MHz filterbank. No sideband filter was available to separate the signal and image sidebands, so correction for the double sideband response of the receiver has been accomplished by assuming that each sideband contributed equally to the observed continuum. As at FCRAO, the line was shifted periodically within the filterbank to minimize standing waves and the effects of non-linearities in the response of the filters in the filterbank spectrometer. These data are shown in Figure 2b.

Figure 2. a) 1982 CO(J=1-0) line.

b) 1982 CO(J=2-1) line.



C H A P T E R I I I

ATMOSPHERIC MODEL

Radiative Transfer

In order to analyze the data, it was necessary to construct a theoretical line profile based on current understanding of the atmospheric and surface parameters of Mars. It should be noted that other papers have dealt with some aspects of this problem. For instance, the CO line profile is discussed by Wilson et al. (1981) in the appendix to their paper on the CO line in the atmosphere of Venus. The radio emission from a planet with a solid surface is nicely treated in a review of the radio emission from the Moon by Muhleman (1972). These two calculations are now combined to obtain the millimeter CO line profile formed in an optically thin plane-parallel atmosphere above a planetary solid surface, and the approximations used in this section for the analysis of the Mars CO lines are discussed.

The brightness temperature at frequency ν observed with a pencil beam at angle of incidence θ in polarization p of an atmosphere above a surface at temperature T_{surf} is

$$T_{B\nu}(\mu) = (1 - R_p(\mu, \epsilon)) T_{\text{surf}} \exp\left(-\int_0^{\infty} k_{\nu}(z) dz/\mu\right) + \int_0^{\infty} k_{\nu}(z) T(z) \exp\left(-\int_z^{\infty} k_{\nu}(z') dz'/\mu\right) dz/\mu. \quad (1)$$

where $k_{\nu}(z)$ is the absorption coefficient at altitude z and frequency ν , $T(z)$ is the atmospheric temperature profile, μ is the cosine of the angle of incidence θ , and the Rayleigh-Jeans approximation has been adopted. $R_p(\mu, \epsilon)$ represents the well known Fresnel power reflection coefficients (see Muhleman, 1972) which are functions of the angle of incidence, the dielectric constant, ϵ , and the angle between the plane of incidence and receiver polarization.

The present observations of Mars do not spatially resolve the planet, so eqn (1) must be averaged over the visible disk of Mars. The disk average of $T_{B\nu}(\mu)$ is

$$T_{D\nu} = 2 \int_0^1 T_{B\nu}(\mu) \mu d\mu. \quad (2)$$

This allows only a radial dependence for the brightness temperature.

To be completely general, the azimuthal coordinate should be integrated

separately. However, since a model will be chosen where azimuthal variations are averaged out, this form is appropriate for the present discussion. Thus, the observed disk averaged brightness temperature, T_{D_V} , may be computed once $T(z)$, $k_V(z)$, T_S , and ϵ are known or adopted for the model.

Although it may seem obvious, it is important to note that if equations (1) and (2) are divided by T_{surf} (the value of the continuum) almost all absolute temperature information is lost. This means that uncalibrated spectral information, such as the line-to-continuum data presented here, can give us no more than relative temperatures - the atmospheric temperature structure and the surface temperature are almost exactly correlated. This is not surprising, nor does it have a strong influence on the solution of the problem. The absolute temperature of the martian surface is fairly well known from the Viking measurements, and small errors produced by using this value will not have an extreme effect on any of the important parameters used in the model.

Finally, it should be noted that the absorption coefficient and temperature profiles appear together as a functional in Equation 1. To a certain degree, it is only the product of these two that can be constrained at any given height. This limits the extent to which the mixing ratio (in the absorption coefficient) and the temperature structure can be separated. It should not be surprising, then, that errors

in the assumed values of the temperature structure will have a dramatic impact on the CO abundance deduced.

Absorption Coefficient of CO

The value of the absorption coefficient in the atmosphere of Mars is related to the temperature, pressure and mixing ratio of CO. The total optical depth of CO₂ at 115 GHz is on the order of 10⁻³, and its contribution in the calculation of $k_\nu(z)$ may therefore be ignored. The absorption coefficient of the CO(J=1-0) transition is given by

$$k_\nu(z) = k_\nu(T(z), P(z), X(z))$$

$$= \frac{8.931 \times 10^9 P(z) X(z)}{T(z)^3} \Phi(\nu, \nu_0, P(z), T(z)) \text{ km}^{-1} \quad (3)$$

where $P(z)$ and $X(z)$ are the pressure (in millibars) and mixing ratio profiles respectively, ν_0 is the line frequency, and $\Phi(\nu, \nu_0, P(z), T(z))$ is the normalized line profile function in units of MHz⁻¹ (Wilson et al., 1981). The CO(J=2-1) absorption is a factor of eight stronger, a factor which will have important ramifications later.

At high pressures, the CO lines are pressure broadened and the line shape is a Lorentzian. (A Van Vleck-Weiskopf line shape is appropriate if the line width is comparable to the line center fre-

quency. However, in the atmosphere of Mars, the line width at the surface pressure is approximately 10^{-4} of the line center frequency, and under these conditions a Lorentzian line shape is identical to the Van Vleck-Weisskopf shape.) The pressure broadened line width for CO given in Wilson et al.'s appendix (1981) has been adopted and is given by

$$\Delta\nu = 3.3 \times 10^{-3} P (T/300)^{0.75} \text{ GHz} \quad (4)$$

At very high altitudes (above about 70 km on Mars), Doppler broadening dominates pressure broadening and the line shape is Gaussian with the Doppler line width (about 75 kHz for the martian stratosphere). At intermediate pressures, where the pressure broadened line width is comparable to the Doppler width, the proper line profile is the Voigt profile, which is a convolution of the Gaussian and Lorentzian line shapes. Although this profile was used in the fitting, further examination of the Lorentzian profile will expose some interesting relationships between the parameters.

Since these lines are pressure broadened, the linewidth is given by

$$\Delta\nu = \Delta\nu_1 P, \quad (5)$$

where $\Delta\nu_1$ is the linewidth at unit pressure and P is the pressure at the height of interest. If the temperature structure and atmospheric composition are fixed, the pressure at any height is proportional to the surface pressure, P_0 , as is the linewidth. The line profile function is given by

$$\Phi(\nu, \nu_0, P, T) = \frac{\Delta \nu}{(\nu - \nu_0)^2 + \Delta \nu^2} \quad (6)$$

As long as the linewidth is smaller than the offset from line center, the line profile function is also proportional to the surface pressure. This in turn implies that the absorption coefficient in Equation 3 is proportional to XP_0^2 . Thus, it can be concluded that changes in the mixing ratio and the surface pressure have very similar effects on the spectrum and will be very strongly correlated in any model fitting to the millimeter lines. To see this, consider the effect of changing both so that the above product is preserved. Except for a secondary pressure effect in the lineshape, the absorption coefficient will remain unchanged. Since the temperature structure also has been preserved, the observed line also will be unchanged. This point will become important when the observed lines are fit.

From the above discussion, it is apparent that although there are many parameters in the model, many of them have very similar effects on the lineshape and may be highly correlated. This correlation can be advantageous since it can decrease the complexity of the system to be determined. For example, the correlation between the surface pressure and the CO abundance simplifies the analysis by removing one variable and giving a relationship between an error in the value of the surface pressure chosen and the CO abundance deduced. However, it can also prove difficult by hiding those variables that are the most important to tie down. As it turns out, the main reason for attempting to fit

both the CO(J=1-0) and CO(J=2-1) lines simultaneously will be to provide the extra, sufficiently-independent constraint needed to determine both the atmospheric temperature and the CO abundance uniquely. This becomes possible because the CO(J=2-1) line probes the martian atmosphere at a different, though overlapping, set of heights. In doing so, it resolves the functional relationship between the temperature structure and the absorption coefficient noted in the last chapter.

Viking Measurements - Constraints on the Model

As was pointed out in the Introduction, the possible complexity of the atmospheric model can be enormous. In order to establish a benchmark and to determine some of the parameters that must be used in the model, the Viking entry probe data must be examined. Although these data represent only one season and a small latitude range, they do provide a useful starting point.

The Viking entry data and Lander meteorology experiments show that there is a great deal of vertical structure to the temperature profile but also that it follow a general trend. Since these measurements were limited both in time and latitude, we have used these trends only to guide our initial attempts at defining a temperature model. The temperature of the atmosphere at the surface is fairly stable with 220K as an approximate daytime disk average and large diurnal variations ($\pm 20K$;

Hess et al., 1977), though the effects of these on our model should be smoothed considerably by disk averaging. The atmospheric temperature decreases linearly with height to a constant value of about 135K above 60 km, where our sensitivity to CO in the atmosphere is diminished.

For simplicity, it is assumed initially that the temperature of the surface itself was the same as that of the atmosphere just above (220K). This is not always the case on Mars since the surface radiatively cools during the night far more efficiently than the atmosphere above it. Thus, in the early morning, the surface temperature is less than the gas just above it. Conversely, sunlight heats the surface during the day causing the afternoon surface temperatures to be greater than the atmospheric temperatures. Because all the data were obtained on the day side of the planet and represent a disk average, the adoption of equality between the atmospheric and surface temperatures seems reasonable. Since Viking determined the thermal properties of the surface, the surface temperature at each point on the surface could in principle be computed and used in the model as Clancy et al. (1983) have done. Alternatively, these same calculations could be used to estimate a mean surface temperature for use in the present analysis. Clancy et al. have shown that it is unnecessary to calculate each point separately - a disk average will suffice. In any case, once a particular value is adopted, its exact value becomes somewhat unimportant as it is the ratio of the atmospheric temperatures to the surface temperature that is important in the formation of these lines.

The surface dielectric constant, which specifies the emissivity and polarization of the emission from the surface, was adopted to be 2.5 (Cuzzi and Muhleman, 1972). Since our observations were made on an alt-az telescope with polarization fixed parallel to the azimuth axis, Mars rotated with respect to the plane of polarization of the receiver during the observations. Thus, each point on the martian surface was observed with a range of polarization angles, and in this analysis the average of the parallel and perpendicular polarizations for R_p has been adopted at all points on the disk. It should be noted that this would be the case in any event due to disk averaging (see below), because the analysis has been simplified by making the surface isothermal. The disk temperature of the nominal model then becomes 198K. Finally, any uncertainties introduced by these assumptions will affect the results in the same way that uncertainties in the adopted surface temperature do. Thus, the particular choice of the surface temperature and emissivity should have only a minor effect on the formation of the line.

C H A P T E R I V
MODEL FITTING TO THE CO(J=1-0) LINE

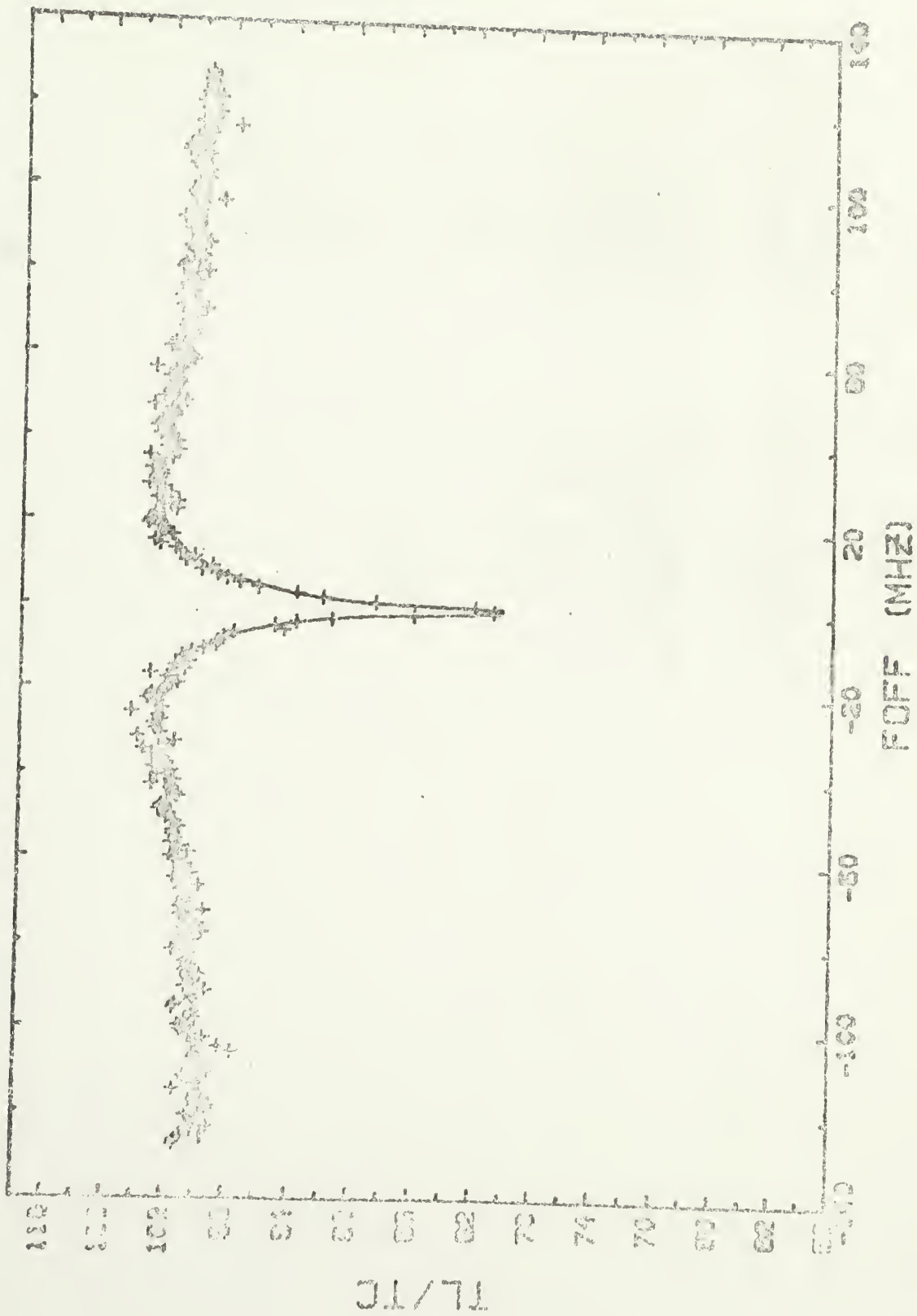
As a simple first approximation to the martian atmospheric temperature structure, it was assumed that the atmospheric lapse rate was constant in the lower part of the atmosphere. The first model therefore contained only five parameters: the CO mixing ratio (assumed constant throughout the atmosphere), the surface temperature, the temperature and pressure of the atmosphere at the surface and the temperature lapse rate. Although a constant stratospheric temperature was originally included in this list, it turned out that the CO lines were formed entirely below that region, so that this parameter could not be defined. As has been stated before, the atmospheric temperature structure and the surface temperature were assumed to be the same for all points on the disk.

The original reduction of the 1980 CO(J=1-0) data (Good and Schloerb, 1981) used this same model. As was mentioned in the Introduction, that work used a set of fixed temperature profiles to derive the most likely CO mixing ratio and the uncertainty in this quantity. This model fit the data extremely well and produced an abundance that was plausible. Therefore, in the absence of any internal inconsistencies or external contradictions, a more complicated model did not seem warranted by the available data. The model curves

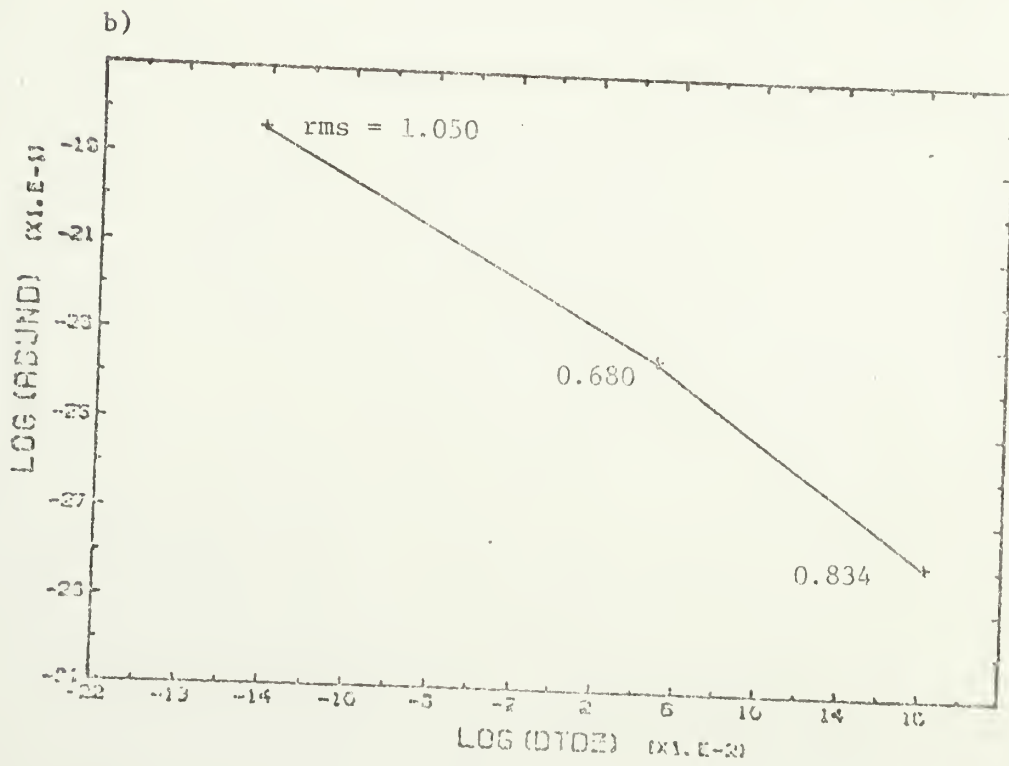
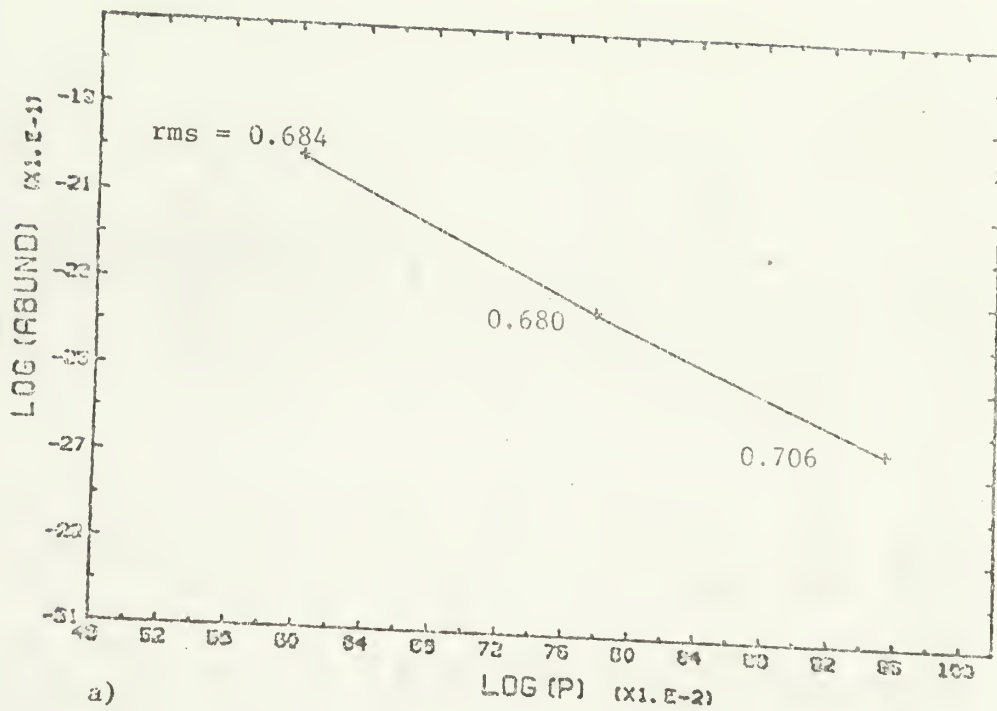
plotted in Figure 1 are from this work. The better model in the figure is for the best fitting CO abundance of 3.2×10^{-3} . For comparison, the spectrum predicted for the same atmosphere and a mixing ratio of 8×10^{-4} (the infrared result) was also calculated and shown in the figure.

In the present analysis of the 1982 CO(J=1-0) data, the temperature structure is not fixed but rather is solved for at the same time as the CO mixing ratio. When the model was fit to the line, it produced an extremely good fit and values for the CO abundance that were consistent with Good and Schloerb (1981) (Figure 3). A more important feature of the analysis, however, was that an indication of the importance of individual parameters and the relationships between them could be derived. As may be expected from the discussion of the line forming process presented in the last chapter, even the five parameters in this simple model cannot all be determined simultaneously. An almost exact correlation exists between the mixing ratio and the surface pressure, with a change in the mixing ratio mimicked by a change in the inverse square of the surface pressure. Figure 4a shows the mixing ratio fit to the CO(J=1-0) for various choices of the surface pressure, all other parameters held constant. Any choice is equally valid from the standpoint of the data, so a standard value of 6.5 mbars has been adopted for the surface pressure (Seiff and Kirk, 1977). As was also anticipated, the surface temperature and the temperature of the atmosphere at the surface were found to be exactly correlated.

Figure 3. Constant lapse rate model fit to the 1982 CO(J=1-0) line.



- Figure 4. a) Best fit CO mixing ratio vs assumed surface pressure for the 1982 CO(J=1-0) line.
- b) Best fit CO mixing ratio vs assumed lapse rate for the 1982 CO(J=1-0) line.



Thus there are, in effect, three independent parameters in the simplest model: the CO abundance, the temperature of the atmosphere at the surface, and the temperature lapse rate. The other two parameters must be assumed, though the effect of these assumptions can be analyzed using the above relationships. Also, as indicated by the previous analysis, although these relationships were determined from the simple model, they are equally valid for more complicated ones. The values of the parameters fit to the data and their correlations are given in Table 1.

Although it has been shown that a CO mixing ratio and the two parameters defining the simple temperature structure may be determined from the data which fit the line, it has not been shown that the abundance that is determined is insensitive to the details of the temperature structure. Rather, it has been found that under the assumption of a constant lapse rate, both that lapse rate and the CO abundance are tightly constrained. It still remains quite possible that under different assumptions about the structure in the temperature profile an equally good fit could be obtained with a different abundance. As an indication of the importance of the details of the temperature structure, Figure 4b shows that if an alternative lapse rate is imposed on the model, the best fit mixing ratio is strongly affected and the fit is badly degraded.

To illustrate this effect more substantially, a series of temperature models have been fit to the CO(J=1-0) line. The atmosphere

Table 1. Results of Fitting Model
to 1982 Mars CO(J=1-0) Line

Fixed

Surface Pressure = 6.5 mbar

Surface Temperature = 220 K

Fitted

CO Mixing Ratio = $(4.1 \pm 0.4) \times 10^{-3}$

Atmospheric
Temperature at Surface = 220.5 ± 0.7 K

Lapse Rate = 1.11 ± 0.04 K/km

Correlation Coefficients

Abundance - Lapse Rate = -0.72

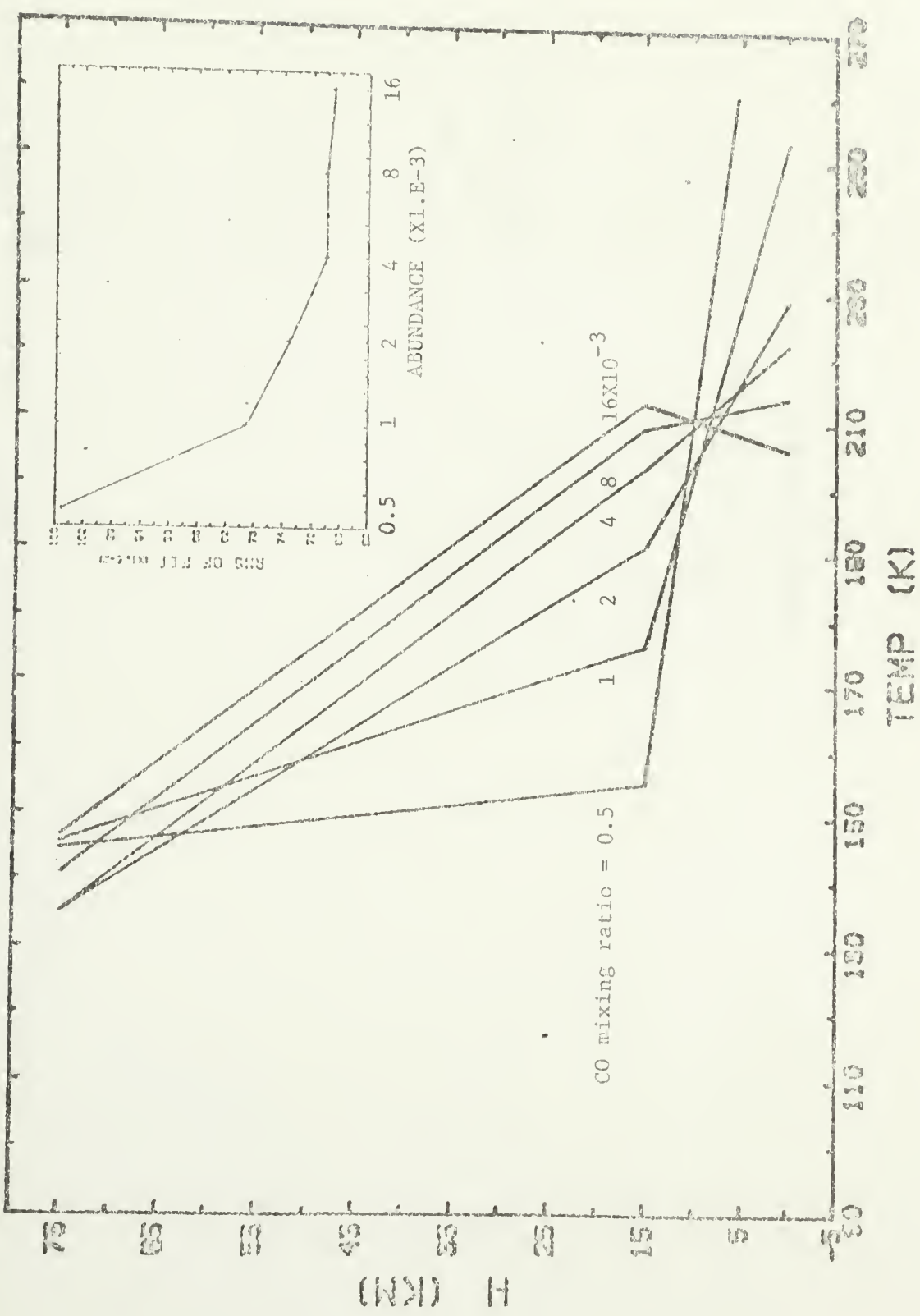
Abundance - Temperature = +0.32

Temperature - Lapse Rate = +0.33

was assumed to be composed of two parts, each having a constant lapse rate, divided at a predetermined height (15 km). With this still fairly simple model, it was found that a temperature model could be obtained to fit any CO abundance above about 10^{-3} (Figure 5). This implies that unless the temperature structure can be independently constrained, there can be no claim to have determined the CO abundance. Furthermore, the sensitivity of the deduced CO mixing ratio value to the temperature profile chosen is extreme, and even a fairly detailed profile, such as the mean profile based on the Viking data use by Clancy et al. (1983), could force a substantial error in the deduced CO abundance if it does not fairly characterize the temperature structure at the time of the observations.

In the Introduction to this section, the discrepancy between the CO abundances found by different researchers fitting the same line (Good and Schloerb, 1981; Clancy et al., 1983) and by fitting two different lines separately (Clancy et al., 1983) was discussed. The above analysis suggests that this could be due to differences in the assumed temperature structure. With the benefit of hindsight, it would seem that this should have been obvious. The lines are optically thick at line center and might better be used to find the temperature structure, precisely because the emitted radiation is so sensitive to this profile. Thus, in order to derive abundances, the temperature structure must first be determined or specified accurately. This cannot be done with one CO line alone.

Figure 5. Two lapse rate temperature profiles from fits to the 1982 CO(J=1-0) line with the CO mixing ratio fixed at different values. Inset shows the rms of the fits.



C H A P T E R V
SIMULTANEOUS FITTING OF TWO CO LINES

The information necessary to constrain both the CO mixing ratio and the atmospheric temperature structure can be obtained by fitting both the CO(J=1-0) and CO(J=2-1) lines simultaneously. The temperature structure may have some temporal variability, though on the basis of the similarity between the current CO(J=2-1) line and that of Clancy et al. (1983) and between the 1980 CO(J=1-0) and 1982 CO(J=1-0) lines, these variations are not likely to be extreme. We therefore have some justification for postulating a time-independent temperature mean temperature structure for the planet for the purpose of the model. The current observations of the CO(J=1-0) and CO(J=2-1) lines overlap in time, although the CO(J=1-0) data were obtained over a much longer time than were the CO(J=2-1). Nevertheless, the possibility of significant variations during the observations is very real, and future observations of the two lines should be made concurrently to avoid any possible bias.

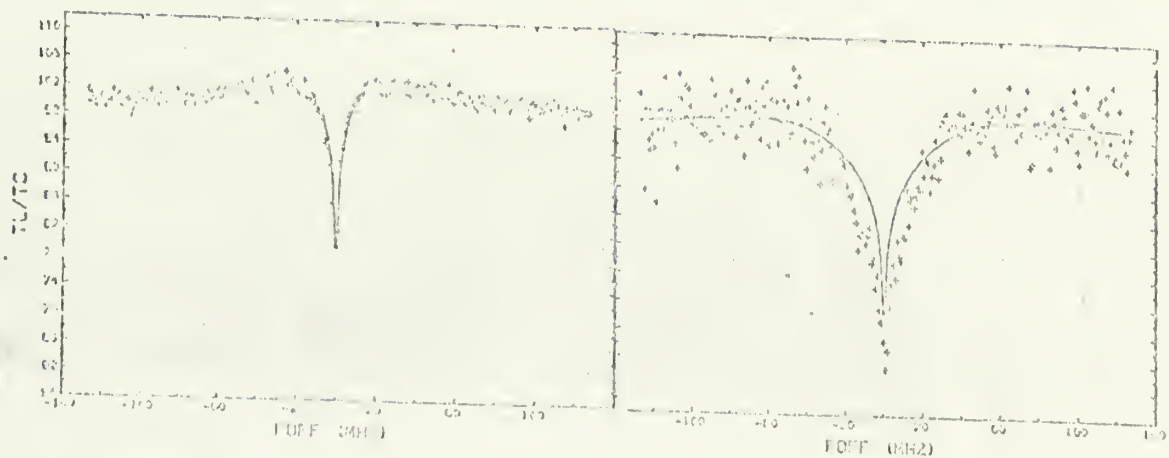
The fits to the two lines simultaneously in this chapter are summarized in Table 2. Initially, we return to the simple atmospheric model with a single constant lapse rate. As should be expected on the basis of the previous discussion, it proved quite easy to fit either of the CO lines individually (Figure 6, Table 2). However, the best fit

Table 2. Results of Simultaneously Fitting Model to 1982 Mars CO(J=1-0) and CO(J=2-1) Lines

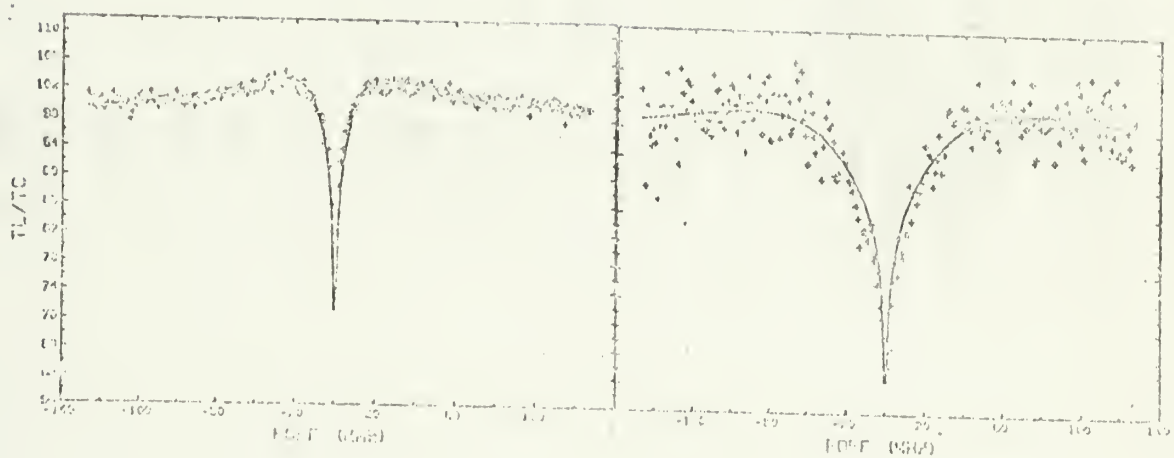
Temperature Model	Mixing Ratio($\times 10^{-3}$)	Figure for Model	RMS			
			Simultaneous		Individual	
			1-0)	(2-1)	(1-0)	(2-1)
Linear	3.55 ± 0.13	6	1.29	3.22	0.69	3.15
Two Lapse Rate	1.02 ± 0.05	7	1.01	3.11	0.70	3.05
Multiple Lapse Rate	0.99 ± 0.05	8	1.01	3.06	0.71	3.02
Multiple Lapse Rate (variable T_{surf})*	0.81 ± 0.04	9	0.77	3.02	-	-

* In the last model the surface brightness temperature for the CO(J=1-0) line was 9.1 ± 0.7 K less (96% of) that for the CO(J=1-0) line (220 K).

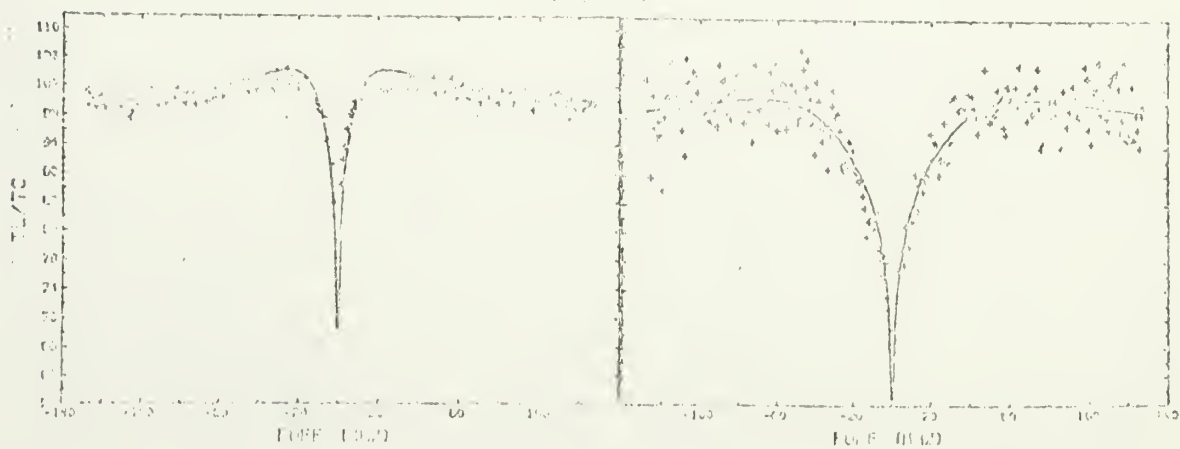
Figure 6. a) Constant lapse rate model fits to the 1982 data.
b) Corresponding temperature profiles.



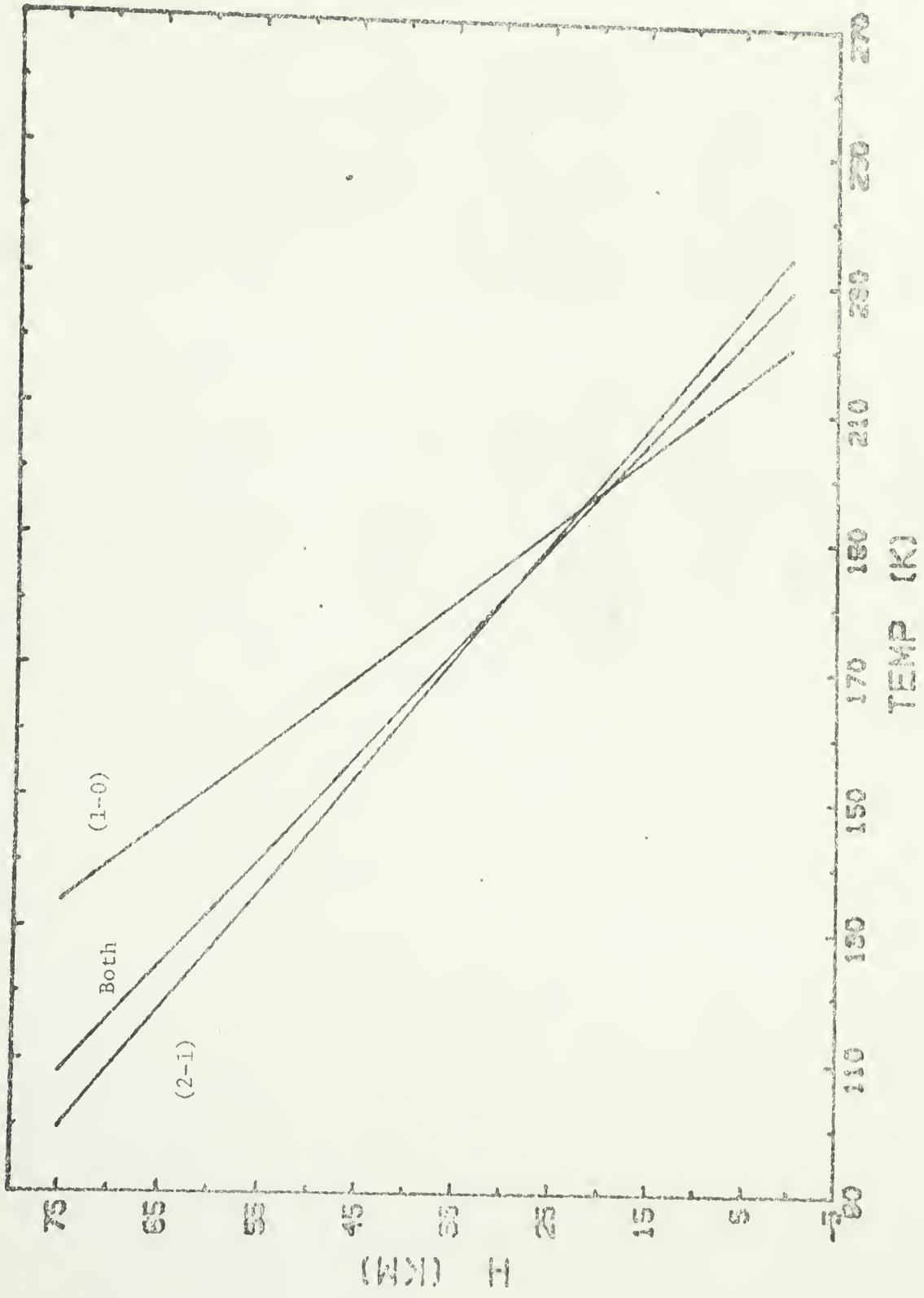
Fit to CO(j=1-0)



Fit to Both



Fit to CO(J=2-1)

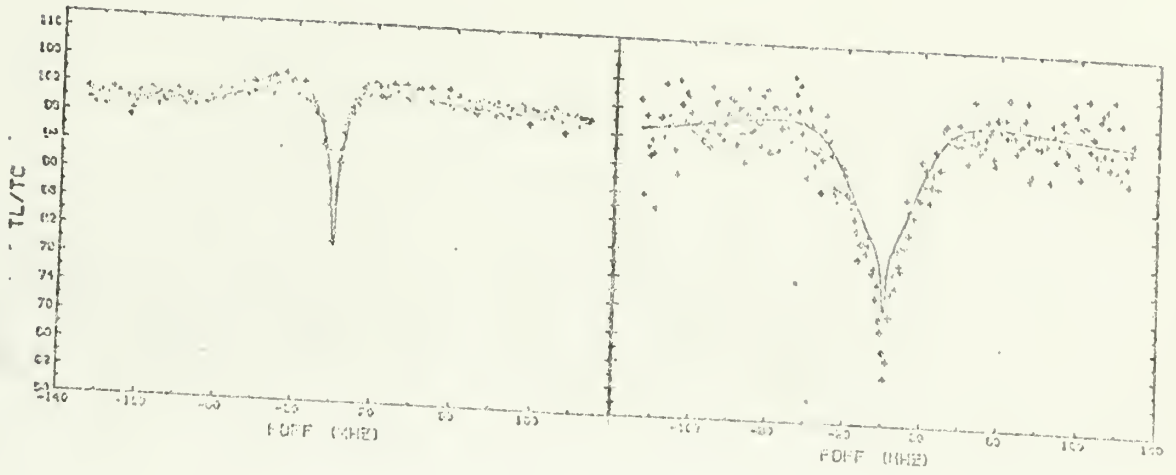


parameters (in particular the temperature structures deduced) for these two lines agree badly and, not surprisingly, a fit to the two lines simultaneously is also poor. This inability to achieve consistent results is a clear indication that the choice of a model must be at fault; we are therefore forced to increase its complexity if we are to fit both lines with the same atmosphere.

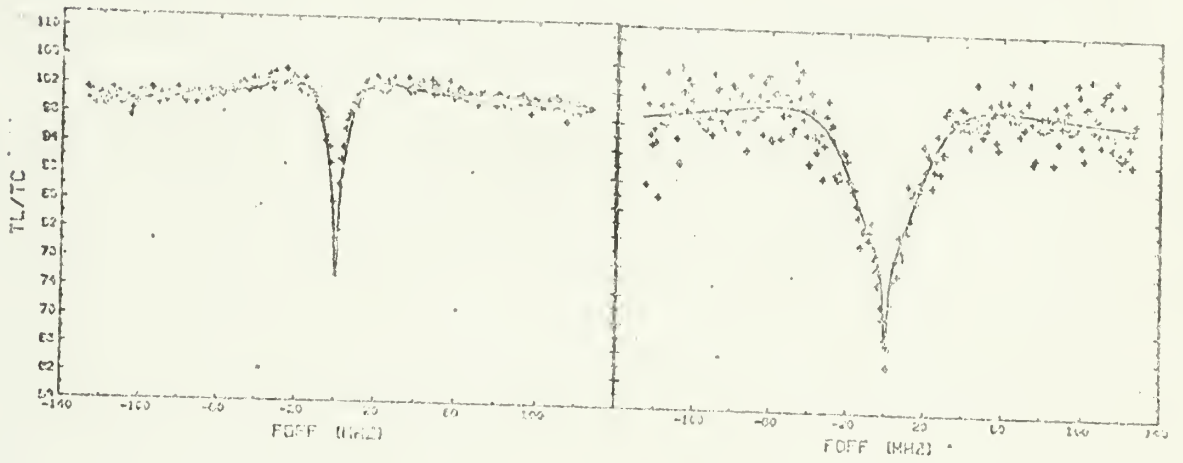
In principle, the model may be refined by introducing additional structure into either the CO mixing ratio profile or the temperature profile. In this work, it has been decided to maintain a constant CO mixing ratio and allow the temperature to vary for two reasons. First, significant structure in the former is more likely (McElroy and Donahue, 1972). Second, in an optically thick line the temperature profile more strongly influences the emission. The form of this added structure was chosen to be the same as was used for the CO(J=1-0) line fitting in the previous chapter: two lapse rates which change at 15 km. (Tests have shown that this choice of heights does not bias the results to any substantial degree.)

The results of a fit of this model to the CO(J=1-0) and CO(J=2-1) lines simultaneously are shown in the second line in Table 2. In this case it proved to be possible to fit both lines to about the limit of the noise - as indicated by the fit of the model to each line separately (Figure 7, Table 2). Interestingly enough, the CO abundance obtained with this model is less than a third of that found with the

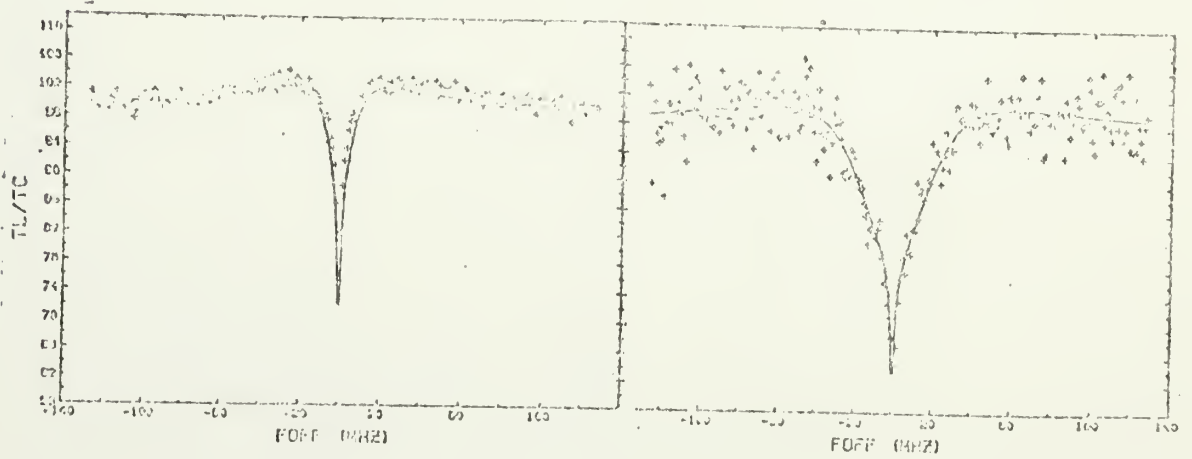
Figure 7. a) Double lapse rate model fits to the 1982 data.
b) Corresponding temperature profiles.



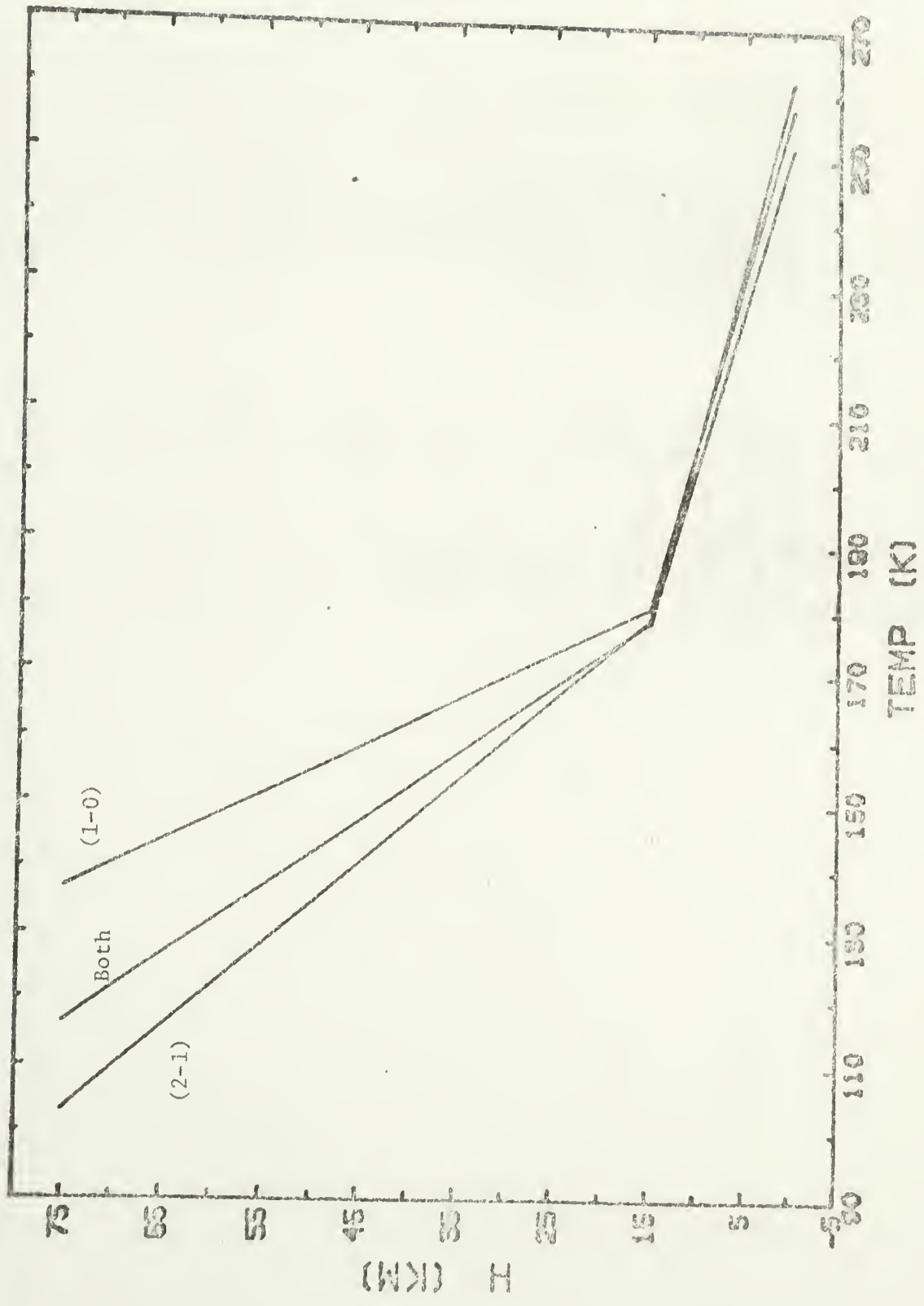
Fit to CO(J=1-0)



Fit to Both



Fit to CO(J=2-1)

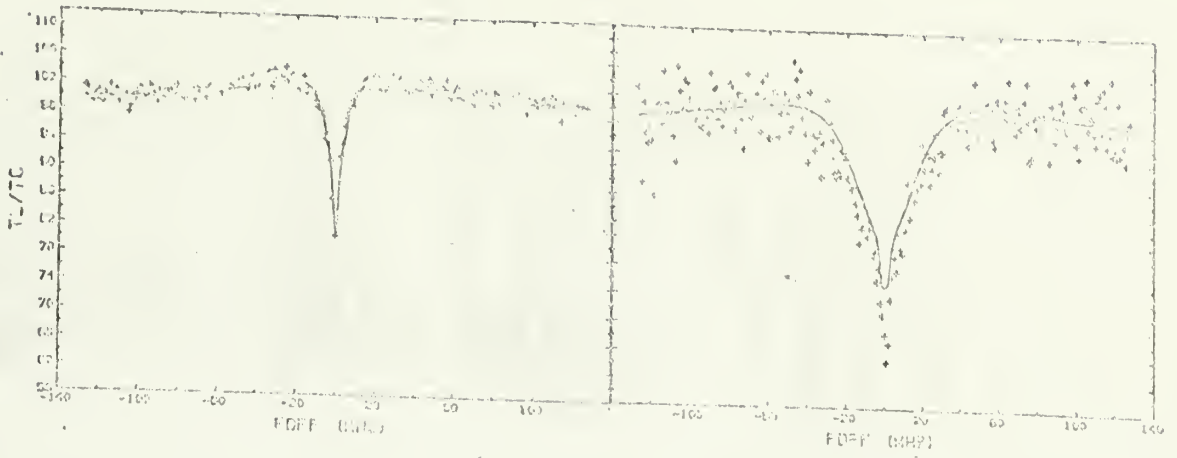


simpler model and, therefore, is close to that found from the infrared lines (Kaplan et al., 1969). In addition, a fit of the two lines individually using this mixing ratio yields more consistent results for the temperature structure, although there are differences in the upper atmosphere above the bulk of the CO. Thus, additional structure in the atmospheric temperature leads to a better fit and more consistent results. However, the inaccuracy in the simultaneous fits to the two lines is still enough to warrant further attempts at fitting and, correspondingly, a more complex model.

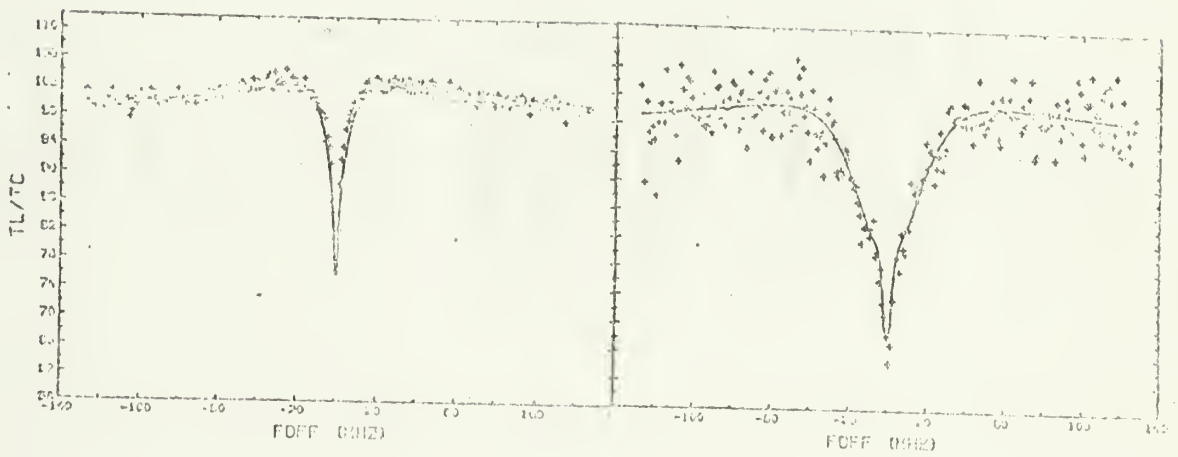
Continuing the process of adding structure to the temperature profile, the two CO lines are next fit using a model with four lapse rates. The temperature is linearly interpolated between fit points every ten kilometers (about one scale height) up to fifty kilometers. The temperature at height zero was not used as an explicit parameter but extrapolated from above because it proved to be insensitive and unstable. Also, the temperature above fifty kilometers altitude was constrained to be within five degrees of that at fifty, although this actually had no effect on the fit since the model is insensitive to the temperature structure in this region.

The results of the fits to the lines simultaneously are given in the third line of Table 2 and the models are plotted with the data in Figure 8. As may be seen in the table, the mixing ratio deduced was not significantly different from that found using the two lapse rate

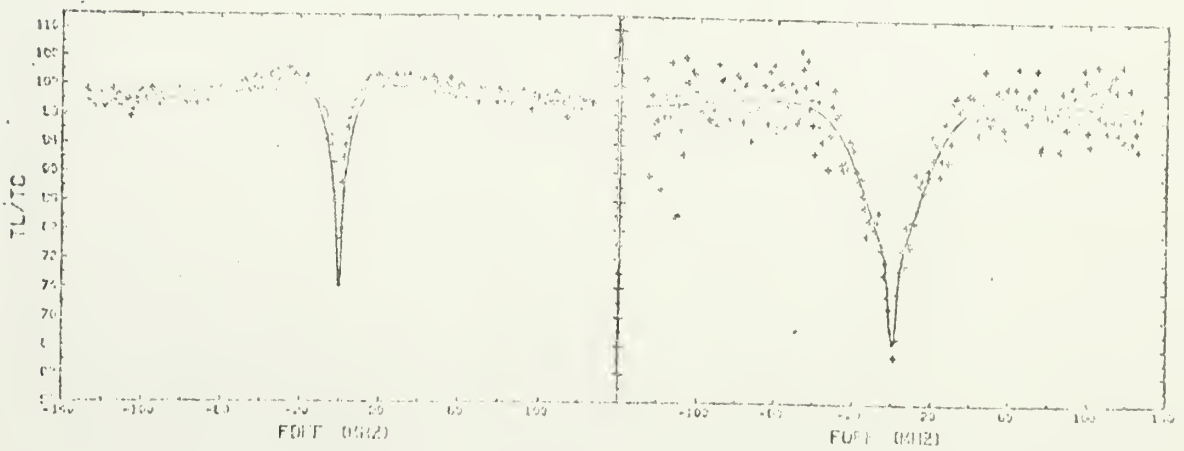
Figure 8. a) Multiple lapse rate model fits to the 1982 data.
b) Corresponding temperature profiles.



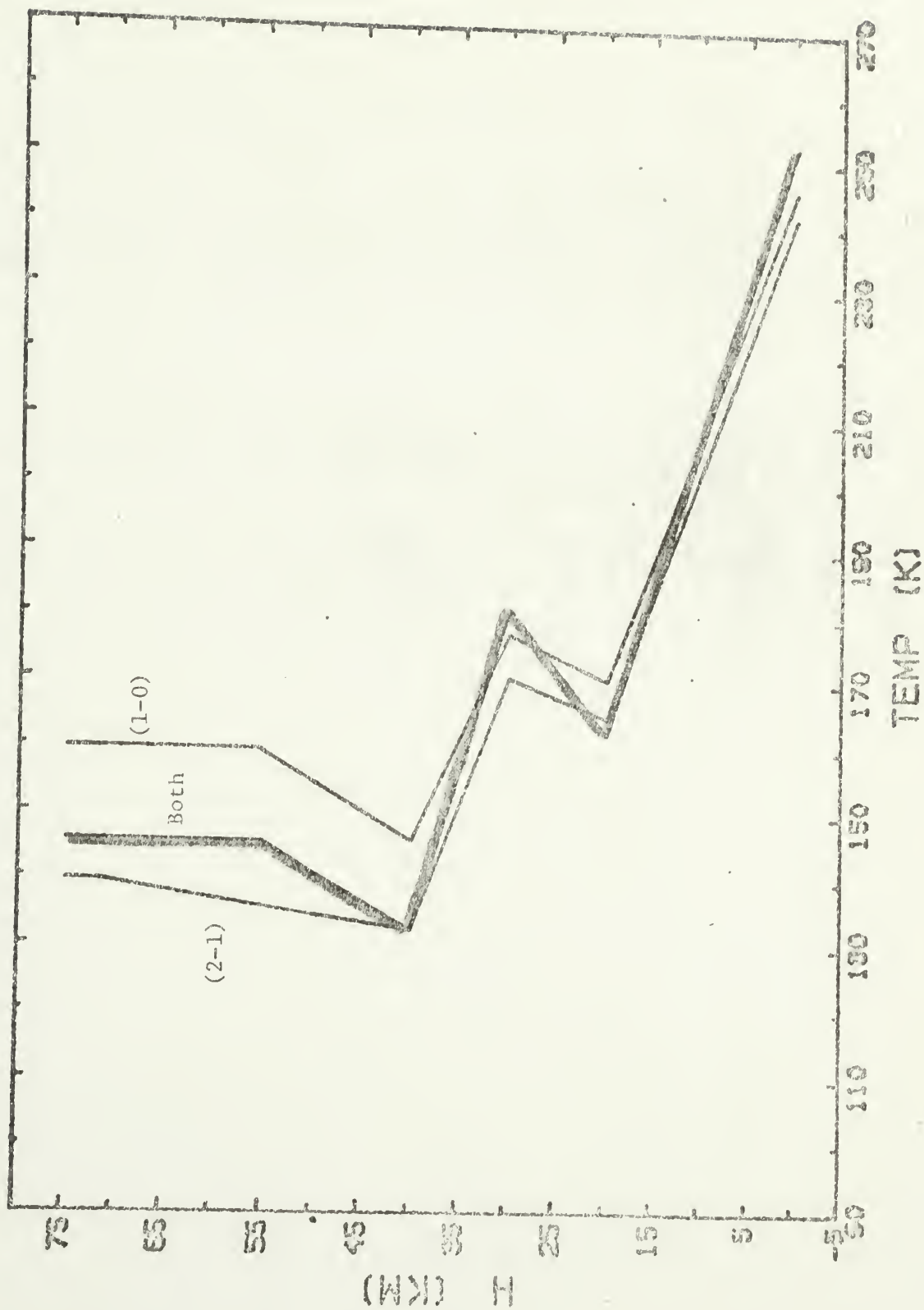
Fit to CO(J=1-0)



Fit to Both



Fit to CO(J=2-1)



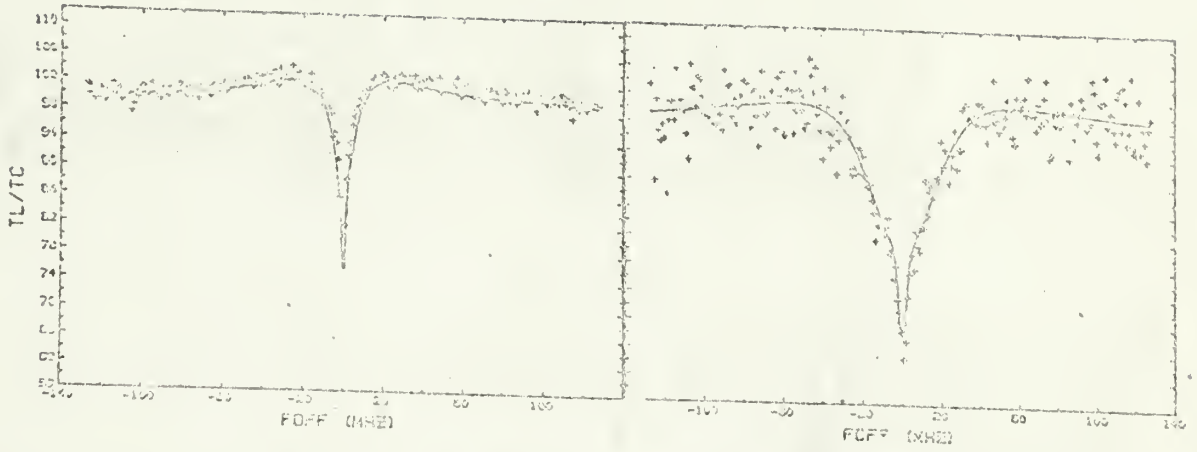
model and the temperature profile, although containing more structure, was also similar to that of the previous model. Thus, overall, the simultaneous fit to the two lines was not significantly better than that of the two lapse rate model. However, when the two lines are fit separately, the two temperature profiles found are quite similar in shape. Also significant is the fact that only small perturbations of the simultaneous fit temperature profile are needed to fit the two lines individually since this implies that minor differences in the temperature structure at the times of the two observations may account for the difference.

In the region below forty kilometers, the difference between the CO(J=1-0) fit temperature profile and that for the CO(J=2-1) line is more accurately described as a temperature displacement, with the CO(J=2-1) profile being consistently cooler than the CO(J=1-0). Such a difference could be accounted for by a difference of about ten degrees in the surface brightness temperature at the two frequencies, and in fact such a difference might be anticipated as the two frequencies see substantially different depths below the planet's surface. On the other hand, even with this shift there would remain a difference in the temperature profiles above forty kilometers, primarily to account for the depths of the center channels of the two spectra. Because the two spectra were not, in fact, taken exactly concurrently and because there appears to be temperature structure in the atmosphere with an amplitude of about twenty degrees, this difference may reflect temporal variations in the temperature profile.

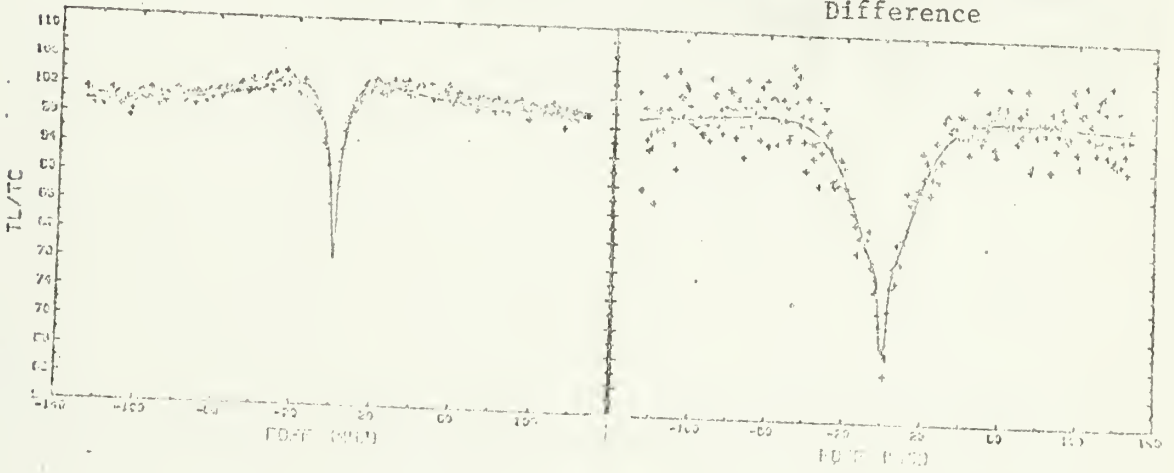
The above analysis suggests that the fits could be improved if T_{surf} were slightly different at the two frequencies. Therefore, an extra parameter was added to the model: a surface temperature difference between the two frequencies. As before, the surface temperature for the CO(J=2-1) line was fixed at 220K and the CO(J=1-0) temperature was allowed to vary in order to produce the best fit. With the inclusion of this last parameter, we were able to fit both the CO lines simultaneously to the noise. These fits are summarized at the bottom of Table 2 and shown in Figure 9. The CO(J=1-0) surface temperature was found to be $9 \pm 1\text{K}$ cooler than the 220K CO(J=2-1) surface temperature, consistent with calculations of the millimeter wavelength spectrum by Cuzzi and Muhleman (1972).

Both lines have now been fit with a set of parameters that seem reasonable. However, that same conclusion was reached by both Good and Schloerb (1981) and Clancy et al. (1983) when they fit the CO(J=1-0) line alone and obtained different results. The fact that such a detailed model had to be invoked here suggests that a similar bias is probably not operating, but it would be preferable to have more substantial evidence on this point. As a test of the reliability of the program for the retrieval of the CO mixing ratio and temperature structure, a simulation was run; the spectra predicted for a given parameter set, plus noise to simulate the actual signal-to-noise ratio of the lines, were fit and the input parameters retrieved. The CO

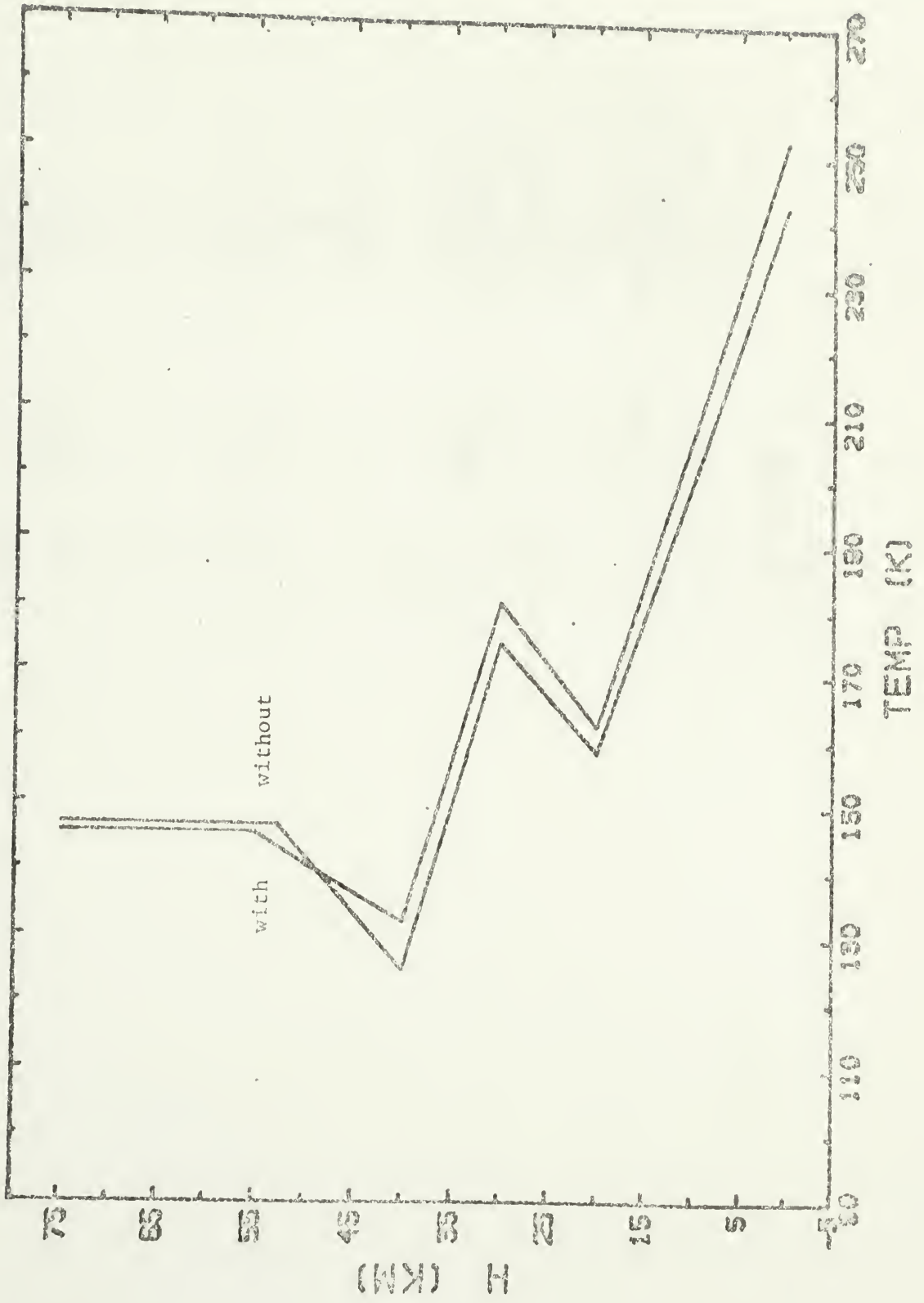
Figure 9. a) Surface temperature offset model fit to the 1982 data.
b) Corresponding temperature profiles.



Fit to Both without
Surface Temperature
Difference



With Difference



mixing ratio was set at 2×10^{-3} and an approximation to the Viking 1-entry-data atmospheric profile defined the temperature structure. This profile was chosen for two reasons. First, because it represents an actual measurement at one point on the planet, it is a likely profile. Second, its structure is relatively incompatible with the multiple lapse rate parametrization used above as the places in the atmosphere where the lapse rate actually changes do not occur at the same heights it is allowed to change in the model. This last attribute is of particular importance because it tests the need for the complexity in the model profile and gives an indication of the errors in the retrieved profile.

The simulated data were fit in the same way as the real measurements, using the single lapse rate, two lapse rate, and multiple lapse rate models. The results of these fits are presented in Table 3. As with the real data, the single lapse rate model overestimates the CO abundance, although here the simultaneous fit to the data (Figure 10) is actually quite good. The two lapse rate model fits both lines only slightly better but the temperature structure retrieved is a better approximation to the original profile. The fit to these data with the multiple lapse rate model is not appreciably better but the retrieved model parameters are quite interesting. Each of the line segments that make up the model cross the true profile near their midpoint. However, the points at which the lapse rates change can differ from the true profile by as much as 13K - the arbitrary form imposed on the model

Table 3. Results of Simultaneously Fitting Model to Simulated Mars CO(J=1-0) and CO(J=2-1) Lines

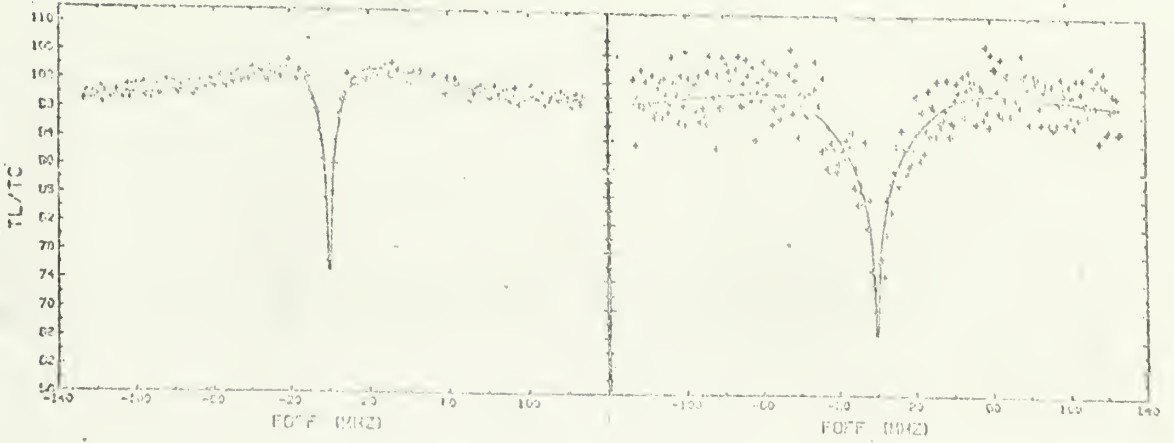
Temperature Model	Mixing Ratio($\times 10^{-3}$)	RMS	
		(1-0)	(2-1)
Linear	2.92 ± 0.13	0.61	3.01
Two Lapse Rate	1.95 ± 0.12	0.61	2.99
Multiple Lapse Rate	1.99 ± 0.12	0.61	2.95

The retrieved profiles are shown in Figure 10.

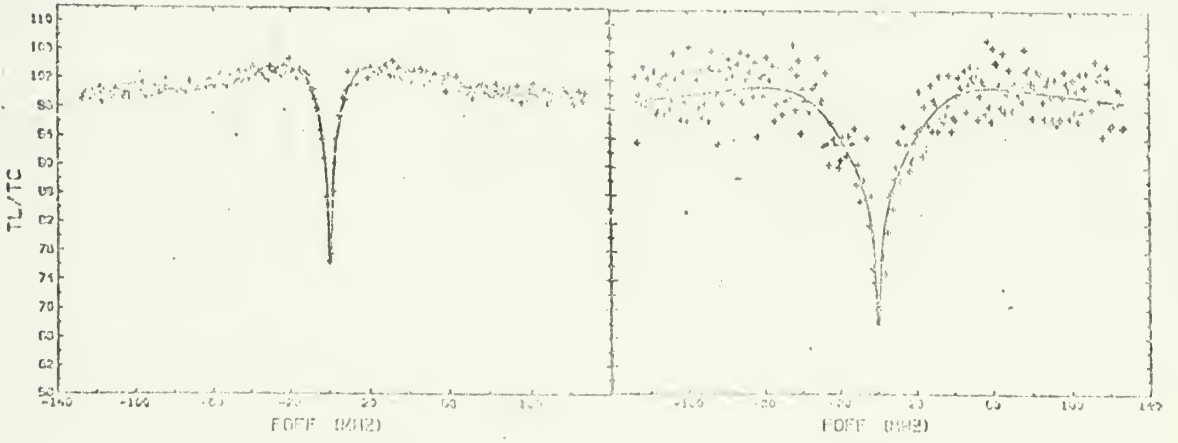
Actual CO abundance was 2×10^{-3} .

Figure 10. a) Fits to the simulated data.

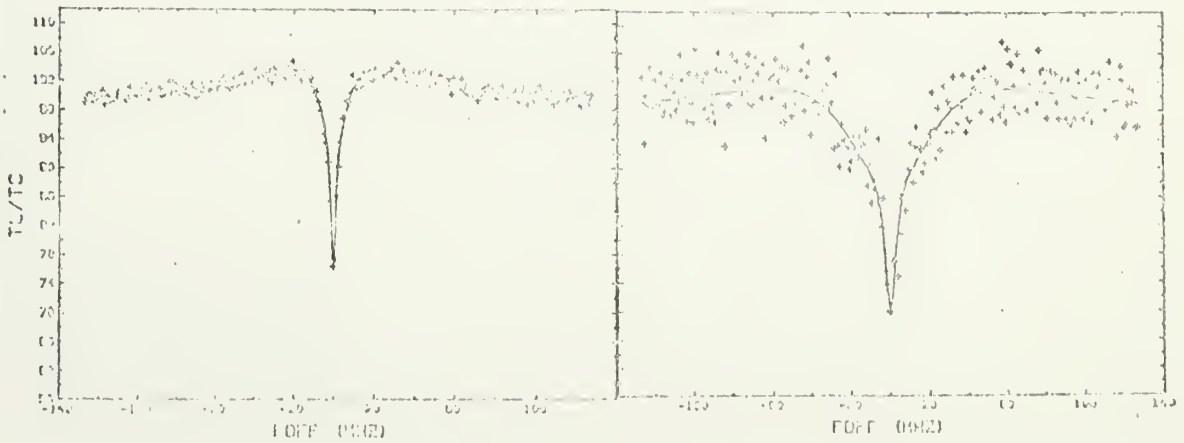
b) Corresponding temperature profile and true structure.



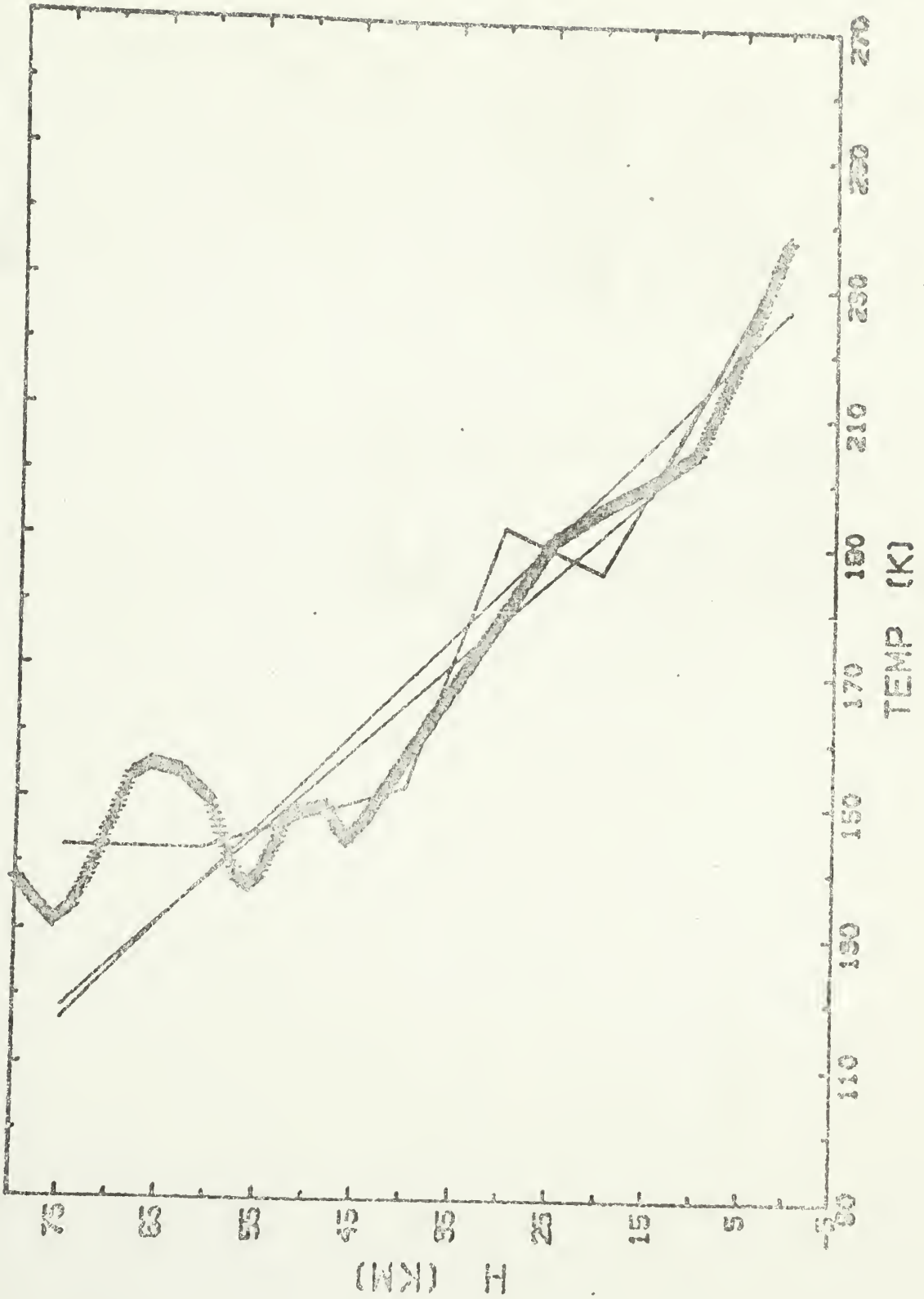
Fit to CO(J=1-0)



Fit to Both



Fit to CO(J=2-1)



giving rise to this exaggerated structure. Undoubtedly, a parametrization that created a smoother curve for the model (e.g. a spline) would do a better job of retrieving the true profile.

The ability of the simplest model to fit the line profiles is due to several factors. Foremost is the fact that no surface temperature difference was included in the model. It was partly to fit what turned out to be a temperature difference of some sort that prompted much of the additional structure postulated for the atmospheric temperature profile. It is important to note, however, that this additional structure can be justified on the basis of the simulation as necessary to ensure an accurate determination of the CO abundance.

It is encouraging that none of the uncertainty in the derived atmospheric temperatures appears to affect the accuracy with which the CO mixing ratio can be determined; even the two lapse rate model does a remarkably good job of retrieving this parameter. Even more remarkable is the extreme degree to which the CO abundance and the form of the temperature profile are correlated. Nowhere do the constant lapse rate profile and the two lapse rate profile differ by more than 9K, and yet the CO abundances differ by 50%. This reinforces the conclusion about this relationship that was reached in the previous chapter: the derived CO abundance is too strong a function of the temperature profile for this function to be merely assumed - it must be derived from the data.

Finally, the assumption of a constant mixing ratio profile should be reexamined since it remains possible that some of the structure

attributed to temperature differences could actually come from variations in this parameter. Tests were made using a model in which the mixing ratio above a given height either doubled or dropped to zero. This model was chosen for its simplicity and for its extreme nature; it was felt that effects unobservable under these conditions would not appear for smaller variations in the abundance profile. The effects on the lineshapes proved remarkably insensitive to even fairly substantial structure. In general, the lines produced looked quite similar to those that would be obtained using a uniform CO abundance whose value was the mean of this model over the region of the atmosphere the observations are sensitive. This comes about both because the emission is a weaker function of the CO abundance than it is of the temperature and because the weighting function for any given frequency channel averages over enough of the atmosphere to smooth out the fluctuations. Also, the weighting functions for any given channel in the two lines overlap enough to prevent the difference in the two lines being caused by abundance variations.

C H A P T E R V I
SUMMARY AND CONCLUSIONS

In their original analysis of the CO(J=1-0) spectrum, Good and Schloerb (1981) felt that they did not have enough information to choose between different temperature models and therefore chose to use the simplest one; a constant lapse rate. This leads to a deduced CO mixing ratio four times greater than the current analysis shows. Since the only independent CO abundance at that time (Kaplan et al., 1969, Young, 1971 from IR lines in the Connes spectral atlas) was also a quarter of that value, it appeared that a substantial increase in the CO abundance had occurred during the intervening years. Given the possible time variability noted by Hunten (1974), this seemed to be a reasonable possibility.

Besides determining the CO abundance, the current analysis has also found the reason for the discrepancies in the fits to the CO lines by different investigators. The CO abundance deduced is strongly dependent on the form chosen for the temperature structure, far more than had been supposed. Therefore, although the CO abundance has been determined for the time of the 1982 measurement, no definite conclusion can be reached regarding the abundance at the time of the 1980 CO(J=1-0) measurement; the possible combinations of mixing ratio and temperature profile are too numerous to make this possible. On the

other hand, the similarity between the 1980 CO(J=1-0) spectrum and the 1982 line strongly suggests that conditions were comparable at the two times. If this is so, it is entirely possible that the CO mixing ratio measured at three different times in the past fourteen years has been within 25% of a value of about 10^{-3} .

If the CO abundance is in fact stable, then there are two important consequences. First, it means that a single CO line might be better used as a probe of the martian atmospheric temperature profile than as a probe of the CO abundance. Second, it suggests that any long term variations in the CO abundance, due to the mechanisms proposed by Hunten (1974), are small.

In addition to the above evaluation of the CO abundance, two major related conclusions have been drawn from this analysis. First, the mixing ratio deduced is strongly dependent on the details (and even the parametric form) of the temperature structure; although a single line may be fitted well with an assumed temperature profile and a deduced CO mixing ratio, that mixing ratio may be totally inaccurate if even fairly minor details of the temperature structure are incorrect. Second, a single CO line, because it can be fit by using even the simplest of temperature models, does not contain enough information to constrain both the CO abundance and the temperature profile.

Finally, we note that given high spatial resolution, moderate spectral resolution and low noise, this technique would allow detailed

probing of both the CO abundance profile and the temperature profile in the lower and middle atmosphere of Mars - possibly with the accuracy obtainable by an entry probe. This would allow local modeling of the atmospheric chemistry, an important consideration given the latitudinal and seasonable variability of water.

BIBLIOGRAPHY FOR PART I

- Connes, J., Connes, P., Maillard, J.P. (1969). Atlas of Near Infrared Spectra of Venus, Mars, Jupiter, and Saturn, Centre National de la Recherche Scientifique, Paris.
- Clancy, R.T., Muhleman, D.O., Jakosky, B.M. (1983). Variability of Carbon Monoxide in the Mars Atmosphere (Icarus, in press)
- Cuzzi, J.N. and Muhleman, D.O. (1972). The Microwave Spectrum and Nature of the Surface of Mars. Icarus 17, 548-560.
- Goldsmith, P.F., and Scoville, N.Z. (1980). Baseline Ripple Reduction by Quasi-Optical Phase Modulation, Astron. Astrophys. 82, 337.
- Good, J.C., and Schloerb, F.P. (1981). Martian CO Abundance from the J=1-0 Rotational Transition: Evidence for Temporal Variations. Icarus 47, 166-172.
- Hess, S.L., Henry, R.M., Leovy, C.B., Ryan, J.A., Tillman, J.E. (1977). Meteorological Results from the Surface of Mars: Viking 1 and 2. J. Geophys. Res. 82, 4559-4574.
- Hunten, D.M. (1974). Aeronomy of the Lower Atmosphere of Mars. Rev. Geophys. Space Sci. 12, 529-535.

- Kakar, R.K. , Waters, J.W. , Wilson, W.J. (1977). Mars: Microwave Detection of Carbon Monoxide. Science 196, 1090-1091.
- Kaplan, L.D. , Connes, J. , Connes, P. (1969). Carbon Monoxide in the Martian Atmosphere. Ap.J. 157, L187-L195.
- McElroy, M.B. and Donahue, T.M. (1972). Stability of the Martian Atmosphere. Science 177, 986-988.
- Muhleman, D.O. (1972). Microwave Emission from the Moon. In Thermal Characteristics of the Moon (J.W. Lucas, ed.), Progress in Astronautics and Aeronautics, 28, 51-81. MIT Press Cambridge, Massachusetts.
- Parkinson, T.D. and Huntten, D.M. (1972). Spectroscopy and Aeronomy of O₂ on Mars. J. Atmos. Sci. 29. 1380-1390.
- Schloerb, F.P. , Robinson, S.E. and Irvine, W.M. (1980). Observations of CO in the Stratosphere of Venus via Its J=1→0 Rotational Transition. Icarus 43, 121-127.
- Seiff, A. and Kirk, D.B. (1977). Structure of the Atmosphere of Mars in Summer at Mid-Latitudes. J. Geophys. Res. 82, 4364-4378.
- Wilson, W.J. , Klein, M.J. , Kakar, R.K. , Gulkis, S. , Olsen, E.T. and Ho, P.T.P (1981). Venus. I. Carbon Monoxide Distribution and Molecular Line Searches. Icarus 45, 624-637.

Young, L.D.G. (1971). Interpretation of High Resolution Spectra of Mars

III. Calculations of CO Abundance and Rotational Temperature.

J. Quant. Spec. Rad. Trans. 11, 385-390.

P A R T I I

VENUS SO₂ ABUNDANCE

Portions of the following work have been published under the title

"Limits on Venus' SO₂ Abundance Profile
from Interferometric Observations at 3.4 mm Wavelength"

J.C. Good and F.P. Schloerb
Icarus 53, 538-547 (1983)

CHAPTER I

INTRODUCTION

Since the discovery that the clouds of Venus are primarily composed of sulphuric acid droplets (Young, 1973), it has been apparent that we must understand the chemistry of sulfur in the atmosphere in order to explain the origin of the clouds. A major sulfur bearing compound that has been observed in the lower atmosphere (Hoffman et al., 1980, Oyama et al., 1980), and at the cloud tops (Esposito et al., 1980), and is likely to be involved in the cloud forming process is SO_2 . Current models of the chemistry of the clouds (Winick and Stewart, 1980), which concentrate on the upper clouds, involve photodissociation of SO_2 and other species from the lower atmosphere for the formation of sulphuric acid droplets. The transport of SO_2 to the cloud forming region is an integral part of this process and, therefore, its abundance profile provides important constraints on models of the clouds of Venus.

The clouds of Venus are stratified into three layers (Knollenberg and Hunten; 1980). The upper clouds occur between 56.5 and 70 km from the surface (390 to 34 mbars pressure and 286 to 225 K) and have a bimodal particle size distribution; 0.4 micron diameter "haze" particles and 2.0 micron diameter "cloud" particles. Both modes are composed essentially of H_2SO_4 with variable amounts of H_2O

depending on the temperature and pressure. It is at the top of these upper clouds that the models predict the photochemical conversion of SO_2 to H_2SO_4 to occur (Winick and Stewart, 1980). The middle cloud layer between 50.5 and 56.6 km (940 to 390 mbars pressure and 345 to 286 K) has a trimodal size distribution with particle diameters of 0.3, 2.5 and 7.0 microns. The smaller two particle types are similar to the two modes in the upper cloud layer (Knollenberg and Hunten, 1980). In addition to these liquid droplets, however, there are the larger particles of unknown composition which appear, on the basis of the atmospheric refractive index (Knollenberg and Hunten, 1980), to be a crystalline solid. The lowest cloud layer (47.5 to 50.5 km, 1370 to 940 mbars, 367 to 345 K) has a similar trimodal size distribution with sizes of 0.4, 2.0, and 8.0 microns.

The haze extends both above and below the clouds, from 31 to 90 km. At the top of the upper clouds the larger liquid particles become dominant in terms of mass, outweighing the haze by a factor of from 3 to 10. Between the middle and upper clouds the haze decreases considerably and the crystalline particles appear and become dominant in terms of mass and visual extinction. Between the middle and lower clouds the number of the larger liquid particles increases somewhat and the number of crystalline particles jumps considerably (Knollenberg and Hunten, 1980).

In all, Pioneer Venus made five measurements of the SO_2 abundance in Venus' atmosphere. The Orbiter UV Spectrometer (OUVS) measurements

(Esposito et al., 1979) imply a mixing ratio of 0.10-0.15 ppm at 69 km (the top of the upper cloud layer). An upper limit of 10 ppm was set by the Large Probe Mass Spectrometer (LNMS) at 52 km (Hoffman et al., 1980), in the middle cloud layer. No measurements of any kind were made in the lower cloud layer which has its base at about 47.5 km. The Large Probe Gas Chromatograph (LGC) made two measurements below the clouds (Oyama et al., 1980) of 176 (+296/-0) ppm at 42 km and 185 - 43 ppm at 22 km. A consistent upper limit of 300 ppm at 22 km was set by the LNMS. These measurements are summarized by von Zahn et al. (1983). Modeling of the cloud chemistry (Winick and Stewart, 1980) predicts an SO₂ abundance of about 4 ppm near the bottom of the upper clouds (58 km). Thus, these points suggest that the large SO₂ abundance is constant in the lower atmosphere and drops to a few ppm or less somewhere between 40 and 60 km. It is our goal to place meaningful constraints on the SO₂ distribution in this important region.

The region of the clouds that we wish to study does not lend itself readily to observation. All ultraviolet, visible, and infrared radiation is blocked by the upper clouds or even by the haze above them. At best, we can hope to obtain information about the upper unit optical depth or so of the highest clouds at these wavelengths and as the cloud total optical thickness is at least 6 (Knollenberg and Hunten, 1980), we are limited to the upper 3 or 4 km. At radio wavelengths (longward of 1 cm) we begin to see through the atmosphere to the surface. Although the region of the atmosphere which contains the

clouds has some effect on measurements at cm wavelengths, such measurements are most sensitive to the lower atmosphere. At millimeter wavelengths the only known source of opacity is CO_2 and, as we shall show, at 80-90 GHz (3 mm λ), the spectral region we observed, we are probing at the base of and just below the clouds.

At this frequency and at the temperature and pressure near the cloud base ($\sim 350\text{K}$, 1 bar) SO_2 behaves essentially as a continuum absorber, similar to CO_2 , due to the blending of many broad lines. At lower pressures (~ 1 mbar) individual lines would be observable. The SO_2 absorption coefficient at 3 mm λ is equal to that of CO_2 at 50 km if its abundance is ~ 100 ppm, and because the abundance measured by Pioneer Venus in the lower atmosphere is ~ 200 ppm, there would be a noticeable effect on the mm λ emission if this abundance were to persist into the lower clouds. Thus, small amounts of SO_2 in the clouds should be detectable via their effect on the planet's brightness temperature and limb darkening at 3 mm λ .

The beams of most single millimeter-wave antennas are much larger than Venus' diameter, and therefore, a single antenna measurement can only give an average disk brightness temperature. An accurately calibrated disk temperature can potentially say a great deal about the amount of SO_2 absorption in the atmosphere, but unfortunately, at mm wavelengths, absolute measurements of this type are seldom accurate enough for our purposes. Instead we have used an interferometer to

spatially resolve the planet and determine the amount of limb darkening. Since limb darkening is a relative measurement, it offers the potential for greater accuracy and a more sensitive experiment. As we shall see, the constraints placed on the SO₂ abundance profile by our measurement of the limb darkening could only be matched by a brightness temperature determination accurate to better than 1%, a factor of 4 better than any determination to date (Ulich et al., 1980).

The response of a two element interferometer as a function of the spacing between the two telescopes is equal to the Fourier transform of the brightness distribution of the source (Appendix A). Thus, the measurement of this response, called the visibility function, is equivalent to a measurement of the limb darkening curve. The visibility function, V , for a uniformly bright disk is given by

$$V(\beta) = S_V \frac{J_1(2\pi\beta)}{(\pi\beta)} \quad (1)$$

where β is a dimensionless spacing of the interferometer projected on the plane of the sky, S_V is the total flux density, and J_1 is the first Bessel function. The spacing parameter, β , is defined as:

$\beta = (x/\lambda) \times (R/D)$, where λ is the wavelength, x is the physical spacing of the interferometer elements, R is the radius of Venus, and D is its distance. Since λ , R , and D are either fixed or can be adjusted to some reference value, the parameter β is essentially a normalized spacing for the interferometer elements. The visibility function for a uniform disk resembles a damped oscillation which first crosses zero at $\beta =$

0.609836. The main effect of limb darkening on this response is to broaden the first lobe of the visibility function and thereby move the point where it crosses zero, β_0 , farther out. The exact position of this zero crossing, then, is diagnostic of the amount of the limb darkening.

We have chosen to characterize the amount of limb darkening by measuring the zero crossing for several reasons. First, as will be demonstrated, it is quite sensitive to the amount of limb darkening and therefore to the amount of SO₂. Second, it is independent of any amplitude calibration, being essentially a measurement of the projected spacing of the interferometer when the null in the visibility function occurs. Finally, because it is a measurement of a null point, it is insensitive to gain variations and requires less phase stability than most other applications of interferometers.

C H A P T E R I I
M E A S U R E M E N T O F T H E Z E R O C R O S S I N G

Observations

Our measurements of the Venus zero crossing were made on 17-20 December 1980 at 3.4 mm wavelength (87.24 GHz) with the Hat Creek Radio Astronomy Observatory interferometer (operated by the University of California, Berkeley). The interferometer consisted of two moveable 6m dishes which were placed on an East-West baseline roughly 85m apart. The HPBW of the individual elements was about 2.5 arcmin. The receivers were cooled Shottky diode mixers and the double sideband system temperature (including ground pickup) was approximately 150K. The observation dates were chosen so that Venus would be much smaller than the primary antenna beams since partial resolution of Venus by the beam would have mimicked limb darkening of the planet and significantly affected the zero crossing. The extent to which this would occur has been estimated, assuming a planet of uniform brightness and a gaussian beam. During our observations Venus had a semidiameter of 5.8 arcsec, and a small but noticeable correction ($\Delta\beta = -0.00022$) must be made to our measured value of the zero crossing.

Baseline Determination

Because the parameter we wish to measure is a projected spacing of the interferometer it is crucial that we know precisely the physical spacing of the interferometer elements. To determine this spacing, the baseline, we observed radio point sources of known position on each of the four days mentioned above plus the previous one, 16 December 1980. Eleven sources (Table 1) were used in this fitting, providing uniform coverage in hour angle (and continuous coverage in time) and covering $\pm 40^\circ$ in Dec. The baselines determined from the accumulated data on each of the five days agreed to within the uncertainties (about 1 part in 10^6), which were small compared to the accuracy needed for our measurement. All of the Venus data were eventually recalibrated to the baseline that was finally determined. The errors remaining in the baseline measurement have a negligible effect on our determination of the zero crossing.

The baseline calibrator phases alone for all of the four days together are shown in figure 1. By sketching a curve to approximate the variations evident in the plot we can determine to which range of 2π a given measurement belongs. By doing no more than adding or subtracting increments of 2π , the points are shifted to the correct range. A spline curve fit to the data is also shown. As can be seen, the phase of the system showed an overall drift with time; a linear drift contributing a change of 2π in ~ 36 hrs and diurnal variations

Table 1.

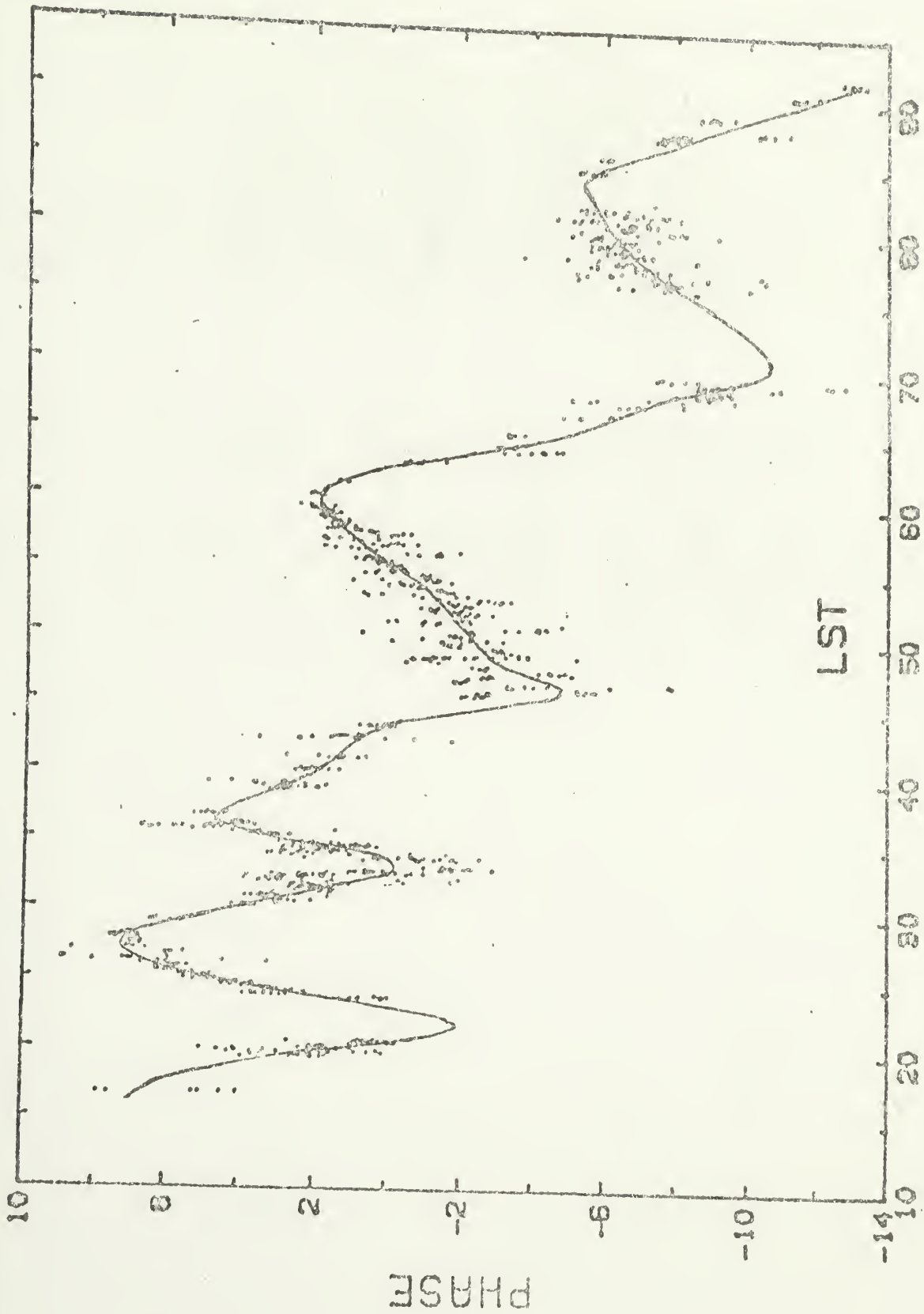
Baseline sources

NRAO 530	6.2 f.u.
OV 236	10.3
BL Lac*	4.9
3C 345*	10.4
3C 273*	25.5
3C 279*	5.8
3C 454*	6.6
3C 84*	52.9
OJ 287*	3.5
NRAO 150*	4.3
3C 120*	3.0

* Also used for amplitude and phase calibration.

The fluxes listed above represent a determination from internal ratioing of our amplitude data.

Figure 1. Phase variations of the reference calibrators, showing the stability of the short term stability and long term drifts in the system.



with amplitude $\sim\pi$. We can be sure that these variations are not related in any way to the choice of baseline as the baseline sources during any given time period were spread out over a large part of the sky and the drift observed was not correlated with position at all. There is a strong correlation between the periods of most rapid change and rapid changes in temperature, sunrise occurring at about 13^h 20^m LST. However, all of the variations mentioned above occur on a time scale that is long compared to the π change in phase at the Venus zero crossing and the variations on shorter timescales appear to be purely random in nature.

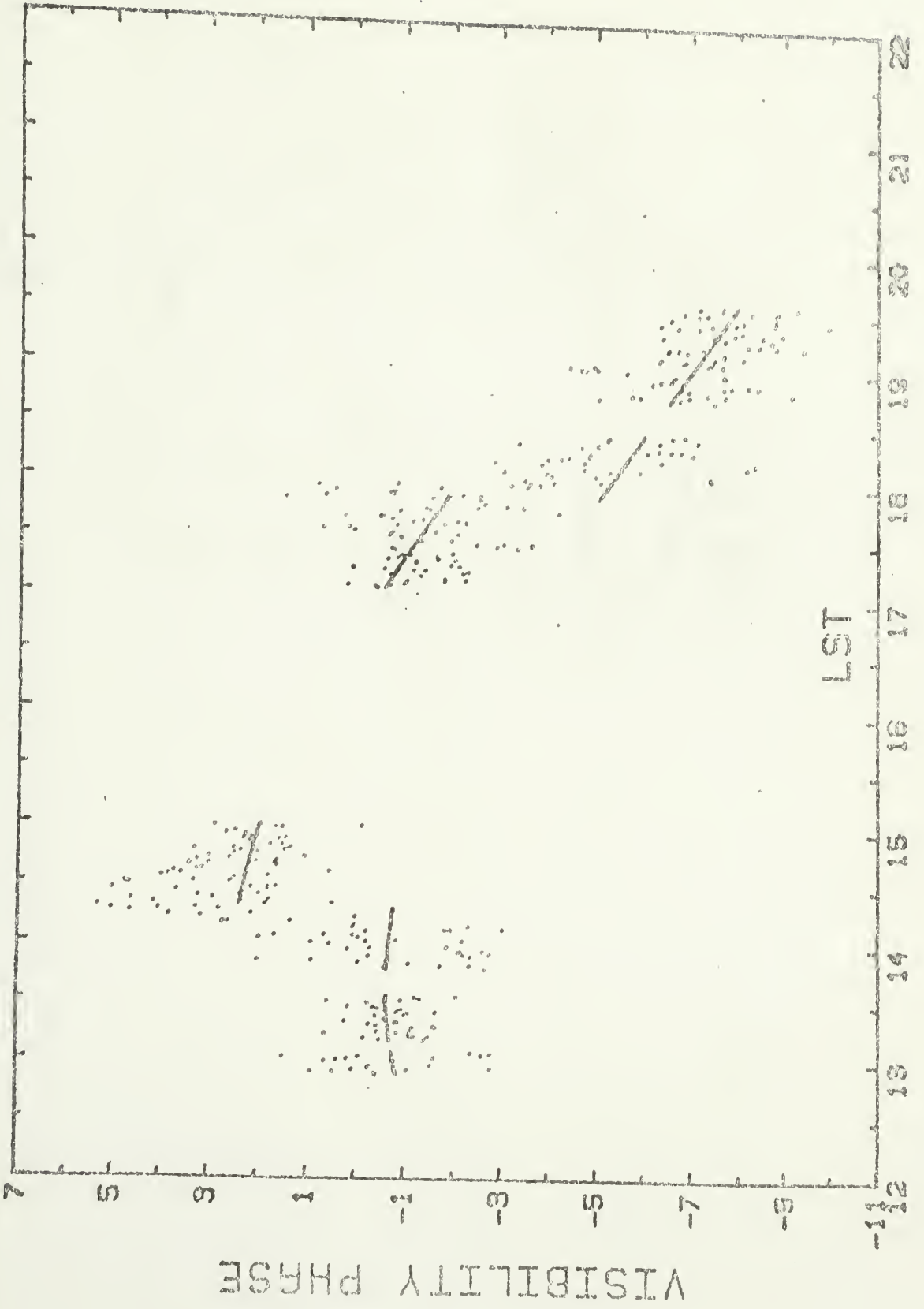
Phase Calibration

Both the amplitude and the phase of the Venus measurements required calibration, and six of the baseline sources were also used for this purpose. Data from these sources were taken interspersed with Venus data so that any temporal or altitude dependent variations could be removed. Comparison of the calibrator data with the raw Venus data makes apparent the necessary corrections to the Venus data. However, the phase drift determined from the mean of the calibrators is not identical to that of Venus, and there are also several instances where the calibrator phase drift is somewhat different from source to source. Since the π shift in phase at the zero crossing occurs on a much shorter timescale than any of these relative drifts we can calibrate those long term drifts out of our measurement. In order to improve the

calibration of the Venus phase we assumed that Venus is azimuthally symmetric and therefore that Venus' phase was flat except in the region very close to the zero crossing. Thus, the removal of the phase drift from the Venus data can be aided by utilizing those parts of the Venus data itself that were well away from the zero crossing. Any pronounced asymmetry in the planet would be apparent as a systematic variation of the Venus phase data with respect to the calibrators. Although small variations do exist, they are not larger than the typical differences between adjacent observations of the calibrators.

In the same way as for the calibrator phase and using the calibrator data as a guide, we can approximate the phase behavior of the Venus data and the period during which the visibility function is negative (out of phase by π) becomes apparent. This approximation can be used to correct the Venus phase data for the 2π ambiguity as was done for the calibrator data. The corrected points for one day are shown in Figure 2. Also shown in this figure is a polynomial fit to those points well away from the zero crossing (the fit, however, is shown for all the points). The difference of each point from the curve is the absolute calibrated phase for that point. Although we have corrected for the ubiquitous 2π ambiguity, in the vicinity of the zero crossing we have a π ambiguity since we have no a priori way of knowing whether a point has or has not made the change. As a function of β it appears that the π phase change is not sudden but rather more gradual, indicative of an asymmetry in the planet or of a pointing error. However, as

Figure 2. Sample Venus phase data with fitted polynomial showing the abrupt π phase shift at the zero crossing.



a function of time we find that this effect is due to the measurements made while Venus was setting and that it did not occur when the planet was rising. Thus, this effect is essentially an indication of the accuracy with which we can calibrate out the phase drifts in the system.

The phase information alone does not provide accurate enough information to allow us to determine the zero crossing or even to search for asymmetry on the planet. We have therefore used this information primarily to determine the sign of the visibility function, to be used in conjunction with the amplitude data. In practice, those points for which the absolute calibrated phase was greater than $\pi/2$ were judged to be negative. Here we are implicitly assuming that the planet is symmetric and therefore that the visibility is real.

Amplitude Calibration

The basic calibration of the data was done via the "chopper wheel" method (Penzias and Burrus, 1973) where observations of an ambient temperature load and the sky are used to deduce the system temperature. In addition, several sources near Venus in the sky were used to check the amplitude calibration. The absolute calibration of these sources (table 1) was achieved by comparison to 3C273. The flux density of 3C273 itself was found to be 25.5 ± 1.0 Janskys by comparison to Jupiter and Saturn using a single antenna where Jupiter was assumed to have a brightness temperature of 179 K and Saturn a brightness temp-

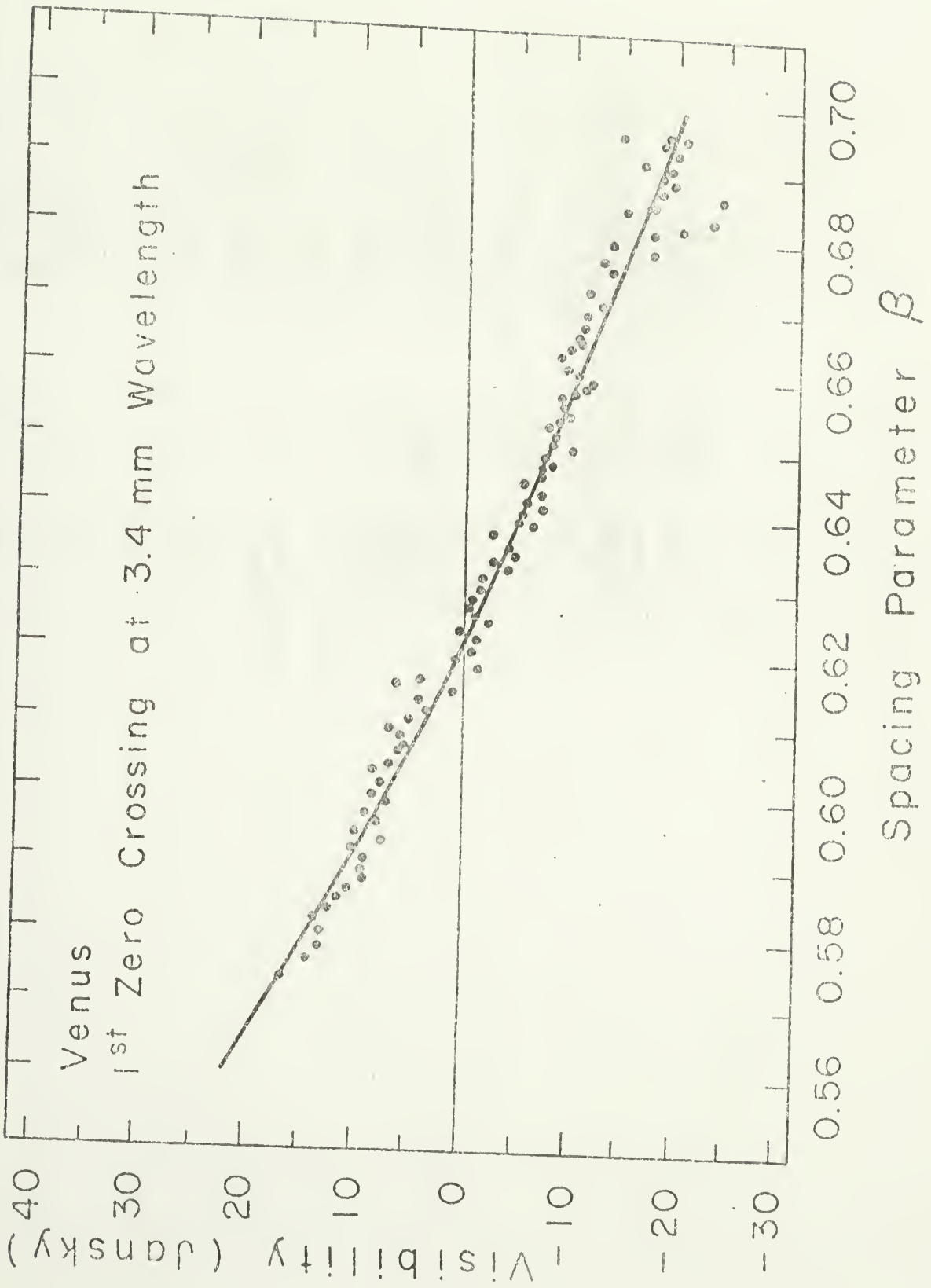
erature of 153 K (Ulich et al., 1980). Since the rms of the 3C273 measurements is about 10% of its brightness we cannot do an extremely accurate absolute calibration. It does, however, allow us to check the amplitudes of the Venus observations to this level and assure that relative amplitudes are correct.

The Venus data were taken over the range 2 to 5 airmasses, although only the points between 2 and roughly 3 airmasses were finally used to determine the zero crossing because systematic effects as well as a general scatter in the points appear for observations made through more than about 3 airmasses. As was discussed in the last section, the phase information can be used to supply the sign information, those points being negative whose phase has gone through the π discontinuity. In practice we have used as the criterion that the absolute calibrated phase be greater than $\pi/2$. The amplitude as a function of β is shown in Figure 3 with each point corrected for sign by using the phase information. Also shown is the polynomial fit for the zero crossing.

Fit for Zero Crossing

To find the zero crossing itself we have used a second order polynomial least squares fit, not for the polynomial coefficients but for the value of the zero crossing itself (Appendix B). The covariance matrix for this problem can be derived exactly, and therefore the uncertainty of the zero crossing measurement can also be found exactly. From this fit the zero crossing is found to be $\beta_0 = 0.6223 \pm 0.0007$

Figure 3. Venus amplitude data (10 point average) with polynomial fit for the zero crossing. The amplitude calibration is only approximate.



again, using a reference radius $R_{\text{venus}} = 6100$ km. When corrected for the partial resolution of the planet by the primary antenna beams the value becomes

$$\beta_0 = 0.6221 \pm 0.0007$$

The correction for beamsize does not introduce any perceptable additional error in this measurement.

C H A P T E R I I I
I N T E R P R E T A T I O N O F T H E Z E R O C R O S S I N G

I n t r o d u c t i o n

In order to understand the effects of the SO₂ abundance profile on the visibility function zero crossing, it helps to analyze in more depth the limb darkening curve in terms of the atmospheric parameters. In particular, we can derive the limb darkening law for an atmosphere composed of an adiabatic ideal gas where the absorption coefficient varies as a power law in pressure and temperature. Though this does not accurately reflect the specific situation on Venus, it does allow us to determine qualitatively the effects of changes in the important atmospheric parameters and the correlations between those parameters.

If we define our coordinate system with the distance increasing inward (downward toward the surface of the planet), the condition of hydrostatic equilibrium is given by

$$dP = \rho g dh \tag{2}$$

where P is of course the pressure, g the acceleration due to gravity, ρ is the density, and h the distance parameter. Since we are postulating an adiabatic ideal gas, the pressure is given by

$$p = \frac{\rho kT}{\mu m^m H} \tag{3}$$

and

$$\left(\frac{P}{P_0}\right) = \left(\frac{\rho}{\rho_0}\right)^\gamma = \left(\frac{T}{T_0}\right)^{\gamma/(\gamma-1)} \quad (4)$$

where T is the temperature, k is the Boltzman constant, m_H is the mass of a hydrogen atom, and μ_m is the mean molecular weight of the atmosphere.

We will use the Rayleigh-Jeans approximation for the Planck function,

$$B_\nu = \frac{2kT}{\lambda^2} \quad (5)$$

and assume that the absorption coefficient is of the form

$$\alpha = a \left(\frac{P}{P_0}\right)^n \left(\frac{T_0}{T}\right)^m \quad (6)$$

This form is valid for many continuum absorbers, and in particular for CO_2 (Ho et al., 1966) and, at high pressures, for SO_2 (Jannsen and Poynter, 1981).

We can show (Appendix C) that in this case the limb darkening curve is given by

$$\frac{I(\mu)}{I(0)} = \mu^{\left(\frac{\gamma-1}{\gamma n - m(\gamma-1) - 1 + \gamma}\right)} \quad (7)$$

where μ is the cosine of the viewing angle ($\cos(\theta)$). When we view the planet, the angular distance outward from the center of the planet as a fraction of the radius of the planet gives us the viewing angle θ

$$\sin(\theta) = \frac{r}{R} \quad (8)$$

Therefore,

$$I(r) = I_0 \left(1 - \frac{r^2}{R^2}\right)^{1/2 \left(\frac{\gamma - 1}{\gamma n - m(\gamma - 1) - 1 + \gamma}\right)} \quad (9)$$

It is important to note here that it is impossible to determine both γ and the parameters defining the absorption coefficient, n and m . Since, as we shall see below, γ is a measure of the lapse rate in the atmosphere, this means that it is impossible to determine both the temperature structure and the absorption coefficient profile in the atmosphere from a measurement of the limb darkening curve. It is only in cases where one of the two is known with some precision that the other can be determined uniquely.

In the specific case of Venus, the absorption by CO_2 is of the form (Ho et al., 1966)

$$\alpha = a \left(\frac{P}{P_0}\right)^2 \left(\frac{T_0}{T}\right)^5 \quad (10)$$

so

$$n = 2$$

and

$$m = 5$$

In general, the lapse rate in the atmosphere is given by

$$\frac{dT}{dh} = \frac{(\gamma-1)}{\gamma} \frac{\mu_m m H g}{k} \quad (11)$$

This is easily derived from hydrostatic equilibrium and the adiabatic relationships listed above. On Venus,

$$\frac{dT}{dh} = 8.3 \times 10^{-5} \text{ K/cm}$$

$$g = 860 \text{ cm/s} \quad (\text{assumed constant with height})$$

and
$$\mu_m = 43.2 \quad (95\% \text{ CO}_2 + 5\% \text{ N}_2)$$

(Muhleman et al., 1980, Hoffman et al., 1980)

Thus,

$$\frac{\gamma-1}{\gamma} = 0.19$$

and

$$\gamma = 1.23$$

This means that the limb darkening curve should be approximately

$$I = I_0 \left(1 - \frac{r^2}{R^2}\right)^{(0.0743)} \quad (12)$$

This function is indeed quite similar to the curves produced by the numerical model to be discussed later. Fourier transforming it, we obtain a zero crossing of 0.6225 which is within 1σ of our measurement.

This remarkably close result is somewhat fortuitous as the limb darkening is actually quite sensitive to the parameters we approximated above and to the effects of planetary curvature and atmospheric refraction. However, it does give us faith in our analysis of the importance of specific variables and it further suggests that the zero crossing that we have measured may be consistent with a pure CO₂ atmosphere.

It is illuminating to consider the effects of changing the various atmospheric parameters on this curve. First, we note that the only parameters that will affect the shape of the limb darkening curve are γ , n and m . Anything that changes the scale of the curve by changing I_0 is not of direct interest because the visibility function zero crossing is unaffected by vertical scalings. The parameters n and m are, as we said, 2 and 5 for CO₂. If the atmosphere were dominated by absorption by SO₂ these parameters would be 1.22 and 3.1. This would imply a limb darkening curve given by

$$\frac{I}{I_0} = \left(1 - \frac{r^2}{R^2}\right)^{(0.113)} \quad (13)$$

which has a sharper limb and is therefore more limb bright than the curve for the pure CO₂ atmosphere. When transformed, this gives a zero crossing which is more than 7σ less than the observed value. The same difference in the exponent could be obtained in a pure CO₂ atmosphere by decreasing the lapse rate by about 20% and indeed, the lapse rate in the upper part of the clouds is closer to this value, so we cannot

expect to determine the exact values of any parameters from this simplified analysis. It does, however, again point up the impossibility of determining both the temperature structure and the source of opacity at the same time.

Model Limb Darkening Curves

In order to interpret our measurement of the zero crossing further we must link it to a set of limb darkening curves and thereby to a set of atmospheric models. The variable parameters in these models are the runs of temperature, pressure and SO₂ mixing ratio with height. All three must be assumed in order to calculate the emergent intensity of radiation from each point on the disk of the planet. This distribution is then transformed to give the visibility function and its zero crossing.

The solution to the radiative transfer equation for the emergent intensity from a non-scattering planetary atmosphere where azimuthal symmetry is assumed can be written (Chandrasekhar, 1960)

$$\begin{aligned}
 I_{\nu}(\mu_0) &= B_{\nu}(T_s) e^{-\tau_s} + \int_0^{z_s} k(z) B_{\nu}(T(z)) e^{-\tau(z)} \frac{dz}{\mu(z)} \\
 &= B_{\nu}(T_s) e^{-\tau_s} + \int_0^{\tau_s} B_{\nu}(T) e^{-\tau'} d\tau' \quad (14)
 \end{aligned}$$

where

$$\tau(z) = \int_0^z k(z) \frac{dz}{\mu(z)}, \quad (15)$$

$$\tau_s = \tau(z_s),$$

z_s is the depth of the surface, $B_\nu(T)$ is the Planck function, and $k(z)$ is the absorption coefficient. The coordinate system is positive inward and μ_0 is the value of μ at $z = 0$ (the top of the atmosphere). This equation can be integrated numerically as

$$I_\nu(\mu_0) = B_\nu(T_s) e^{-\tau_s} + \sum B_\nu(T(z_i)) e^{-\tau(z_i)} (1 - e^{-\Delta\tau_i}) \quad (16)$$

The absorption coefficient at a given height is a combination of contributions from CO_2 and many lines of SO_2 . Each SO_2 line has a Van Vleck-Weiskopf lineshape and the absorption due to a specific line is a function of the absorption coefficient at line center (γ_0) and the linewidth. This absorption is given by

$$\gamma = \gamma_0 (\nu/\nu_0)^2 \left[\frac{\Delta\nu^2}{(\nu-\nu_0)^2 + \Delta\nu^2} + \frac{\Delta\nu^2}{(\nu+\nu_0)^2 + \Delta\nu^2} \right] \quad (16)$$

The peak absorption, γ_0 , for an asymmetric rotor such as SO_2 is given by (Townes and Schawlow, 1955)

$$\gamma_0 = \frac{8\pi^2\nu_0 f_\nu}{3ckT} \frac{(2J+1) |\mu_{ij}|^2}{Q_r} \frac{N_{\text{SO}_2}}{\Delta\nu} e^{-W_i/kT} \quad (17)$$

where N_{SO_2} = the number density of SO_2 (cm^{-3})

$|\mu_{ij}|$ = dipole matrix element for the transition

W_i = energy of the lower state

f_v = fraction of molecules in the ground vibrational state
 ($f_v = 0.917$ at 293 K and is slowly varying, so assumed constant)

Q_r = rotational partition function.

Also,

$$(2J+1) |\mu_{ij}|^2 = S_{ij} \mu^2 \quad (18)$$

where S_{ij} = line strength

and μ = dipole moment of $\text{SO}_2 = 1.634 \times 10^{-18}$ esu

The rotational partition function, Q_r , can be obtained from measured molecular parameters and the temperature:

$$Q_r = \frac{1}{\sigma} \left[\frac{\pi}{ABC} \left(\frac{kT}{h} \right)^3 \right]^{1/2} \quad (19)$$

where σ = symmetry number = 2

and where $A = 60776.18$ MHz

$B = 10318.10$ MHz

and $C = 8799.96$ MHz are the rotational constants.

The pressure broadened linewidth, $\Delta\nu$, at a given temperature and pressure can be scaled from that at a standard T_0 and P_0 by

$$\Delta\nu = \Delta\nu_0 \frac{P}{P_0} \left(\frac{T_0}{T} \right)^{0.75} \quad (20)$$

where

$P_0 = 1$ mbar

$T_0 = 293$ K

and $\Delta\nu_0 = 5.4$ MHz for broadening by CO_2 (Janssen and Poynter, 1980).

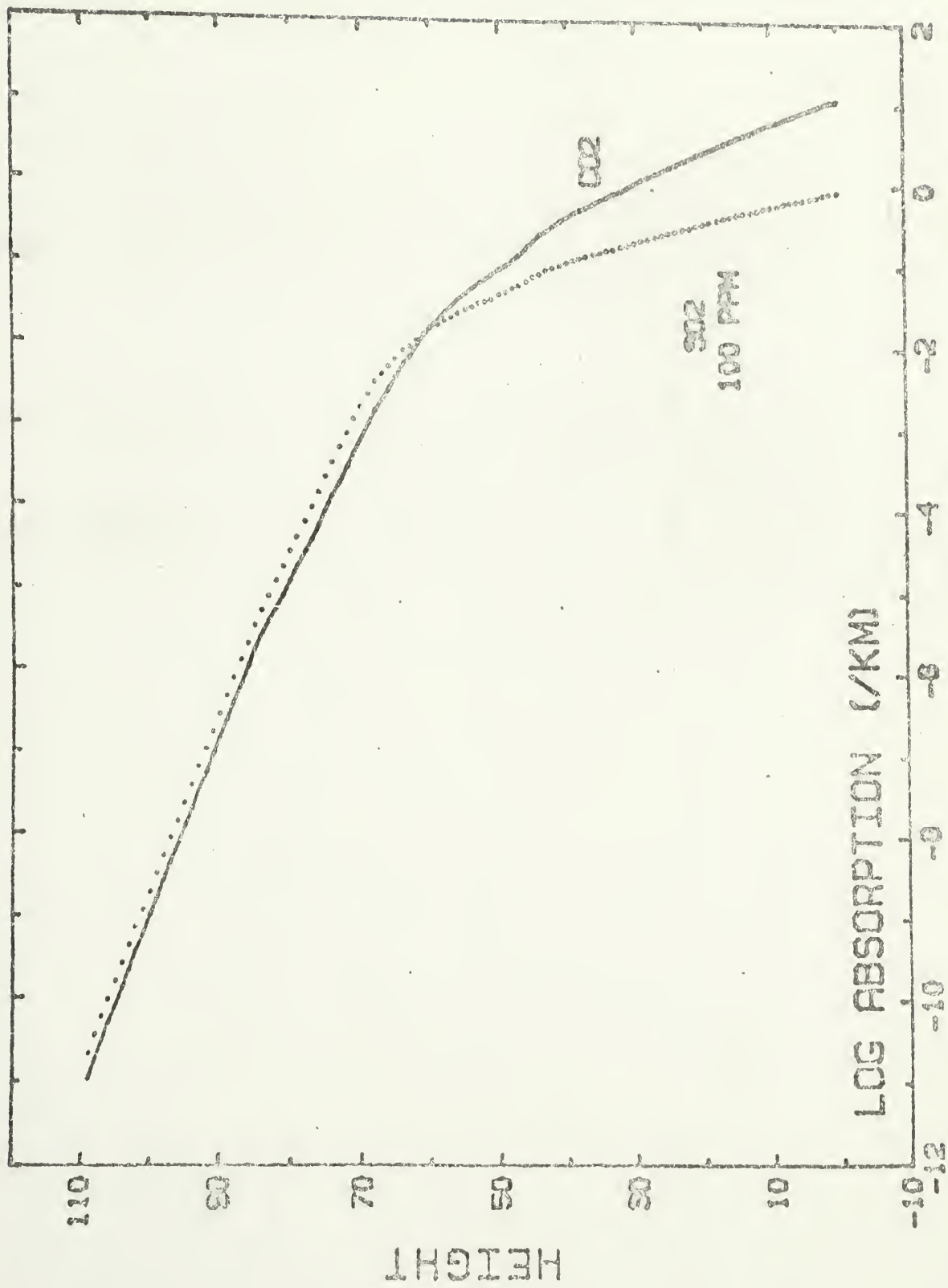
The absorption coefficients tabulated by Kolbe et al. (1976) were for SO₂ self-broadening for which $\Delta\nu_0 = 12$ MHz and must be scaled up accordingly. This parameter is not well known in any case, being based on the measurement of one line at 24.08 GHz (Krishnaji and Chandra, 1963) and could be in error by as much as 30%. At low pressures, our absorption coefficients are in good agreement with the similar calculations made by Janssen and Poynter (1980). At high enough pressures the effects of individual lines disappear and there are contributions from lines at even higher frequencies than the ones included. Thus for pressures > about 1 bar, we have adopted an analytical expression (Janssen and Poynter, 1980):

$$\gamma = 3.69 \text{ m} \sqrt{\frac{2 P^{1.22}}{T^{3.1}}} \text{ km}^{-1} \quad (21)$$

where P is in mbars and m is the mixing ratio of SO₂.

To facilitate comparisons between the CO₂ and SO₂ absorptions per kilometer we show in Figure 4 a comparison of the CO₂ absorption and that produced by SO₂ if the SO₂ were uniformly mixed at 100 ppm. In this case it can be easily seen that the effect of SO₂ would be apparent only above about 60 km, but that there it would be dominant. In fact, it would produce a strong, sharp absorption line, but we know from the Pioneer Venus measurements that the SO₂ abundance has dropped to about 0.1 ppm at 70 km, so no such line is to be expected. The value of 100 ppm was chosen for convenience and the effect of

Figure 4. Absorption coefficients for CO_2 and SO_2 (100 ppm) in the atmosphere of Venus. The height at which SO_2 becomes significant depends on its abundance.



variations from this is to scale the absorption coefficient proportionately. In the cloud forming region between 45 and 70 km the effect on the emergent intensity is quite sensitive to the amount of SO₂.

Additionally, we have investigated the effect of the uncertainty in the pressure broadened line width mentioned above. For all the lines used the linewidth was decreased by 30% and the absorption coefficients were again calculated. The effect of this scaling is considerably less than might at first have been supposed, changing the absorption coefficient by at most a few percent. As the pressure broadened linewidths are decreased, the peak absorption of each line is increased and therefore the absorption due to the nearest lines is increased. On the other hand, the contributions from more distant lines is decreased. Because the effect from these distant lines is considerable, the net effect is to leave the absorption coefficient essentially unchanged.

Finally, before we can use the radiative transfer equation to calculate the emergent intensity, we must know the refractive index at each along the path so that we can change that path accordingly as we progress. Snell's law for a spherically symmetric medium is

$$r n(r) \sin(\phi(r)) = s \quad (22)$$

where r = radius

$n(r)$ = refractive index at r

$\phi(r)$ = angle between radial direction and path of radiation
 and s = impact parameter for ray emergent from the atmosphere.

The Lorentz-Lorenz relationship gives the refractive index

$$n(r) = 1 + N_0 \rho(r)/\rho_0 \quad (23)$$

where $\rho(r)$ = density
 if ρ_0 = density at STP
 and N_0 = refractivity at STP are known.

The atmospheric composition is effectively 95% CO₂ and 5% N₂,
 therefore the refractivity

$$N_0 = 0.95 N_{\text{CO}_2} + 0.05 N_{\text{N}_2} \quad (24)$$

where $N_{\text{CO}_2} = 4.94 \times 10^{-4}$
 and $N_{\text{N}_2} = 3.00 \times 10^{-4}$ (Muhleman et al., 1980)

Calculation of the Visibility Function

In the last section, we developed the formalism needed to calculate the emergent intensity at any point on the planet's face. Having chosen a ray directed into the atmosphere, we integrate down along a path which bends relative to the local normal both because of the curvature of the planet and because of refraction. At each point along the path, the contribution to the emergent intensity is calculated, as

are the new optical depth and the new direction the path will follow. We choose the points at which our rays enter the atmosphere based on our accuracy criterion for the subsequent transformation to a visibility function.

In choosing the points across the face of the planet for the intensity calculation, we are primarily interested in obtaining a set of intensities which will, when transformed, give us an accurate visibility function and, in particular, an accurate zero crossing. Because we require fairly high accuracy in the zero crossing we must choose the points and do the transformation carefully. As is shown in appendix A, the visibility function is obtained from the brightness temperature distribution by the transform

$$V(\beta) = \frac{4\pi k}{\lambda^2 D^2} \int_0^{r_{\max}} T_b(r) J_0\left(\frac{2\pi\beta r}{r_0}\right) r \, dr \quad (25)$$

where

$$\beta = \frac{s \, r_0}{\lambda \, D} \quad (26)$$

with

- s = the projected spacing of the interferometer
- λ = the wavelength (3.4 mm)
- D = distance to Venus (2.17×10^{13} cm)
- r_0 = reference radius of Venus (6100 km).
- r = projected radius viewed by observer
(i.e. impact parameter)

This can be approximated as

$$V(\beta) = \frac{4\pi k}{\lambda^2 D^2} \sum_i T_b(r_i) J_0\left(\frac{2\pi\beta r_i}{r_0}\right) r_i w_i \quad (27)$$

where r_i = quadrature points

and w_i = weights

There is no straightforward way to test the accuracy of any given integration scheme or quadrature since there is no function with a shape similar to that of the brightness temperature distribution on Venus which has an analytical transform. Instead we have internally compared several integration techniques and chosen one which gives high accuracy with the minimum number of points. Since the function we wish to fit is not analytic in nature, we have used one of our models as a base. Of course, the calculations to get the intensities for this brightness temperature test model had to be carried out at a specific set of r_i . The points for the other quadratures were interpolated from these using a cubic spline under tension and are therefore essentially free of any sort of interpolation error. This should not matter in any case, as we are interested in the effects of various quadrature schemes on the transform. Because the correct zero crossing is unknown we have chosen to use as a reference zero crossing that obtained by transforming the intensities via 40 point gaussian quadrature. In addition to gaussian quadratures, we have transformed the distribution using trapezoidal and Simpsons's rule integrations and points numbering up to

1000. For the transforms to agree to within 1 part in 10^5 , which is accurate enough for our purposes, there must be at least 500 points in a trapezoidal or Simpson's rule integration. This number can be reduced considerably by concentrating the points near the limb of the planet where most the rapid change of brightness with radius occurs and we found that reliable accuracy could be obtained with somewhat under 200 points distributed in this manner.

Model Fitting to Zero Crossing Measurement

It has become apparent in our analysis up to this point that an atmospheric model in which CO_2 is the only absorber agrees with our measurement quite well. This being so, we realize that any modeling we do will have the effect of placing upper limits on the absorption coefficient at various levels in the atmosphere. It is noteworthy that although this analysis is concerned with the SO_2 mixing ratio profile, it also places constraints on any absorber in the cloud region.

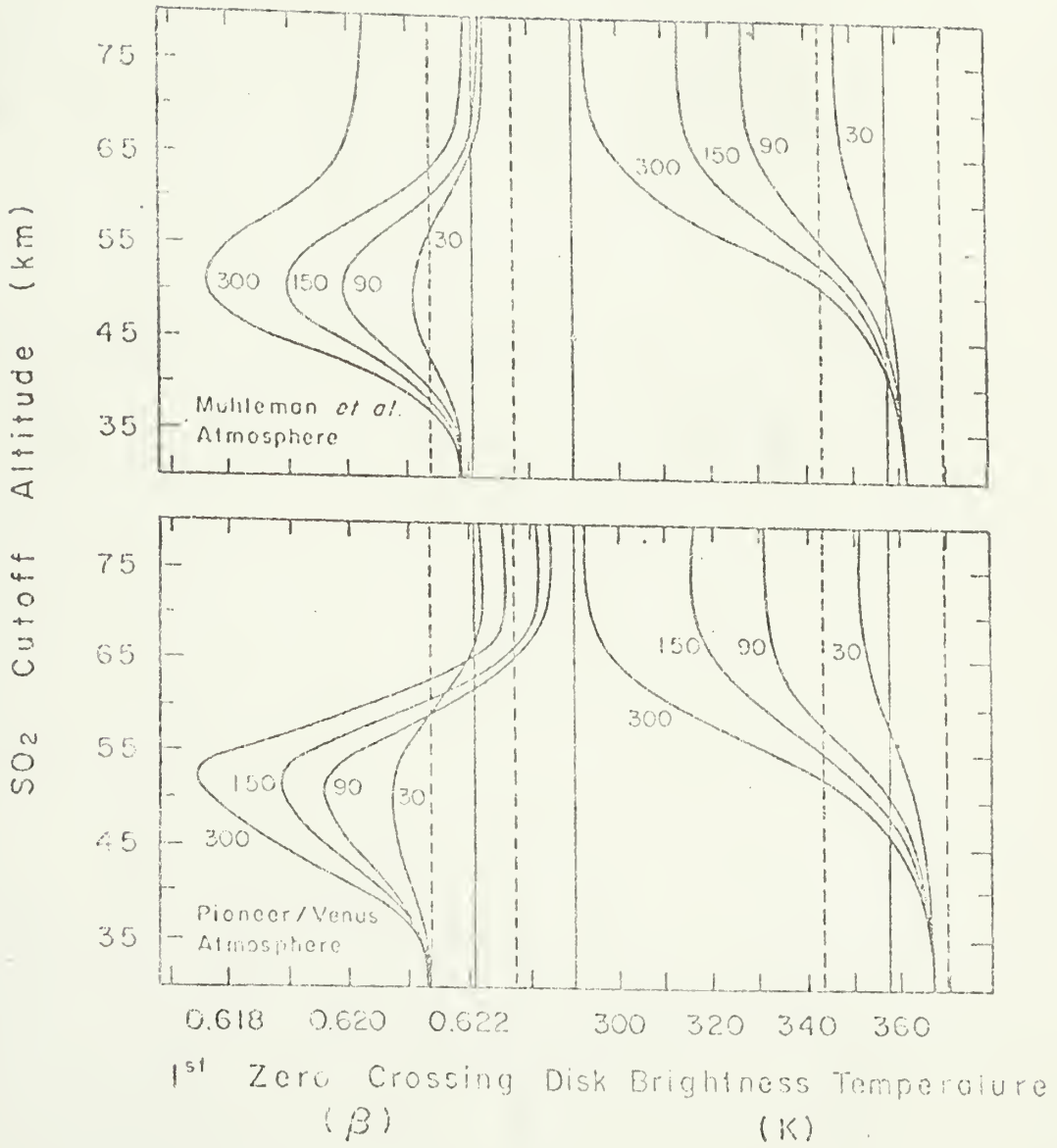
The final variable needed as input to the model calculations is the mixing ratio profile of SO_2 . We know that the general form of this profile is one in which the mixing ratio is fairly constant at a high level (~ 200 ppm) below the clouds (40 km) and then decreases in the region of the clouds to a value of about 0.1 ppm at 70 km. What we wish to determine is the range of profiles in the clouds that is consistent with our zero crossing measurement.

Since it is simplest, the first model profile we consider is that of a discontinuous decrease in the SO_2 abundance. In this model the SO_2 mixing ratio is assumed constant up to a cutoff height where it drops to 0.1 ppm, its value above the cloud tops (Esposito et al., 1980). The mixing ratio below this height is a second variable. The zero crossings and brightness temperatures determined from this modeling using the atmospheric model of Muhleman et al. (1979) are shown in Figure 5. As can be seen, for a cutoff at a given height an increase in the mixing ratio decreases the zero crossing. Increasing the height of the cutoff also decreases the zero crossing up to a point. However, high in the atmosphere this effect reverses, bringing the zero crossing back up. The brightness temperature monotonically decreases in response to the increase of either the mixing ratio of SO_2 or the cutoff level, because doing either increases the overall absorption in the atmosphere and shifts the mean of the weighting function to higher levels and therefore to lower temperatures.

Although large amounts of SO_2 over the entire region would thus be acceptable from the point of view of the zero crossing measurement, they would imply a disk temperature that is quite low. By comparing the modeled brightness temperatures with the brightness temperatures for Venus measured by Ulich et al. (1980), we can rule out those mixing ratio profiles which have large amounts of SO_2 at high altitudes. This is not surprising in light of the Pioneer Venus measurements, which limited the mixing ratio at 52 km to be less than 10 ppm (Hoffman et

Figure 5. Zero crossings and brightness temperatures predicted for SO₂ distributions in which the abundance is constant at the value shown up to a given height and essentially zero above. The curves are shown for two different model atmospheres and the measured value and uncertainty are also depicted. Only those portions of the curves falling within the uncertainty limits on the measurement (dotted lines) are consistent with the zero crossing measurement.

SO₂ Cutoff Distribution Models



al., 1980). Because the brightness temperature measurements constrain the cutoff to be in the lower cloud layers, we can use our zero crossing measurement to constrain the mixing ratio profile in this region, further constraining the brightness temperature.

To test the sensitivity of the results to the atmospheric model, we have performed the same analysis using the Pioneer Venus atmospheric measurements (Seiff et al., 1980). This work is also shown in Figure 5. For this atmospheric model, the conclusions are essentially the same, though even less SO_2 can be allowed. Therefore, our results are insensitive to the details of the atmospheric model. Finally, we have examined the sensitivity of the model to a change in the SO_2 linewidth, and found its effect on our result to be negligible. This is due to the effect mentioned before, that while a decrease in the linewidth increases the peak absorption of each of the lines, it also decreases the contribution from the wings of all the distant lines.

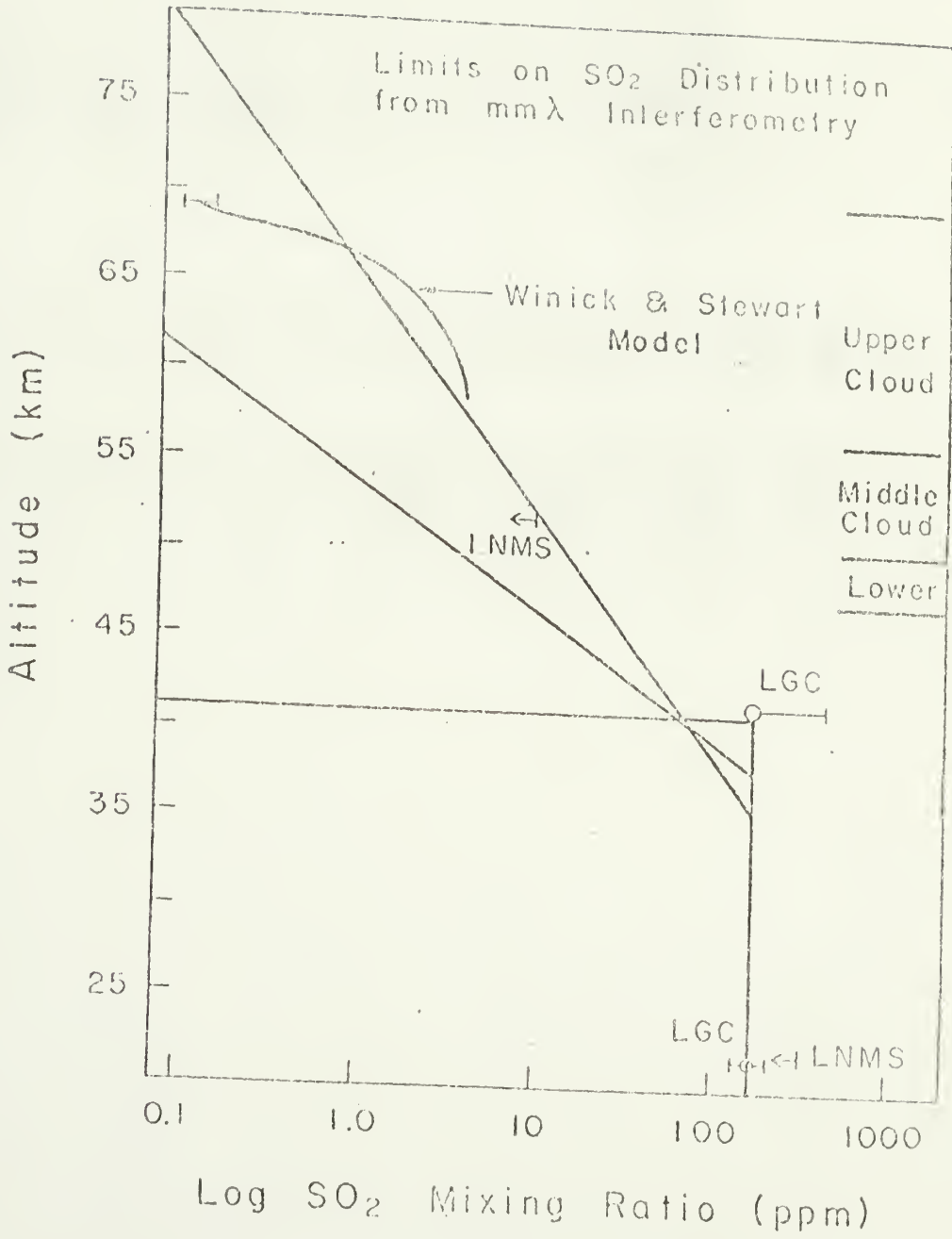
Representation of the results in terms of a model with an exponential SO_2 dropoff is more complicated, due to the presence of an extra parameter, but is more physically realistic. This is the kind of dropoff with height that one would expect in a region where the eddy diffusion coefficient is constant and a sink exists which is proportional to the SO_2 abundance. Also, this model allows for a variable amount of SO_2 in the clouds, only partly tied to the abundance below the clouds rather than the more drastic approach of the previous model. Bearing

in mind that the modeling already presented suggests that we can only place constraints on the total amount of SO_2 in the height range we are sensitive to, we present in Figure 6 those profiles which allow the maximum amount of SO_2 . For these curves, we adopted a mixing ratio of 180 ppm in the lower atmosphere (the Pioneer Venus measurement). Each of these profiles corresponds to a zero crossing exactly 2σ from our measurement. Thus, for a given cutoff point a scale height larger than the one shown would produce a zero crossing different from the measured one by more than 2σ . Plotting the profiles differing from the measurement by 1σ produces a similar set of curves but displaced downward by about 4 km. The above analysis was done using the Muhleman et. al (1980) atmosphere. Using the Pioneer Venus atmosphere (Seiff et al., 1980) would place even tighter constraints on the 2σ set of profiles, shifting them downward by 3-4 km. Thus the curves plotted represent a strong constraint on the distribution of SO_2 in the atmosphere.

Conclusions on the SO_2 Abundance Profile

The large amounts of SO_2 (~180 ppm) measured by Pioneer Venus in the lower atmosphere cannot persist above 40 km. The best fit to the data occurs if the decrease with height that this implies begins at even lower altitudes. Certainly, by the time the base of the clouds (~47 km) is reached the mixing ratio has dropped considerably. The model is not sensitive to the mixing ratio below 35 km but clearly, this result limits the range of chemical models for the region just

Figure 6. Upper limits to the SO₂ abundance profile. The Pioneer Venus observed values are shown for comparison. Any of the SO₂ profiles shown represents an upper limit. That is, if there is SO₂ at any level in addition to that shown, it give rise to a zero crossing inconsistent with our measurement.



below the clouds. Finally, if we insist that the measurement of about 185 ppm SO₂ made by Pioneer Venus at about 42 km is accurate, we are forced to have an essentially discontinuous drop in the SO₂ abundance at this point in order to fit the observed Venus visibility function zero crossing to within 2 σ .

CHAPTER IV

DISCUSSION

Sulfur Chemistry in the Clouds of Venus

Because the chemical processes effective at the base of the clouds are unknown, we cannot use our result to infer specifics about the chemical state of the atmosphere. However, by investigating the transport equation we can reach general conclusions on the relative importance of transport and chemistry in determining the SO_2 profile.

The transport of chemical species in the atmosphere is in general due to microturbulent convection or eddies and is treated as a diffusion process. The parameter defining the state of the atmosphere with regard to this transport mechanism is the eddy diffusion coefficient, κ , which appears in the diffusion equation

$$\frac{\partial m}{\partial t} = \frac{\partial}{\partial z} (\kappa(z) \frac{\partial m}{\partial z}) - S(z) m \quad (28)$$

where m is the abundance of the species (in this case SO_2) and S is a source term (in our case the destruction rate). In the steady state, as we suppose for Venus,

$$\frac{\partial}{\partial z} (\kappa(z) \frac{\partial m}{\partial z}) = S(z) m \quad (29)$$

Suppose that over a small region both S and κ are constant. Then

$$\frac{\partial^2 m}{\partial z^2} = \frac{S}{\kappa} m \quad (30)$$

and

$$m = m_0 e^{-\sqrt{S/\kappa} (z-z_0)} \quad (31)$$

is the solution, where the abundance drops monotonically with height from m_0 at a height z_0 .

It is easy to see that it is impossible to have a situation where the abundance drops with height unless there is some destruction mechanism. On the other hand, it is not possible to determine from the mixing ratio profile alone what the destruction rate is, since the mixing ratio scale height is

$$H = \sqrt{\kappa/S} \quad (32)$$

and therefore a small destruction rate can be masked by an equally small eddy diffusion coefficient.

If we assume that at the point at which the mixing ratio begins to drop the rate is given by the least precipitous of our models ($H \approx 6$ km), we have a relationship between the destruction rate and the eddy diffusion coefficient. Because the region between 28 and 48 km appears to be neutrally stable against convection (Schubert et al., 1980), we cannot put a lower limit on the eddy diffusion coefficient. However, it is certainly not greater than $\sim 10^4 \text{ cm}^2 \text{ s}^{-1}$. This would imply a

destruction coefficient of $S \approx 3 \times 10^{-8} \text{ s}^{-1}$ and, at the number density of that level in the atmosphere and a mixing ratio of 200 ppm, a reaction rate of $R \approx 4 \times 10^8 \text{ cm}^{-3} \text{ s}^{-1}$.

In fact, the eddy diffusion coefficient can be much smaller than this. Therefore the very quick decrease in the abundance which we observed could be achieved with a relatively small reaction rate and requires no violent chemistry. The other main conclusion we can draw from the above discussion is that the sink for SO_2 must exist in full force at the point in the atmosphere where the mixing ratio profile begins its decline.

The discussion above is based on our fitting to the Muhleman et al. (1980) model atmosphere. If we instead use the Pioneer Venus atmospheric temperature profile we find that the abundance profile must begin to drop at a lower altitude or, alternatively, that the decrease is more precipitous. Indeed, if the abundance measured by Pioneer Venus for SO_2 at 40 km is correct this decrease must be almost instantaneous. This would imply that either the destruction mechanism for SO_2 above that point is extremely efficient or that the eddy diffusion coefficient is almost zero.

Other Possible Sources of Opacity

Though we have discussed our results in terms of constraints on the SO_2 abundance profile, the data really constrain the absorption

coefficient profile in general. For instance, any strong absorption in the clouds themselves, either due to the cloud particles or to the presence of another absorber such as H_2SO_4 gas, would also affect the zero crossing measurement. Both these possible sources are linked to the cloud distribution, therefore we can limit them both by limiting the absorption coefficient in the clouds. Because we have no a priori knowledge of the form of possible sources of extra opacity, we have increased the absorption coefficient in the lower cloud by a fraction of the CO_2 value at each height. The CO_2 opacity in this region averages roughly 0.1 km^{-1} , and our measurement limits any extra source of opacity in this region to be at most 20% of this value. This does not rule out a cloud opacity similar to that measured by Kliore et al. (1979) at X-band (3.8 cm), but it does imply that the source of that opacity cannot be a molecular absorption that increases as ν or ν^2 . If accurate laboratory measurements of the H_2SO_4 opacity are made (Steffes and Eshleman, 1981), our result will place constraints on the amount of H_2SO_4 gas in the lower cloud layer and below the clouds in much the same way as for SO_2 . This might shed some light on the way in which the H_2SO_4 droplets are destroyed below the clouds.

In addition we note that the fit of Muhleman et al. (1980) required that there be extra absorption throughout the atmosphere producing an additional 83% above that due to CO_2 (i.e. that the absorption coefficient of CO_2 had to be multiplied up by a factor of 1.83 to

account for their observations). The measurements used in the determination of this quantity were sensitive to that part of the atmosphere well below the clouds. We have used this same factor throughout the atmosphere to judge its effect on the zero crossing and brightness temperature at 3.4 mm. The brightness temperature produced is well below the measured brightness of 357.5 K (Ulich et al., 1980). In addition, the zero crossing is almost 2σ below our measured value even in the total absence of SO_2 . Thus it appears that whatever the source of the additional opacity in the lower atmosphere at cm wavelengths, it either does not exist at mm wavelengths or is confined to the region below about 30 km.

Brightness Temperature of Venus at Millimeter Wavelengths

We have noted that the constraints placed on the zero crossing also constrain the disk average brightness temperature. In terms of the two atmospheric models which were used, the brightness temperatures were found to be 361.0 ± 0.6 (corresponding to 1σ in β_0) or ± 3.0 (2σ) using the Muhleman et al. (1979) atmospheric model or 365.0 ± 3.0 (2σ) using the Pioneer Venus data. Using the Pioneer Venus data we cannot reproduce a zero crossing within 1σ of the measured value. This may be due to the fact that the temperatures measured in situ do not constitute a disk average. At worst this represents a 2% uncertainty, therefore Venus at this wavelength should be a very good calibration source. The brightness temperature generated by the model which best fits the

zero crossing measurement ($T_b = 361.0$) is in very good agreement with the measurements of Ulich et al. (1980); (357.5 ± 13.1 K).

The only detectable opacity source at 3.4 mm λ appears to be CO_2 , therefore we can assume that over most of the millimeter spectrum a model in which this is the only source should predict the continuum brightness temperature of Venus accurately.

Use of Venus as an Absolute Calibration Source

Because the brightness temperature of Venus appears to be tightly confined it would seem that Venus represents an extremely good absolute calibration source in this wavelength region. The extreme stability of the atmosphere argues that fluctuations should not be an issue and the high absolute brightness of the source, which can produce an antenna temperature of around 100K at inferior conjunction, makes this an easy source to use for this purpose. Phase effects, which would be caused by diurnal variations, should also be quite small at this depth in the atmosphere. The other planets, in particular Jupiter and Saturn, can also be used for calibration purposes if accurate ratios to Venus are made. Ulich et al. (1980) have measured the brightness of Jupiter and Saturn to be 179.4 ± 4.7 K and 153.4 ± 4.8 K respectively at 86.1 GHz. We have measured the flux ratios of the three planets during November of 1980, when they were near each other in the sky, thus removing atmospheric effects to first order. These measurements were made at three frequencies: 94.51, 104.02 and 113.53 GHz. From our model we

predict the mean brightness temperature of Venus at these three frequencies to be 353.6, 345.1 and 337.7 K respectively. Using this and the flux ratios we measured (corrected for beamsize effects and scaled for distance) we have calculated the temperatures of Jupiter and Saturn at the three frequencies. For Jupiter the three measured temperatures are 194 ± 13 , 186 ± 6 and 174 ± 6 K and for Saturn they were 171 ± 24 , 163 ± 8 and 157 ± 8 K for 94.51, 104.02 and 113.53 GHz respectively.

If we assume that Jupiter and Saturn actually have the same brightness temperatures at these three frequencies (and they should), we can take the weighted average of these three values. Doing so we find that $T_{\text{Jupiter}} = 181 \pm 4$ K and $T_{\text{Saturn}} = 161 \pm 6$ K at the mean wavelength of 2.9 mm (103.5 GHz). These uncertainties do not include the uncertainty in the Venus temperatures, which we have estimated to be about 2%. Including this increases the uncertainties for the temperatures of Jupiter and Saturn to ± 6 K and ± 8 K respectively.

BIBLIOGRAPHY FOR PART II

- Chandrasekhar, S. (1960) Radiative Transfer, New York, Dover Press.
- Esposito, L.W., Winick, J.R. and Stewart, A.I. (1979), Sulfur Dioxide in the Venus Atmosphere: Distribution and Implications. Geophys. Res. Let. 6, 601-604.
- Hoffman, J.H., Hodges, R.R., Donahue, T.M. and McElroy, M.B. (1980), Composition of the Venus Lower Atmosphere from the Pioneer Venus Mass Spectrometer. J. Geophys. Res. 85, 7882-7890.
- Ho, W., Kaufman, I.A. and Thaddeus, P. (1966) J. Geophys. Res. 71, 5091.
- Janssen, M.A. and Poynter, R.L. (1981), The Microwave Absorption of SO₂ in the Venus Atmosphere. Icarus 46, 51-75.
- Kolbe, W.F., Leskovar, B. and Buscher, H. (1976), Absorption Coefficients of Sulfur Dioxide Microwave Rotational Lines. J. Mol. Spec. 59, 86-95.
- Kliore, A.J., Elachi, C., Patel, I.R. and Cimino, J.B. (1979), Liquid Content of the Lower Clouds of Venus as Determined from Mariner 10 Radio Occultation. Icarus 37, 51-72.

- Knollenberg, R.G. and Hunten, D.M. (1980). The Microphysics of the Clouds of Venus: Results of the Pioneer Venus Particle Size Spectrometer Experiment. J. Geophys. Res. 85, 8039-8058.
- Krishnaji and Chandra, S. (1963), Molecular Interactions and Linewidths of the Assymmetric Molecule SO₂. J. Chem. Phys. 38, 1019-1021.
- Muhleman, D.O., Orton, G.S. and Berge, G.L. (1979), A Model of the Venus Atmosphere from Radio, Radar and Occultation Observations. Ap. J. 234, 733-745.
- Oyama, V.I., Carle, G.C., Woeller, F., Pollack, J.B., Reynolds, R.T. and Craig, R.A. (1980), Pioneer Venus Gas Chromatography of the Lower Atmosphere of Venus. J. Geophys. Res. 85, 7891-7902.
- Penzias, A.A. and Burrus, C.A. (1973), Millimeter-wavelength Radio Astronomy Techniques Ann. Rev. Ast. Ap. 11, 5172.
- Poynter, R.L. and Pickett, H.M. (1980), Submillimeter, Millimeter, and Microwave Spectral Line Catalogue. JPL Publication 80-23.
- Seiff, A., Kirk, D.B., Young, R.E., Blanchard, R.C., Findlay, J.T., Kelley, G.M. and Sommer, S.C. (1980), Measurements of Thermal Structure and Thermal Contrasts in the Atmosphere of Venus and Related Dynamical Observations: Results from the Four Pioneer Venus Probes. J. Geophys. Res. 85, 7903-7933.

- Shubert, G., Covey, C., Del Genio, A., Elson, L.S., Keating, G., Seiff, A., Young, R.E., Apt, J., Counselman, C.C., Kliore, A.J., Liyame, S.S., Revercomb, H.E., Sromovsky, L.A., Soumi, V.E., Taylor, F., Woo, R., and von Zahn, U. (1980), Structure and Circulation of the Venus Atmosphere. J. Geophys. Res. 85, 8007-8025.
- Ulich, B.L., Davis, J.H., Rhodes, P.J. and Hollis, J.M. (1980), Absolute Brightness Temperature Measurements at 3.5 mm Wavelength. IEEE Trans. Antenn. Prop. 28, 367-377.
- von Zahn, U., Kumar, S., Niemann, H., and Prinn, R. (1983), Composition of the Venus Atmosphere. in Venus, University of Arizona Press, 299-430.
- Winick, J.R. and Stewart, A.I.F. (1980), Photochemistry of SO₂ in Venus' Upper Cloud Layer. J. Geophys. Res. 85, 7849-7860.
- Young, A.T. (1973), Are the Clouds of Venus Sulfuric Acid? Icarus 18, 564-582.

A P P E N D I C E S

Appendix A

Visibility Function from Brightness Temperature Distribution

The radiance coming from a planet or any other object can be denoted by a temperature T_b (the brightness temperature) through the equation

$$I_v = \frac{2kT_b}{\lambda^2} \quad (1)$$

If the Rayleigh-Jeans approximation to the Planck function is accurate (i.e. if $kT \gg h\nu$) and if the radiation arises in an optically thick region of uniform temperature, then this brightness temperature is equal to the kinetic temperature in the source. For Venus at mm wavelengths, the atmosphere is optically thick and the radiation is coming primarily from a region where the kinetic temperature is between roughly 250 and 450 K. Thus, the brightness temperatures measured fall within this range, at our wavelength (3.4 mm) being 361 K.

This radiance I_v corresponds to an electric field vector $\overline{E_0}$ where

$$E_0^2 = I_v \quad (2)$$

(E_0 = source strength/unit area)

The electric field is assumed to vary as

$$\bar{E} = \bar{E}_0 e^{i\omega t} \quad (\omega = 2\pi\nu) \quad (3)$$

(where the bar denotes a time average) and at a distance R from the area da where this field arises the effect is felt as

$$dE = \frac{\bar{E}_0}{R} e^{i(\omega t - kR)} da \quad (k = 2\pi/\lambda) \quad (4)$$

which is just a spherical wave.

To obtain the electric field on a plane (the interferometer) at a distance D from the source (the planet) we must integrate over the sources contributions. The field at (X, Y) due to a point source at (x, y) can be approximated

$$E(X, Y) = \frac{E_0(x, y)}{R} e^{i(\omega t - kR)} \quad (5)$$

However,

$$\begin{aligned} R &= D [1 - 2(Xx + Yy)/D^2]^{1/2} \\ &\approx D [1 - (Xx + Yy)/D^2] \end{aligned} \quad (6)$$

Therefore

$$E(X, Y) \approx \frac{e^{i(\omega t - kD)}}{D} \times E_0(x, y) e^{ik(Xx - Yy)/D} \quad (7)$$

For a circular planet,

$$x = r \cos\theta \quad y = r \sin\theta$$

$$X = s \cos\phi \qquad Y = s \sin\phi$$

so in this case

$$E(s, \phi) \approx \frac{e^{i(\omega t - kD)}}{D} \times E_0(e, \theta) e^{i(krs/D)\cos(\theta - \phi)} \quad (8)$$

This can be further simplified if we have azimuthal symmetry. For Venus at millimeter wavelengths this is not a bad assumption since models of the meteorology predict that at the lower cloud levels there should be little latitudinal variations in temperature. Thus we can set $\phi = 0$ without loss of generality.

$$E(s) \approx \frac{e^{i(\omega t - kD)}}{D} \times E_0(r) e^{i(krs/D)\cos\theta} \quad (9)$$

A two element interferometer consists of two telescopes a distance d apart and a distance D from the source. We define one of the two as the origin of the (s, ϕ) coordinate system. A time delay is placed in the lines leading from the telescopes in order to compare the electric fields generated on a plane perpendicular to the source. On this plane the elements of the interferometer are effectively spaced a distance of s apart. The signals from the two elements, which are voltages proportional to the electric field strengths at the telescopes, are put through a multiplier whose output is proportional to the product of the input voltages. This output, averaged over time, is the response of the interferometer.

If the source is a point at (r, θ) on the sky the response will be

$$\begin{aligned}
 R(r, \theta) &= A \overline{E_1 E_2} \\
 &= A \overline{E(0)E(s)} \\
 &= \frac{A e^{2i(\omega t - kD)}}{D^2} \times E_0^2(r) e^{i(krs/D) \cos \theta} \\
 &= \frac{A}{D^2} E_0^2(r) e^{i(krs/D) \cos \theta} \quad (10)
 \end{aligned}$$

where A is the constant of proportionality and represents an effective area for the combined telescopes.

This is the response of the interferometer to a point source at (r, θ) when the projected spacing of the interferometer is s .

Integrating in r and θ over an extended source, we get the total response

$$\begin{aligned}
 R_{TOT} &= \frac{A}{D^2} \int_0^\infty E_0^2(r) \left[\int_0^{2\pi} e^{i(krs/D) \cos \theta} d\theta \right] r dr \\
 &= \frac{A}{D^2} \int_0^\infty E_0^2(r) J_0(krs/D) r dr \\
 &= A \int_0^\infty \left(\frac{2kT_b(r)}{\lambda^2} \right) J_0 \left(2\pi \frac{s r}{\lambda D} \right) \left(\frac{r}{D} \right) \left(\frac{dr}{D} \right) \quad (11)
 \end{aligned}$$

We define

$$\beta = \frac{s r_0}{\lambda D} \quad \text{where } r_0 \text{ is a reference radius,} \quad (12)$$

in our case the radius of the
visible planet

$$= \frac{s}{\lambda} \alpha_0 \quad \text{where } \alpha_0 \text{ is the angular size of} \\ r_0 \text{ at the distance } D$$

Thus

$$R_{TOT}(\beta) = A \int_0^{\infty} S(\alpha) J_0\left(\frac{2\pi\beta\alpha}{\alpha_0}\right) \alpha \, d\alpha \quad (13)$$

where

$$S(\alpha) = \frac{2kT_b(D\alpha)}{\lambda^2}$$

$$= \frac{2kT_b(r)}{\lambda^2} : \text{ the specific intensity} \quad (14)$$

This response $R_{TOT}(\beta)$ is called the visibility function and denoted $V(\beta)$. At $\beta = 0$ ($s = 0$) the bessel function J_0 is unity. Therefore,

$$V(\beta=0) = A \int_0^{\infty} S(\alpha) \alpha \, d\alpha$$

$$= A S_0$$

where

$$S_0 = \frac{2k\bar{T}_b \Omega}{\lambda^2} \quad \text{is the total flux density} \quad (15)$$

$$\Omega = \pi \alpha_0^2$$

$$= \pi \frac{r_0^2}{D^2} \quad \text{is the solid angle subtended} \\ \text{by the source}$$

and

$$\overline{T_b} = \frac{1}{\pi r_0^2} \int_0^{\infty} T_b(r) r dr$$

is the mean brightness temperature of the source. For our particular case we prefer to use spatial distance rather than angular ones since we will be doing the integrations in spatial coordinates at the planet. Therefore we will use (13) in the form

$$V(\beta) = \frac{2k}{\lambda^2 D^2} \int_0^{r_{\max}} T_b(r) J_0\left(2\pi\beta\frac{r}{r_0}\right) r dr$$

where again

$$\beta = \frac{s r_0}{\lambda D}$$

with

- s = the projected spacing of the interferometer
- λ = the wavelength (for us 3.4 mm)
- D = distance to Venus (for us 2.17×10^{13} cm)
- r_0 = reference radius of Venus (6100 km).

Appendix B

Error Analysis

To find the zero crossing in the visibility function data we have used a polynomial least squares fit in which we have fitted not for the polynomial coefficients but for the zero crossing itself. This represents a simple adjustment to the standard least squares polynomial algorithm but one which we have not seen elsewhere. In fact, least squares fitting in general seems to be poorly understood by many. In order to avoid any confusion we will here present our derivation from first (almost) principles.

We are not attempting to explain why or when the errors in individual data points form a normal distribution about some mean curve. What concerns us here is the determination of that mean curve in terms of the parameters that define it. Neither are we attempting to promote a method for determining what form the curve should take, a question that is highly situation dependant and to a large degree a subjective decision. What we describe is the method of best fitting for the parameters of a curve of predefined functional form.

Data Fitting

In general one wishes to fit a set of measured points $(x_i, y_i \pm \sigma_i ; i=1, n)$ with a curve $y(x; a_j)$ where the a_j ($j=1, m$) are the parameters defining the curve (e.g. polynomial coefficients), the

values of which we will determine. We will assume here that the points y_i are distributed normally about the the curve $y(x)$ and therefore that the quantities

$$[y_i - y(x_i)]$$

have a gaussian distribution about 0. The goodness of the fit is characterized by the quantity

$$\chi^2 = \sum_i \frac{1}{\sigma_i^2} [y_i - y(x_i)]^2 \quad (1)$$

which should be a minimum when the a_j are optimized for the best fit. Of course, this does not guarantee that the choice of the funtional form for the fitting curve is optimal, just that we have optimized the form under consideration. We will denote the optimal values of the a_j by a_j^* . The above comments merely represent a review and are offered without proof.

In order to minimize χ^2 we require that

$$\left. \frac{\partial \chi^2}{\partial a_j} \right|_{a_j^*} = \sum_i - \frac{2}{\sigma_i^2} [y_i - y(x_i)] \left. \frac{\partial y(x_i)}{\partial a_j} \right|_{a_j^*} = 0 \quad (2)$$

If the function $y(x)$ is linear in the a_j (which it is for a polynomial) this is a sufficient condition to determine the a_j^* exactly. We shall do so for our special case below. If $y(x)$ is not linear in the a_j we must approximate the equations and iterate to a solution. This involves choosing some initial guess for the a_j and linearizing the equations. In general we can make a Taylor series expansion:

$$\frac{\partial \chi^2}{\partial a_j} \approx \left. \frac{\partial \chi^2}{\partial a_j} \right|_{a_j^*} + \sum_k \left. \frac{\partial^2 \chi^2}{\partial a_j \partial a_k} \right|_{a_j^* a_k^*} (a_k - a_k^*) \quad (3)$$

where the first term after the equality is zero by the definition of a_j^* (equation 2). This set of equations (there is one for each j) can be conveniently written in matrix form:

$$\begin{pmatrix} \frac{1}{2} \frac{\partial^2 \chi^2}{\partial a_1 \partial a_1} & \frac{1}{2} \frac{\partial^2 \chi^2}{\partial a_1 \partial a_2} & \frac{1}{2} \frac{\partial^2 \chi^2}{\partial a_1 \partial a_3} & \dots & \frac{1}{2} \frac{\partial^2 \chi^2}{\partial a_1 \partial a_m} \\ \frac{1}{2} \frac{\partial^2 \chi^2}{\partial a_2 \partial a_1} & \frac{1}{2} \frac{\partial^2 \chi^2}{\partial a_2 \partial a_2} & \frac{1}{2} \frac{\partial^2 \chi^2}{\partial a_2 \partial a_3} & \dots & \frac{1}{2} \frac{\partial^2 \chi^2}{\partial a_2 \partial a_m} \\ \frac{1}{2} \frac{\partial^2 \chi^2}{\partial a_3 \partial a_1} & \frac{1}{2} \frac{\partial^2 \chi^2}{\partial a_3 \partial a_2} & \frac{1}{2} \frac{\partial^2 \chi^2}{\partial a_3 \partial a_3} & \dots & \frac{1}{2} \frac{\partial^2 \chi^2}{\partial a_3 \partial a_m} \\ \vdots & \vdots & \vdots & \ddots & \vdots \\ \frac{1}{2} \frac{\partial^2 \chi^2}{\partial a_m \partial a_1} & \frac{1}{2} \frac{\partial^2 \chi^2}{\partial a_m \partial a_2} & \frac{1}{2} \frac{\partial^2 \chi^2}{\partial a_m \partial a_3} & \dots & \frac{1}{2} \frac{\partial^2 \chi^2}{\partial a_m \partial a_m} \end{pmatrix} \begin{pmatrix} a_1 - a_1^* \\ a_2 - a_2^* \\ a_3 - a_3^* \\ \vdots \\ a_m - a_m^* \end{pmatrix} = \begin{pmatrix} \frac{1}{2} \frac{\partial \chi^2}{\partial a_1} \\ \frac{1}{2} \frac{\partial \chi^2}{\partial a_2} \\ \frac{1}{2} \frac{\partial \chi^2}{\partial a_3} \\ \vdots \\ \frac{1}{2} \frac{\partial \chi^2}{\partial a_m} \end{pmatrix}$$

or as matrices $\bar{\alpha} \times \bar{a} = \bar{d}$

where the factor of $1/2$ throughout has been added for later convenience.

The matrix α is called the curvature matrix since it contains all the terms involved in the curvature of χ^2 with respect to the a_j . If we solve for a , which is of course what we are interested in;

$$\bar{a} = \bar{\alpha}^{-1} \times \bar{d} = \bar{\epsilon} \times \bar{d} \quad (4')$$

we find that we must invert $\bar{\alpha}$. The resulting matrix, $\bar{\epsilon}$, is call the error matrix for reasons that will become apparent.

We have yet to determine either the first derivatives needed for \bar{d} or the second derivatives in $\bar{\alpha}$. From the definition of χ^2 we can easily derive

$$\frac{1}{2} \frac{\partial \chi^2}{\partial a_j} = \sum_i \frac{-1}{\sigma_i^2} [y_i - y(x_i)] \frac{\partial y(x_i)}{\partial a_j} \quad (5)$$

$$\approx \sum_i \frac{-1}{\sigma_i^2} [y_i - y(x_i)] \left(\frac{y(x_i; a_j + \Delta a_j) - y(x_i; a_j)}{\Delta a_j} \right) \quad (5')$$

If the partial derivative can be done analytically as is the case for our fit it is not necessary to use the finite difference equation. If this becomes necessary care must be taken to choose an appropriate stepsize. We can continue the process of by taking the second derivative

$$\frac{1}{2} \frac{\partial^2 \chi^2}{\partial a_j \partial a_k} = \sum_i \frac{1}{\sigma_i^2} \left[\left(\frac{\partial y(x_i)}{\partial a_j} \right) \left(\frac{\partial y(x_i)}{\partial a_k} \right) - (y_i - y(x_i)) \frac{\partial^2 y(x_i)}{\partial a_j \partial a_k} \right] \quad (6)$$

If the function is second order in the a_j the the second term inside the summation, while it is not identically zero, sums to zero. Thus in this case, which is a good approximation in most situations

$$\frac{1}{2} \frac{\partial^2 \chi^2}{\partial a_j \partial a_k} = \sum_i \frac{1}{\sigma_i^2} \left[\frac{\partial y(x_i)}{\partial a_j} \frac{\partial y(x_i)}{\partial a_k} \right] \quad (6')$$

$$\approx \sum_i \frac{1}{\sigma_i^2} \frac{(y(x_i; a_j + \Delta a_j) - y(x_i; a_j))}{\Delta a_j} \frac{(y(x_i; a_k + \Delta a_k) - y(x_i; a_k))}{\Delta a_k} \quad (6'')$$

Using (5) and (6):

$$\left(\begin{array}{ccc} \sum_i \frac{1}{\sigma_i^2} \frac{\partial y(x_i)}{\partial a_1} \frac{\partial y(x_i)}{\partial a_1} & \sum_i \frac{1}{\sigma_i^2} \frac{\partial y(x_i)}{\partial a_1} \frac{\partial y(x_i)}{\partial a_2} & \dots \sum_i \frac{1}{\sigma_i^2} \frac{\partial y(x_i)}{\partial a_1} \frac{\partial y(x_i)}{\partial a_m} \\ \sum_i \frac{1}{\sigma_i^2} \frac{\partial y(x_i)}{\partial a_2} \frac{\partial y(x_i)}{\partial a_1} & \sum_i \frac{1}{\sigma_i^2} \frac{\partial y(x_i)}{\partial a_2} \frac{\partial y(x_i)}{\partial a_2} & \dots \sum_i \frac{1}{\sigma_i^2} \frac{\partial y(x_i)}{\partial a_2} \frac{\partial y(x_i)}{\partial a_m} \\ \vdots & \vdots & \vdots \\ \sum_i \frac{1}{\sigma_i^2} \frac{\partial y(x_i)}{\partial a_m} \frac{\partial y(x_i)}{\partial a_1} & \sum_i \frac{1}{\sigma_i^2} \frac{\partial y(x_i)}{\partial a_m} \frac{\partial y(x_i)}{\partial a_2} & \dots \sum_i \frac{1}{\sigma_i^2} \frac{\partial y(x_i)}{\partial a_m} \frac{\partial y(x_i)}{\partial a_m} \end{array} \right)$$

$$\times \begin{pmatrix} a_1 - a_1^* \\ a_2 - a_2^* \\ \vdots \\ a_m - a_m^* \end{pmatrix} = \begin{pmatrix} \sum_i \frac{-1}{\sigma_i^2} [y_i - y(x_i)] \frac{\partial y(x_i)}{\partial a_1} \\ \sum_i \frac{-1}{\sigma_i^2} [y_i - y(x_i)] \frac{\partial y(x_i)}{\partial a_2} \\ \vdots \\ \sum_i \frac{-1}{\sigma_i^2} [y_i - y(x_i)] \frac{\partial y(x_i)}{\partial a_m} \end{pmatrix}$$

which can be further approximated by (5') and (6'') and solved as in (4). If all the σ_i are the same (and normally we have no recourse but

to assume that they are) they disappear from the above equations. Since the a_j were our own choice and since we have solved for $(a_j - a_j^*)$ we can calculate the a_j^* . If our first guess was too far from the correct value for the various approximations to be accurate we must iterate using the new value as the starting point of the next iteration. In the case where the function $y(x; a_j)$ is linear in the a_j all the equations are exact and we can simplify all of the above by starting with $a_j = 0$.

Error Analysis

Before deriving the formulation for our case we should discuss the method for ascertaining the uncertainties involved. To find the uncertainty in the fitted parameter a_j (denoted by σ_{a_j}) we will again need to assume that the function is no more than second order in the parameters (ie. that equation 6 is valid).

The uncertainty in parameter a_j is affected by each of the data points. In general;

$$\sigma_{a_j}^2 = \sum_i \left(\frac{\partial a_j}{\partial y_i} \right)^2 \sigma_i^2 \quad (8)$$

where we are here considering each of the y_i as a measurable parameter with a given uncertainty (σ_i) and asking what effect the uncertainties in the y_i have on the derived parameter a_j . This is the standard form for propagation of errors when the measured parameters, the y_i , are

uncorrelated. The form of this equation arises when one asks what the rms of the $(a_j)_i$ is, where the $(a_j)_i$ are defined as the values of a_j as would be determined by the values of the i^{th} measured alone. We will not perform the necessary summation and limit here. The covariance between a_j and a_k is similarly found to be

$$\sigma_{a_j a_k} = \sum_i \left(\frac{\partial a_j}{\partial y_i} \right) \left(\frac{\partial a_k}{\partial y_i} \right) \sigma_i^2 \quad (8')$$

It is apparent that (8) is just a special case of (8'), as indeed it should be. Using (4')

$$\bar{a} = \bar{\epsilon} \times \bar{d} \quad (9)$$

where

$$\epsilon_{jk} = (\bar{\alpha}^{-1})_{jk}$$

and

$$\alpha_{jk} = \frac{1}{2} \frac{\partial^2 \chi^2}{\partial a_j \partial a_k} \quad \text{by definition.}$$

We can write out a single term of (9) as

$$(a_j - a_j^*) = \sum_k \epsilon_{jk} \left(\frac{1}{2} \frac{\partial \chi^2}{\partial a_k} \right) \quad (9')$$

and take the derivative

$$\begin{aligned} \frac{\partial a_j}{\partial y_i} &= \frac{\partial (a_j - a_j^*)}{\partial y_i} = \sum_k \epsilon_{jk} \frac{\partial}{\partial y_i} \left(\frac{1}{2} \frac{\partial \chi^2}{\partial a_k} \right) \\ &= \sum_k \epsilon_{jk} \frac{\partial}{\partial y_i} \left(\sum_l - \frac{1}{\sigma_l^2} [y_l - y(x_l)] \frac{\partial y(x_l)}{\partial a_k} \right) \end{aligned}$$

$$= \sum_k \epsilon_{jk} \left(- \frac{1}{\sigma_i^2} \frac{\partial y(x_i)}{\partial a_k} \right) \quad (10)$$

If we use this relationship in (8')

$$\begin{aligned} \sigma_{a_j a_k} &= \sum_i \left(\frac{\partial a_j}{\partial y_i} \right) \left(\frac{\partial a_k}{\partial y_i} \right) \sigma_i^2 \\ &= \sum_i \left(\sum_l \frac{-\epsilon_{jl}}{\sigma_i^2} \frac{\partial y(x_i)}{\partial a_l} \right) \left(\sum_m \frac{-\epsilon_{km}}{\sigma_i^2} \frac{\partial y(x_i)}{\partial a_m} \right) \sigma_i^2 \\ &= \sum_i \sum_l \sum_m \epsilon_{jl} \epsilon_{km} \left(\frac{1}{\sigma_i^2} \frac{\partial y(x_i)}{\partial a_l} \frac{\partial y(x_i)}{\partial a_m} \right) \\ &= \sum_l \sum_m \epsilon_{jl} \epsilon_{km} \left(\sum_i \frac{1}{\sigma_i^2} \frac{\partial y(x_i)}{\partial a_l} \frac{\partial y(x_i)}{\partial a_m} \right) \\ &= \sum_l \sum_m \epsilon_{jl} \epsilon_{km} \left(\frac{1}{2} \frac{\partial^2 \chi^2}{\partial a_l \partial a_m} \right) \\ &= \sum_l \epsilon_{jl} \left(\sum_m \epsilon_{km} \alpha_{ml} \right) \\ &= \sum_l \epsilon_{jl} I_{lk} \end{aligned}$$

where \bar{I} is the identity matrix.

Thus we have shown that in general

$$\sigma_{a_j a_k} = \epsilon_{jk} \quad (11)$$

and of course $\sigma_{a_j}^2 = \epsilon_{jj}$ as a special case.

$\bar{\epsilon}$ is called the error matrix. Having obtained the curvature matrix $\bar{\alpha}$, either exactly or by approximation with finite differences, we can invert for $\bar{\epsilon}$.

This matrix is used to solve for the corrections to the a_j if we are using the approximation method and when the correct values are found contains the errors in the parameters and the correlations between them. These correlations are more usually expressed in normalized form as the correlation coefficients

$$\rho_{a_j a_k} = \frac{\sigma_{a_j a_k}}{\sigma_{a_j} \sigma_{a_k}} \quad (12)$$

which is bounded by ± 1 representing respectively high correlation and high anticorrelation.

Error Analysis on the Zero Crossing

The zero crossing data is in the form of a set of (x_i, y_i) points where x_i is the normalized spacing; β , and y_i is the amplitude corrected for sign by the phase information. We wish to fit these points with a quadratic curve

$$y(x) = A(x - x_0)^2 + B(x - x_0)$$

and in particular we want to find the uncertainty in x_0 ; the zero crossing.

In this case the curvatures can be derived and the parameters solved for exactly. The goodness of fit, χ^2 , can be written

$$\chi^2 = \frac{1}{\sigma_i^2} \sum_i [y_i - A(x_i - x_0)^2 - B(x_i - x_0)]^2$$

where we are assuming that the uncertainty in each point is the same. In practice we have used for σ_i the rms noise in the data after the fit. The first derivatives of χ^2 are given by

$$\frac{\partial \chi^2}{\partial A} = \frac{1}{\sigma_i^2} \sum_i -2 [y_i - A(x_i - x_0)^2 - B(x_i - x_0)] (x_i - x_0)^2$$

$$\frac{\partial \chi^2}{\partial B} = \frac{1}{\sigma_i^2} \sum_i -2 [y_i - A(x_i - x_0)^2 - B(x_i - x_0)] (x_i - x_0)$$

$$\frac{\partial \chi^2}{\partial x_0} = \frac{1}{\sigma_i^2} \sum_i 2 [y_i - A(x_i - x_0)^2 - B(x_i - x_0)] (2A(x_i - x_0) + B)$$

and the second order terms by

$$\frac{\partial^2 \chi^2}{\partial A^2} = \frac{1}{\sigma_i^2} \sum_i 2(x_i - x_0)^4$$

$$\frac{\partial^2 \chi^2}{\partial B^2} = \frac{1}{\sigma_i^2} \sum_i 2(x_i - x_0)^2$$

$$\frac{\partial^2 \chi^2}{\partial x_0^2} = \frac{1}{\sigma_1^2} \sum_i 2[-2A(y_i - A(x_i - x_0))^2 - B(x_i - x_0) + (2A(x_i - x_0) + B)^2]$$

$$\frac{\partial^2 \chi^2}{\partial A \partial B} = \frac{1}{\sigma_1^2} \sum_i 2(x_i - x_0)^3$$

$$\frac{\partial^2 \chi^2}{\partial x_0 \partial A} = \frac{1}{\sigma_1^2} \sum_i 2[2y_i(x_i - x_0) - 4A(x_i - x_0)^3 - 3B(x_i - x_0)^2]$$

$$\frac{\partial^2 \chi^2}{\partial x_0 \partial B} = \frac{1}{\sigma_1^2} \sum_i 2[y_i - 3A(x_i - x_0)^2 - 2B(x_i - x_0)]$$

from which we can create the curvature matrix

$$\bar{\alpha} = \begin{pmatrix} \frac{1}{2} \frac{\partial^2 \chi^2}{\partial A \partial A} & \frac{1}{2} \frac{\partial^2 \chi^2}{\partial A \partial B} & \frac{1}{2} \frac{\partial^2 \chi^2}{\partial A \partial x_0} \\ \frac{1}{2} \frac{\partial^2 \chi^2}{\partial A \partial B} & \frac{1}{2} \frac{\partial^2 \chi^2}{\partial B \partial B} & \frac{1}{2} \frac{\partial^2 \chi^2}{\partial B \partial x_0} \\ \frac{1}{2} \frac{\partial^2 \chi^2}{\partial A \partial x_0} & \frac{1}{2} \frac{\partial^2 \chi^2}{\partial B \partial x_0} & \frac{1}{2} \frac{\partial^2 \chi^2}{\partial x_0^2} \end{pmatrix}$$

and the vector

$$\bar{d} = \begin{pmatrix} \frac{1}{2} \frac{\partial \chi^2}{\partial A} \\ \frac{1}{2} \frac{\partial \chi^2}{\partial B} \\ \frac{1}{2} \frac{\partial \chi^2}{\partial x_0} \end{pmatrix}$$

We can then solve for the parameters $\bar{a} = (A, B, x_0)$ via

$\bar{a} = \bar{\alpha}^{-1} \times \bar{d}$. The matrix $\bar{\alpha}^{-1}$ is of course the error matrix

$$\bar{\epsilon} = \begin{pmatrix} \sigma_A^2 & \sigma_{AB}^2 & \sigma_{Ax0}^2 \\ \sigma_{AB}^2 & \sigma_B^2 & \sigma_{Bx0}^2 \\ \sigma_{Ax0}^2 & \sigma_{Bx0}^2 & \sigma_{x0}^2 \end{pmatrix}$$

Appendix C

Theoretical Limb Darkening Curves

The limb darkening curve for an adiabatic atmosphere in which a locally plane parallel approximation is adequate and for which the absorption coefficient can be represented by a power law in pressure and temperature can be determined exactly.

If we define our coordinate system as we have before with the distance increasing inward (downward toward the surface of the planet), the condition of hydrostatic equilibrium is given by

$$dP = \rho g dh$$

where P is of course the pressure, g the acceleration due to gravity, and h the distance parameter. Since we are postulating an adiabatic ideal gas, the pressure is given by

$$P = \frac{\rho k T}{\mu_m m_H}$$

and

$$\left(\frac{P}{P_0}\right) = \left(\frac{\rho}{\rho_0}\right)^\gamma = \left(\frac{T}{T_0}\right)^{\gamma/(\gamma-1)}$$

where T is the temperature, k is the Boltzmann constant, m_H is the mass of a hydrogen atom, and μ_m is the mean molecular weight of the atmosphere.

We will use the Rayleigh-Jeans approximation for the Planck function,

$$B_{\nu} = \frac{2kT}{\lambda^2}$$

and assume, as we said before, that the absorption coefficient is of the form

$$\begin{aligned} \alpha &= a \left(\frac{P}{P_0}\right)^n \left(\frac{T_0}{T}\right)^m \\ &= a \left(\frac{P}{P_0}\right)^{[n-m(\gamma-1)/\gamma]} \end{aligned}$$

Now,

$$dP = \rho_0 \left(\frac{P}{P_0}\right)^{1/\gamma} g dh$$

therefore

$$dh = \frac{1}{\rho_0 g} \left(\frac{P}{P_0}\right)^{-1/\gamma} dP$$

The optical depth, τ , is given by

$$\begin{aligned} \tau &= \int_0^h \alpha dh' \\ &= \int_0^P a \left(\frac{P'}{P_0}\right)^{[n-m(\gamma-1)/\gamma]} \frac{1}{\rho_0 g} \left(\frac{P'}{P_0}\right)^{-1/\gamma} dP' \\ &= C \int_0^P P'^{[n - m(\gamma-1)/\gamma - 1/\gamma]} dP' \\ &= C P^{[n - m(\gamma-1)/\gamma - 1/\gamma + 1]} \end{aligned}$$

where C is a constant.

Thus

$$P = C' \tau^{\{ [n - m(\gamma-1)/\gamma - 1/\gamma + 1]^{-1} \}}$$

where C' is another constant, and

$$\begin{aligned} T &= T_0 \left(\frac{P}{P_0} \right)^{(\gamma-1)/\gamma} \\ &= T_0 P_0^{-(\gamma-1)/\gamma} \tau^{\left(\frac{\gamma-1}{\gamma n - m(\gamma-1) - 1 + \gamma} \right)} \end{aligned}$$

Also,

$$\begin{aligned} B_\nu &= \frac{2kT}{\lambda^2} \\ &= \frac{2kT_0}{\lambda^2} P_0^{-(\gamma-1)/\gamma} \tau^{\left(\frac{\gamma-1}{\gamma n - m(\gamma-1) - 1 + \gamma} \right)} \end{aligned}$$

We now have all we need to calculate the limb darkening curve. We will assume that the atmosphere can be approximated as plane parallel, not unreasonable considering the other approximations we have made. In general, the specific intensity observed when viewing through an atmosphere at an angle θ (where $\gamma = \cos(\theta)$) is given by

$$\begin{aligned} I(\mu) &= \int_0^\infty B(\tau) e^{-\tau/\mu} \frac{d\tau}{\mu} \\ &= \frac{2kT_0}{\lambda^2} P_0^{-(\gamma-1)/\gamma} \mu^{\left(\frac{\gamma-1}{\gamma n - m(\gamma-1) - 1 + \gamma} \right)} \end{aligned}$$

$$\times \int_0^\infty \frac{(\underline{I})}{\mu} \left(\frac{\gamma - 1}{\gamma n - m(\gamma - 1) - 1 + \gamma} \right) e^{-\tau/\mu} \frac{d\tau}{\mu}$$

For radiation from the center of the disk of the planet, $\theta=0$ ($\mu=1$) and

$$I_0 = I(1) = \frac{2kT_0}{\lambda^2} P_0^{-(\gamma-1)/\gamma} \int_0^\infty \frac{(\underline{I})}{\mu} \left(\frac{\gamma - 1}{\gamma n - m(\gamma - 1) - 1 + \gamma} \right) e^{-\tau} d\tau$$

Comparing this to the general equation above it we find that the integral terms are identical and therefore that

$$I(\mu) = \frac{\gamma - 1}{\mu \left(\gamma n - m(\gamma - 1) - 1 + \gamma \right)}$$

When we view the planet the angular distance outward from the center of the planet as a fraction of the radius of the planet gives us the viewing angle θ

$$\sin(\theta) = \frac{r}{R}$$

Therefore,

$$I(r) = I_0 \left(1 - \frac{r^2}{R^2} \right)^{1/2} \left(\frac{\gamma - 1}{\gamma n - m(\gamma - 1) - 1 + \gamma} \right)$$

